

**ELECTROMAGNETIC PROPERTIES OF
MELT-TEXTURED $\text{YBa}_2\text{Cu}_3\text{O}_{6+x}$ BICRYSTALS OF
GENERAL MISORIENTATION**

by

Michael B. Field

A dissertation submitted in partial fulfillment of the
requirements for the degree of

Doctor of Philosophy
(Materials Science)

at the

UNIVERSITY OF WISCONSIN-MADISON

1996

ABSTRACT

Previous experiments on simple [001] tilt bicrystals of superconducting $\text{YBa}_2\text{Cu}_3\text{O}_{6+x}$ ("YBCO") have demonstrated that grain boundary misorientations of greater than $5\text{-}10^\circ$ strongly degrade the critical current density (J_c). Polycrystalline forms of YBCO contain grains of arbitrary misorientation and have J_c values which are both low and strongly magnetic field ("B") sensitive. This work focused on the superconducting transport properties of such complex, general misorientation YBCO grain boundaries. Despite their more complex structure, their critical current density behavior as a function of misorientation and magnetic field was as good or better than their simpler [001] tilt counterparts.

The first set of experiments dealt with conventionally melt-processed bicrystals with crystal misorientations of $15^\circ\text{-}69^\circ$. Their $J_c(B)$ properties degraded progressively with increasing crystal misorientation. All samples measured at 4K had a residual critical current even in strong fields, indicative of strongly-coupled sections to their boundaries.

The second set of experiments dealt with the detailed characterization of five (5° , 7° , 11° , 14° , 38°) general misorientation YBCO bicrystals produced by the melt-texture,

liquid-phase-removal method. These experiments also possessed grain boundary $J_c(B)$ characteristics which underwent a progressive, rather than a sharp transition with increasing misorientation. The 5° bicrystal had strongly coupled characteristics, while the 7° , 11° and 14° bicrystals had mixed characteristics, indicative of parallel weakly and strongly coupled paths crossing the grain boundary. This was true even for the 38° bicrystal. Based on data from high sensitivity voltage-current traces and magneto-optic imaging, we conclude that some strongly coupled channels remain open, even in very high angle, generally misoriented bicrystals. As a whole these crystals exhibit a slower fall of $J_c(B)$ with misorientation angle than do thin film [001] tilt bicrystals, and the transition from strong to weak coupling as a function of increasing crystal misorientation is neither abrupt nor complete at any misorientation studied.

Acknowledgments

This thesis was not done in a vacuum (no pun intended). There are too many people to thank individually, but let's give it a try. First, there is my advisor Professor David Larbalestier, who guided and focused the thinking behind the experiments and secured funding for both myself and the necessary equipment. Then there is Dr. Xueyu Cai, who taught me basically everything I know about electromagnetic testing of superconductors. Long discussions on the art of Chinese cooking were invaluable as well. Also there are the magneto-optic imaging scientists (Dr. Anatoly Polyanskii and Alex Pashitski), who provided the lovely magneto-optic images shown in Chapter 4. Fellow graduate students, spanning the generations from Henry Muller on down to Michael Naus, played a key role as well, from helping with equipment problems, to maintenance of the group computers, to creating the general feeling of camaraderie of the "6th floor" which made my rather long stay an enjoyable one. Fellow graduated student Harry Edelman deserves special notice for developing the pulsed current measuring system, which was quite useful for measuring many of the samples in this thesis. Also of critical importance was the staff assistance of Bill Starch and Alex Squitieri, who made rigs and maintained magnet systems that were used in my work.

Other research groups influenced my work as well. Professor Susan Babcock and her students helped in my understanding of the structure and properties of grain boundaries. Collaborators at the Texas Center for Superconductivity, Apurva Parikh and

Professor Kamel Salama, provided samples used for the second set of melt-textured grain boundary experiments. Dr. Sungho Jin of AT&T and Dr. Tom Luhman of Boeing also provided samples that were studied in this thesis. The professors and students of the UW “MRG” helped as well with important feedback, and thanks should also be accorded the National Science Foundation, for providing the Materials Research Group grant which provided the financial backing which made this all possible.

Last but not least, thanks to my parents and family, for keeping the fires burning on the homefront. I can now answer the question my family has been asking me for years: “But when are you going to be finished?”

Now!

Table of Contents

Chapter 1 : The Challenge: Bulk Conductor Applications for

<i>YBa₂Cu₃O_{6+x}</i> _____	1
---	----------

Chapter 2 : YBa₂Cu₃O_{6+x}: Processing, Electromagnetic Behavior and Grain

<i>Boundaries</i> _____	12
-------------------------	-----------

The YBa ₂ Cu ₃ O _{6+x} Phase Diagram _____	14
---	-----------

Melt-Texturing of YBa ₂ Cu ₃ O _{6+x} _____	23
---	-----------

Determining the Coupling Characteristics of the Grain Boundary _____	31
--	-----------

Essential Structural Features of Grain Boundaries _____	36
---	-----------

Chapter 3 : Initial Melt-Textured YBa₂Cu₃O_{6+x} Bicrystal Experiments __ **43**

Sample Fabrication _____	43
--------------------------	-----------

Bicrystal Isolation _____	48
---------------------------	-----------

Misorientation Determination - X-Ray Pole Figures _____	52
---	-----------

Electromagnetic Testing _____	61
-------------------------------	-----------

Results _____	65
---------------	-----------

Discussion _____	72
------------------	-----------

<i>Chapter 4 : Experiments with Melt-Out, Melt-Texture (MOMT) YBCO</i>	75
Sample Fabrication and Isolation	78
New Electromagnetic Techniques - Pulsed Current and High Voltage Sensitivity	80
Magneto-Optical Imaging	86
Electromagnetic Results	87
Magneto-Optical Imaging Experiments	98
Results - Role of the Macroscopic Grain Boundary Plane	105
Discussion	110
<i>Chapter 5 : Summary and Conclusions</i>	123
<i>Appendix A: The Mixed Misorientation Description</i>	129
The Mixed Misorientation Description - General Grain Boundary Geometry	129
The Mixed Misorientation Description - Example	136
<i>Appendix B: Laser Cutting of $YBa_2Cu_3O_{6+x}$</i>	141
<i>References</i>	<i>Error! Bookmark not defined.</i>

Table of Figures

Figure 1-1) The irreversibility fields, a measure of the vortex pinning strength, as a function of temperature fraction of T_c for YBCO, Bi-2212, Bi-2223, and La-214. Plot from Suenaga et al. [2].	2
Figure 1-2) Drawings illustrating the thin film YBCO grain boundary geometry of Dimos et al.[14]: a) [001] tilt b) [100] tilt c) [100] twist.	4
Figure 1-3) The plot of the ratio of the intergranular to intragranular critical current densities for YBCO thin films on $SrTiO_3$ with three different primary misorientation geometries {● - (001) tilt, ■ - (100) tilt, ▲ - (100) twist}, at 5K and no applied magnetic field, from Dimos et al.[14].	5
Figure 1-4) Plot of transport $J_c(B)$ for flux-grown bulk YBCO bicrystals with $H//c$, 77K for an intragranular region (▲), and the $3^\circ[001]$ tilt (□), $15^\circ[001]$ tilt (■), $90^\circ[010]$ part tilt/part twist (▼) bicrystals. Adapted from Babcock et al.[4].	7
Figure 2-1) The typical microstructure of polycrystalline sintered YBCO, view under polarized light, from Verhoeven[.]. The brightness contrast between the grains is due to the crystal misorientation, and the striations visible within the grains are twin boundaries (major tick=10 μ m, minor tick=1 μ m).	13
Figure 2-2) Drawing of the perovskite crystal structure, where A and B are metallic cations and X is a non-metallic anion. The YBCO unit cell is composed of three of these perovskite unit cells stacked: the center cell has Y as the A cation, and the top and bottom cells have Ba as the A cation. In both cases, Cu is the B cation and O is the X anion, as shown in Figure 2-4.	15
Figure 2-3) Schematic diagram of twin trace pattern. A 90° cross pattern generally indicates viewing plane normal to c axis, parallel twins indicate viewing planes parallel to c-axis.	16
Figure 2-4) Drawing of the YBCO unit cell, orthorhombic and fully oxygenated to O_7 . The CuO_2 planes are kinked. Vacancies for $O < 7$ occur mainly at the O1 and O5 locations, with some on O4 as well[.]. Drawing from ref. [48].	18
Figure 2-5) Graph of the T_c of $YBa_2Cu_3O_{6+x}$ as a function of oxygen stoichiometry (x). Solid points are calculation, open points are experimental data[.]. From Poulsen et al.[54].	19
Figure 2-6) The $YO_{1.5}$ -BaO-CuO pseudoternary phase diagram at $950^\circ C$ in air. The tie lines indicate that the 123 phase is stable with the 211, CuO, and $BaCuO_2$ phases at $950^\circ C$. These are the common impurity phases detected when trying to form 123. Phase diagram from Beyers and Ahn[.].	20

- Figure 2-7) Space model of the YBCO phase diagram with the primary crystallization field for 123 shaded. Note that this field is quite small and is Ba- and Cu- rich with respect to the 123 composition. Phase diagram from Maeda et al.[65].....22
- Figure 2-8) Vertical binary slice of YBCO pseudoternary in air (Figure 2-6). Phase diagram from Murakami et al.[]23
- Figure 2-9) Schematic diagram of 123 grain nucleation and growth. Note that the growth of 123 shell around the 211 hinders completion of the peritectic reaction. Diffusion and growth is much faster in the ab plane than in the c-direction.....25
- Figure 2-10) Typical microstructure of a melt-textured YBCO grain, viewed under polarized light. The primary twinned phase is 123. Because the twin traces are $\sim 90^\circ$ from each other, this indicates that the c-axis is approximately normal to the sample surface. The darker, elliptical second phase, with around 30% of the volume, is 211.....25
- Figure 2-11) Cracks (or gaps), originally thought to be platelet twist boundaries, are indicated by the arrows. The twin trace pattern (the smaller angle between the twins is less than 90° but greater than 0°) indicates the c-axis of the sample is inclined from the sample surface (see Figure 2-3) and hence the cracks in the ab-plane are visible.26
- Figure 2-12) A drawing illustrating that the lines in the ab direction of melt-textured 123 are not grain boundaries but gaps as a result of the growth process filled with second phase, such as CuO,[69] or cracks due to the tetragonal to orthorhombic transition[70,71]. They do not extended across the width of the sample, and so current can flow along the c-axis of the specimen without crossing a grain boundary. Drawing adapted from Alexander et al.[69].....26
- Figure 2-13) A simple drawing of the melt-out, melt-texturing process before texturing begins. The sintered 123 bar is melt-textured on a 211 bar. During melt-texturing some 30-40% of the liquid, including possible impurities, is wicked into the porous, low density 211 block. Drawing adapted from Willen and Salama[95].....30
- Figure 2-14) Typical V-I traces for a strongly-coupled 90° grain boundary. The key feature is that low applied magnetic fields do not diminish the I_c . Plot taken from Babcock et al.[4]32
- Figure 2-15) Plot of the smooth flux-flow V-I characteristic of a strongly-coupled melt-textured 5° grain boundary at 0.4T and 77K.....33
- Figure 2-16) Plot of V-I curves of UW melt-textured high angle (55° [$\bar{2}$ 3 $\bar{1}$]) bicrystal MB4C1. Low magnetic fields greatly decrease the supercurrent from the zero field value, and the resistive transition is ohmic.....34

- Figure 2-17) a) Two cubic crystals are misoriented by θ about [001]. b) When the crystals are joined, the mismatch can be accommodated by elastic strain and edge dislocations (\perp) spaced b/θ , where b is the burgers vector. Drawing from Read[105].37
- Figure 2-18) Plot of dislocation spacing in a [001] tilt grain boundary as a function of misorientation angle for two different burgers vectors observed by I-Fei Tsu[104]. Plot from Tsu[104].38
- Figure 2-19) The graphical definition of Σ . The left image shows the atomic positions that comprise the two crystal lattices of the grains of a bicrystal. The right image shows the overlap the atoms from one grain of a bicrystal onto the other grain, and a pattern of coincident points that may appear. The number of atoms that comprise each coincident cell is the Σ value, the lower the number indicating the higher the coincidence. Figure from Merkle[.].....41
- Figure 2-20) Schematic plot of grain boundary energy vs. misorientation angle. At certain higher angle misorientations there exists special low energy grain boundaries. Plot adapted from Chan[.].42
- Figure 3-1) The melt-texture process: plot of temperature vs. time, based on the procedure developed by Salama et al.[5]. The quick initial heating creates a melt of 211+liquid. The key grain growth step is the 50 hrs. slow cool through the peritectic. Oxygenation occurs below 600°C.45
- Figure 3-2) Polarized light micrograph of the amorphous non-superconducting and BaCuO₂ and CuO phases resulting from an incomplete peritectic reaction during resolidification from the melt (light gray in the image). The majority, matrix-phase is YBCO.....47
- Figure 3-3) The circled regions of this polarized light micrograph highlight large, amorphous, non-superconducting phases at the grain boundary. Contamination at this size scale will clearly result in an insulating grain boundary.....47
- Figure 3-4) Polycrystalline melt textured sample from AT&T[44], thinned and polished, and viewed under polarized light. The different regions of contrast represent grains of different orientation. The very small dots are 211, and the larger circles are voids. ..49
- Figure 3-5) Polarized light micrograph of the top and bottom surfaces of sample SJ3151B3, which has been thinned to 50 μ m. The boundary goes completely through the sample.....50
- Figure 3-6) Polarized light micrograph of a melt-textured sample from AT&T[44] that was polished in bar form on four sides. Placing these images together, one can choose a direction to polish from so as to isolate a desired bicrystal.....51

- Figure 3-7) A melt-textured high angle grain boundary (MT4C2.2 - $57^\circ[\overline{17} \ \overline{11} \ 2]$) viewed under polarized light. Twins do not intersect at 90° , indicating that both grains have inclined c-axes. The grain boundary plane is macroscopically wavy.....53
- Figure 3-8) Schematic diagram of the x-ray pole figure apparatus showing how the key angles θ , χ , and ϕ are related to the x-ray source, detector, and sample.55
- Figure 3-9) Schematic diagram to show how rotations of ϕ produce Bragg reflections which lie on a conical surface. Maximum χ in reflection mode is $\sim 80^\circ$ and ϕ rotates the full 360° for each χ56
- Figure 3-10) Automatic “raw” pole figure data for sample MB4C1. The location and width of the labeled poles are used to approximate the pole centroids. They are then located manually by scanning in 1° increments.58
- Figure 3-11) A 2θ scan for the (006) pole of a sample (MB4C1) located at $\chi=62^\circ$ and $\phi=277^\circ$ shows a peak intensity of ~ 2100 counts per second at $2\theta=46.6^\circ$59
- Figure 3-12) Map showing the centroid of a c-axis via the peak counts per second values (X =not measured) at an experimentally determined $2\theta=47^\circ$ for sample KS4B2. The centroid is at $\chi=78^\circ$, $\phi=98^\circ$, width $\sim \pm 1^\circ$59
- Figure 3-13) Polarized light micrograph of a UW MT sample was not measured because of the crack which extended across both grains.62
- Figure 3-14) Schematic diagram of the AC T_c experimental system. The sample is cooled in a He gas filled rig, down to either 77K or 4K. The temperature sensor in the rig is read by the temperature controller and relayed to the computer chart recorder. The voltage signal (at the same frequency and phase as a generated current of a known level) is read by the lock-in amplifier and sent to the computer chart recorder. Data is displayed as voltage versus temperature, but this is easily converted to resistance versus temperature as the current level is preset.....63
- Figure 3-15) Schematic diagram of the DC V-I measurement setup. A ramp controller manually triggered a BOP to provide the current for the sample while a DC voltmeter read the response.....64
- Figure 3-16) Plot of $J_c(B,\theta,77K)$ characteristics for melt-textured bicrystals at low magnetic fields. Zero field J_c decreases and the field dependence of J_c increases with increasing misorientation.....66
- Figure 3-17) High field residual critical currents measured in five melt-textured high angle boundaries at 4K. Higher angle boundaries tend to have lower J_c values.....67
- Figure 3-18) A typical AC Resistive T_c trace across a melt-textured boundary (sample MB4C3b). The T_c onset is at $\sim 91K$, with zero resistance occurring at $T=90.2K$68

- Figure 3-19) For sample SJ3151B3 the T_c onset is at 91K, but a resistive tail, believed to be due to dissipation at the grain boundary, is visible down to 88K for a measuring current of 10mA ($J \sim 100A/cm^2$).....69
- Figure 3-20) Two bicrystals exhibited a sharp low field depression of J_c but then exhibited a much slower fall off in strong fields at 77K (B is not $\parallel c$ for either sample).....71
- Figure 4-1) Illustration of seeded melt-textured bicrystal growth. Single crystals of aligned Y-123 grow from the Sm-123 seeds and create a grain boundary dictated by the misorientation of the Sm-123 seeds.....79
- Figure 4-2) Polarized light micrograph of the wiring of a typical laser-isolated bicrystal (KS4B1a). The sample is only $85\mu m$ thick and $370\mu m$ wide, but $\sim 3.5mm$ long, allowing space for four voltage taps. Note that the current leads are large and designed to feed current into the whole cross-section of the sample.....80
- Figure 4-3) Gold pads, $\sim 50-100\mu m$ in diameter were sputtered on the surface through a copper grid in an attempt to get lower contact resistivity (Sample KS4B1c).....81
- Figure 4-4) Schematic diagram of pulsed current experimental circuit. The computer triggers the function generator which defines the shape of the pulse. The function generator then creates the current pulse through the bi-operational power supply.82
- Figure 4-5) Plots of the current pulse and voltage response vs. time. The voltage response to the 1ms pulses has both a leading and trailing inductive spike. The choice of voltage measuring window results in a tradeoff between voltage noise and voltage baseline. Plots adapted from Edelman[136].....83
- Figure 4-6) Schematic diagram of the high sensitivity V-I experimental setup. The key feature is the Keithley voltmeter/preamp combination which can achieve nV sensitivity under optimal conditions.....84
- Figure 4-7) Plot of intergranular $J_c(B, 77K)$, determined by pulsed V-I measurements for MOMT samples of general misorientation of 5° through 38° . Inset shows details of the low field behavior.....88
- Figure 4-8) Plot of the intergranular critical current density in magnetic field, $J_{c(g.b.)}(B)$, expressed as a ratio of the zero field value at 77K for the samples of general misorientation (5° through 38°).....89
- Figure 4-9) A comparison of the intergranular J_c of the $38^\circ[3\ 1\ 1]$ Boeing bicrystal and the $38^\circ e[15\ -14\ 1]$ MOMT bicrystal.....91
- Figure 4-10) Plot of the intergranular log V-J characteristics for sample 11^b at 77K($H \sim \parallel c$).....93
- Figure 4-11) Plot of intragranular (grain B) log V-J characteristics for sample 11^b at 77K($H \sim \parallel c$).....94

- Figure 4-12) Plot of intergranular log V-J characteristics for sample 38°e at 77K.95
- Figure 4-13) Plot of intragranular (grain B) log V-J characteristics for sample 38°e at 77K.96
- Figure 4-14) a) Polarized light micrograph of the 5° bicrystal b) reflected light MO image at 15K in 40mT. The c-axis of each grain is ~9° from surface plane. Flux penetrates preferentially along cracks between platelets and at large 211 particles but not at the GB98
- Figure 4-15) Polarized light micrograph of the 11°c bicrystal b) reflected light MO image at 15K in zero field after field cooling in 40mT. Regions A, B, and C pin flux better than adjacent segments of the boundary100
- Figure 4-16) a) Polarized light micrograph of the GB in sample 14°b. b) Magneto-optic image of the same region. The image was taken after being field cooled to 8K in 40mT.102
- Figure 4-17) Smoothed data from pulsed V-I traces on 14°b as a function of magnetic field. There is a sharp decline in the I_c in low magnetic fields, but the inset highlights a far less field-dependent I_c103
- Figure 4-18) Polarized light micrographs of sample 7°a and 7°b. The grain boundary in 7°a is curved while the GB in 7°b has two ~90° kinks. Applied current direction is along the long sample dimension as indicated.105
- Figure 4-19) A plot of the ratio of the intergranular $J_c(B)$ vs. the lower intragranular $J_c(B)$ for samples 7°a and 7°b at 77K.106
- Figure 4-20) Polarized light micrographs of samples 11°a, b, and c. The boundary planes in 11°a and 11°b have similar inclinations to the samples' long axis, while 11°c is nearly normal to the long axis. Applied current direction is along the long sample dimension as indicated.107
- Figure 4-21) Plot of the $J_c(B, 77K)$ characteristic for samples 11°a, b, c.108
- Figure 4-22) Polarized light micrographs of samples 38°a, c, d showing the different grain boundary plane inclinations. Current direction is along the long sample dimension.109
- Figure 4-23) Schematic drawings of three models for explaining the GB J_c in thin film [001] tilt YBCO as a function of GB structure: a) The dislocation core model [14,15], before and after core overlap, b) The Dayem bridge model[141], and c) Two channel model[42,146].114
- Figure 4-24) Schematic representations of the possible microstructure viewed in the GB plane (GB normal is out of the paper) of a) the prison bar model of a simple [001] tilt boundary. The black regions are the dislocation cores, the gray are the areas near the

cores that are degraded due to strain, while the white areas represent undisturbed lattice. Note the large 2-D rectangular regions of this undisturbed lattice. b) General misorientation GB, composed of a grid of 4 sets of dislocations, results in a geometrical network of essentially point, rather than line contacts (adapted from Miranova et al.[150]). 116

Figure 4-25) Plot of the $J_{c(g.b.)}(B=0, 77K)$ values for flux-grown (\square [20,152]), melt-textured (UW/AT&T MT - \odot [22], MOMT - \odot [33], UW MT - ∇ [22], Boeing seeded - \diamond [151], Argonne seeded - \triangle [93]) and thin film (Ivanov et al. - \bullet [153], Heinig et al. - \blacklozenge [146]) bicrystals, as a function of general misorientation angle. 117

Figure 4-26) Plot of the ratio of the intergranular to intragranular critical currents (0T, 77K) for melt-out samples (\bullet, \odot), in comparison to other general misorientation, UW melt-textured samples previously measured at 77K(∇)[22],(\blacklozenge)[151], Argonne seeded melt-textured bicrystals (\blacklozenge)[93], UW/NIST [001] tilt bulk flux-grown bicrystals at 77K(\triangle)[20,152], thin film samples of mixed misorientation at 5K(\square) by Dimos et al.[14], [001] tilt thin film samples at 77K(\circ) by Heinig et al.[146], and [001] tilt thin film samples at 77K(Δ) by Ivanov et al.[153]. Symbols with white crosses indicate that the intragranular J_c was estimated, while all other samples had measured intragranular J_c values. Second order regression fits to all the bulk scale and thin film data illustrate that bulk scale grain boundaries tend to have a weaker decline of $J_{c(g.b.)}$ with increasing misorientation angle than the thin film boundaries. 119

Figure 4-27) Plots of the ratios of the intergranular to intragranular critical currents as a function of applied magnetic field at 77K: a) $J_c(B)$ for the inter and intragranular regions of sample 7°a with $B \sim \perp c$, b) The ratio of intergranular I_c to intragranular I_c with $B \sim \perp c$, c) $J_c(B)$ for the inter and intragranular regions of sample 7°a with $B \sim \parallel c$, d) The ratio of intergranular I_c to intragranular I_c with $B \sim \parallel c$ 122

Figure 5-1) Plot of the estimated $J_{c(g.b.)}/J_{c(grain)}(77K)$ ratios at zero field for IBAD tapes (\bullet)[155] vs. thin film (TF) bicrystals (\circ)[146,153]. The intragranular J_c value for IBAD tapes is estimated at $2 \times 10^6 A/cm^2$, a standard YBCO TF value[152]. The IBAD ratios are consistently higher than the TF ratios above 10° 126

Figure 5-2) Plot of the estimated $J_{c(g.b.)}/J_{c(grain)}(77K)$ ratios at zero field for IBAD tapes (\bullet) vs. bulk bicrystals (\circ , flux grown[20,152] and melt-textured[22,151,93]). The IBAD ratios lie among the bulk bicrystal ratios. 127

Figure A-1) a) Schematic drawing of a general misorientation grain boundary with a flat grain boundary plane. b) The misorientation between crystal abc and a'b'c' in a) can be described by a rotation angle θ about a rotation axis \underline{u} that sets both crystal coincident. The grain boundary normal \underline{n} is independent of θ and \underline{u} 130

- Figure A-2) a) Drawing of a tilt grain boundary: the rotation axis is perpendicular to the grain boundary plane normal ($\underline{u} \perp \underline{n}$). b) Drawing of a twist grain boundary: the rotation axis is parallel to the grain boundary plane normal ($\underline{u} \parallel \underline{n}$). 133
- Figure A-3) Graphical definition of the Euler angles (Θ , Φ , and Ψ). The misorientation between two crystals of axes xyz and $x'y'z'$ can be described by a rotation about z , followed by a rotation about x'' , and then a rotation of about z' . Figure adapted from Randle[118]. 135
- Figure A-4) Pole figure data plotted on a stereographic projection, with each point a centroid of the labeled pole. The orthorhombic structure of YBCO constrains which pole belongs to which crystal. 137
- Figure A-5) A Wulff net, used to measure angles from a stereographic projection. The longitudinal lines are known as the “great circles.” 138
- Figure A-6) The poles marked on Figure A-4 are rotated so that the c' and c poles lie on the same great circle. Then the misorientation angle between c and c' can be determined by noting the angular distance on the great circle ($\theta_{cc'}=41^\circ$). 140
-
- Figure B-1) Schematic drawing of the thermoevaporation process from ref.[159]. Laser beam first melts the material and then heats the liquid until the vapor phase is formed and ejected from the cut. 142
- Figure B-2) Plot of ablation depth per laser shot as a function of laser wavelength, from ref.[161]. 144
- Figure B-3) Drawing of the Florod Nd:YAG laser, from the Florod LMS Manual[]. This assembly is mounted with the tilt plate attached to the top port of a long working distance Mitutoyo microscope. 145
- Figure B-4) An unpolarized light micrograph of a melt texture sample cut with a Nd-YAG laser a) before and b) after cleaning with methanol. The discoloration surround the cut in the first image is due to re-deposit material from the cut, and is not sample damage. 146

Index of Tables

Table 3-1: Summary of misorientation, T_c , grain boundary J_c electromagnetic coupling, and grain boundary resistivity ($\rho_n d$) for UW and AT&T manufactured MT bicrystals.	65
Table 4-1: Misorientation angle, common axis and illustrative electromagnetic data for various bicrystals.	87
Table 4-2 Comparison of irreversibility fields of the grain boundary and the grains for various MOMT bicrystals at 77K.	97
Table B-1: Bouguer's constants for different laser wavelengths[160].	144

Chapter 1 : The Challenge: Bulk Conductor Applications for $\text{YBa}_2\text{Cu}_3\text{O}_{6+x}$

The main obstacle on the road to practical bulk conductor applications of the superconductor $\text{YBa}_2\text{Cu}_3\text{O}_{6+x}$ ("YBCO") is the inability to pass large supercurrents ($\sim 10^5$ - 10^6 A/cm^2) through this material's grain boundaries in the presence of strong magnetic fields. The material, a black, brittle, complex copper-oxide discovered in 1987[1], has a critical temperature above the 77K boiling point of liquid nitrogen ($T_c=92\text{K}$), as well as an extremely high upper critical field ($H_{c2}(77\text{K}) \gg 10\text{T}$ for fields in the ab plane). It also has strong vortex pinning even at 77K in significant magnetic fields ($>1\text{T}$), as shown by its superior irreversibility field (the magnetic field above which J_c becomes zero) behavior in comparison to other ceramic high temperature superconducting oxides: $\text{Bi}_2\text{Sr}_2\text{CaCu}_2\text{O}_8$ (Bi-2212), $\text{Bi}_2\text{Sr}_2\text{Ca}_2\text{Cu}_3\text{O}_{10}$ (Bi-2223) and $\text{La}_{1.85}\text{Sr}_{0.15}\text{CuO}_4$ (**Figure 1-1**)[2], as well as the Tl- and Hg- based superconducting ceramic oxides. Although the brittle nature of YBCO presents a serious challenge to manufacture of a flexible conductor form, various fabrication methods, such as the powder-in-tube process[3], overcome this obstacle. Intragranular current densities in the bulk forms of YBCO are generally good; they range from $\sim 10^3 \text{ A/cm}^2$ in flux-grown single crystals[4], to $\sim 10^4$ - 10^5 A/cm^2 for melt-textured material[5,6], and up to 10^6 A/cm^2 in thin film single crystals[7].

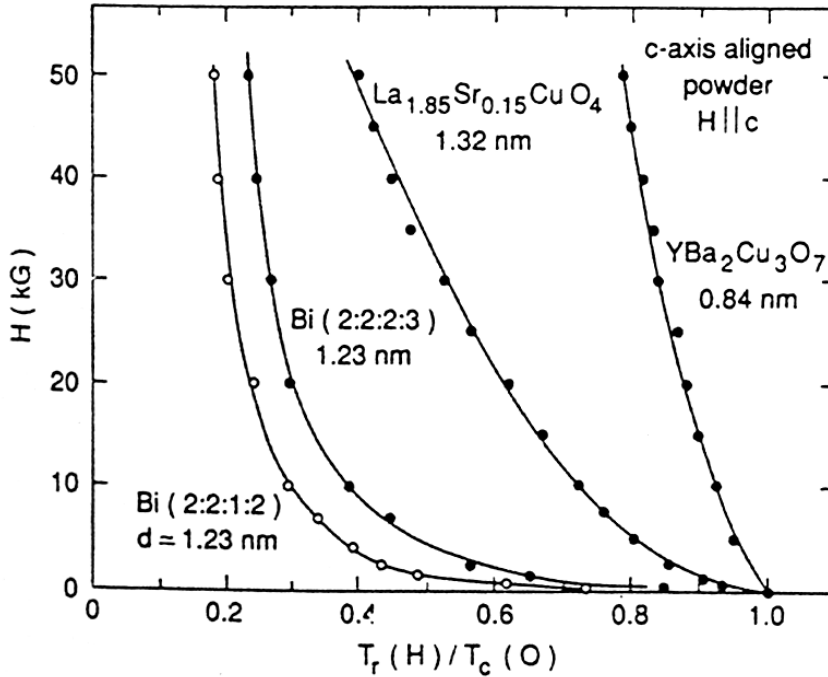


Figure 1-1) The irreversibility fields, a measure of the vortex pinning strength, as a function of temperature fraction of T_c for YBCO, Bi-2212, Bi-2223, and La-214. Plot from Suenaga et al. [2].

However, a major problem remains for YBCO. This is its inability to carry usable critical current densities (i.e., $> 10^5 \text{A/cm}^2$) across misaligned grains. Deutscher and Müller[8] predicted that since the coherence length ($\xi_{0(ab)} \sim 16 \text{\AA}$, $\xi_{0(c)} \sim 2 \text{\AA}$)[9] is of the same order as the grain boundary thickness, the atomic scale grain boundary disorder would severely depress the superconducting order parameter at the grain boundary. Indeed, bulk polycrystalline material has poor transport J_c despite good intragranular magnetization J_c [10]. However, granularity has not been as severe a problem in the Bi-compound family despite similarly small coherence lengths (e.g., Bi-2212: $\xi_{0(ab)} \sim 30 \text{\AA}$, $\xi_{0(c)} \sim 4 \text{\AA}$, 77K)[11]. This improved behavior is believed to be simply a result of the micaceous properties of the

double Bi-O layers in BSCCO compounds, which allows them to be textured to a high degree (i.e., the grains are better aligned) by a series of rolling and heat treatment steps[12]. It is an open question whether there are intrinsic differences in the nature of the grain boundaries in YBCO and BSCCO.

The first experiments to show explicitly the influence of the grain boundary on YBCO current transport, specifically the effect of the misorientation of two crystals across a grain boundary, were those of Dimos et al.[13,14]. By using thin films grown on SrTiO₃ bicrystal substrates of controlled misorientation angle, they demonstrated a strong relationship between the J_c and misorientation angle of either [100] twist, [001] and [100] tilt bicrystals (**Figure 1-2**). They concluded that grains misoriented by more than $\sim 5^\circ$ - 10° are always weakly-coupled. This was inferred from measurements of the ratio of the zero field intergranular to the intragranular critical current densities ($J_{c(g.b.)}(0T,5K)/J_{c(grain)}$), which showed ratios of the order 0.01-0.05 for high angle boundaries, as compared to a 0.5-1 ratio for low angle grain boundaries (**Figure 1-3**). They further proposed that all YBCO grains misoriented by more than $\sim 5^\circ$ - 10° are intrinsically weak-linked, because the grain boundary acquires a suppressed order parameter produced by the grain boundary dislocation core overlap. While the physical size of these dislocations does not suggest an effective overlap until $\sim 20^\circ$, it was also proposed that the strain fields associated with the dislocations can increase their effective diameter so as to cause overlap at $\sim 10^\circ$ [15], provided that the boundary does not relax to a lower strain configuration. Other studies on

thin film Bi and Tl-2212 bicrystals have shown similar $J_{c(\text{g.b.})}(\text{OT})/J_{c(\text{grain})}$, results[16,17], resulting in strongly suppressed $J_c(\text{OT}, 77\text{K}(\text{Tl}), 4\text{K}(\text{Bi}))$ above $\sim 10^\circ$ [001] tilt.

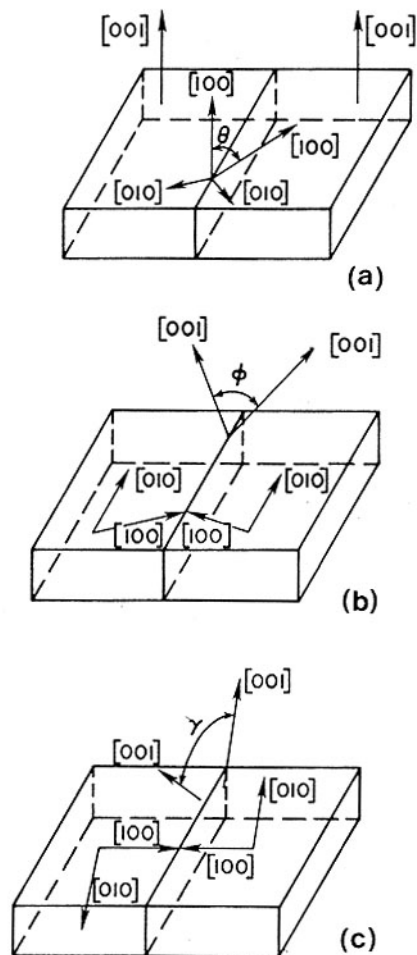


Figure 1-2) Drawings illustrating the thin film YBCO grain boundary geometry of Dimos et al.[14]: a) [001] tilt b) [100] tilt c) [100] twist.

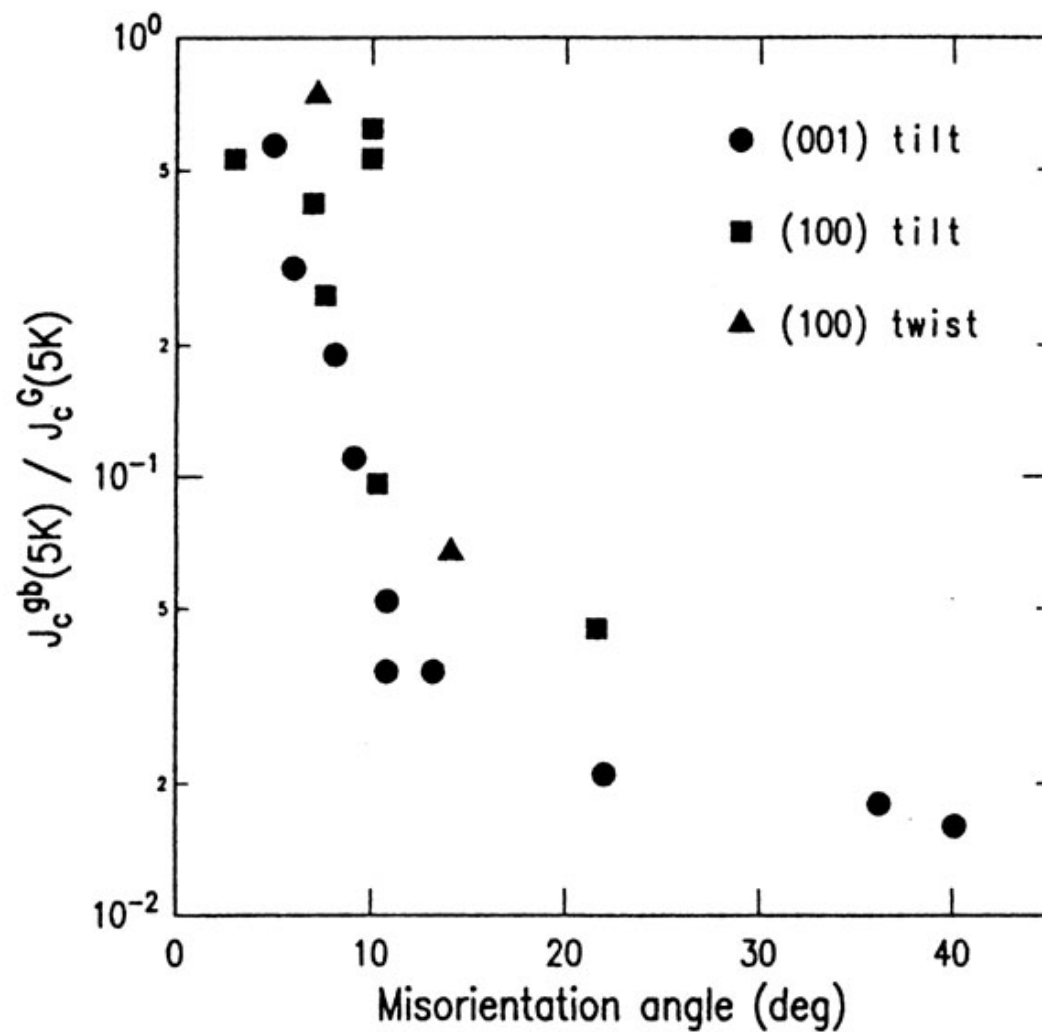


Figure 1-3) The plot of the ratio of the intergranular to intragranular critical current densities for YBCO thin films on SrTiO₃ with three different primary misorientation geometries {● - (001) tilt, ■ - (100) tilt, ▲ - (100) twist}, at 5K and no applied magnetic field, from Dimos et al.[14].

The generality of these conclusions, especially the small value of the crossover misorientation angle from strong to weak coupling, was put in some doubt by subsequent work done at the University of Wisconsin on bulk-scale, flux-grown YBCO bicrystals. Babcock et al.[4] showed two high angle grain boundaries ($14^\circ[001]$ tilt and $90^\circ[010]$ tilt and twist) to be strongly-coupled (**Figure 1-4**). Eom et al. later showed that $90^\circ[010]$ tilt thin films were also strongly-coupled[18,19]. This strong-coupling is indicated by an intergranular $J_c(B)$ that is similar to the intragranular $J_c(B)$, in that it is insensitive to low magnetic fields and has a similar decay in high applied fields. Larbalestier et al.[20] later showed evidence for weakly-coupled, or Josephson Junction (JJ), behavior and strongly-coupled, or flux-pinning (FP), behavior for different bicrystals of the same misorientation (e.g., $14^\circ[001]$ tilt). Recently, the variability of the $J_{c(g.b.)}(0T,77K)/J_{c(grain)}$ was shown by Heinig et al.[21] for 7° YBCO thin films made with the same growth parameters and the same substrates. These results demonstrate that the explanation for grain boundary properties cannot be as simple as Dimos et al.[14] proposed. Thus the grain boundary properties are not only a function uniquely defined by their misorientation, and $\sim 5^\circ$ - 10° of misorientation is not necessarily the strong-coupling limit.

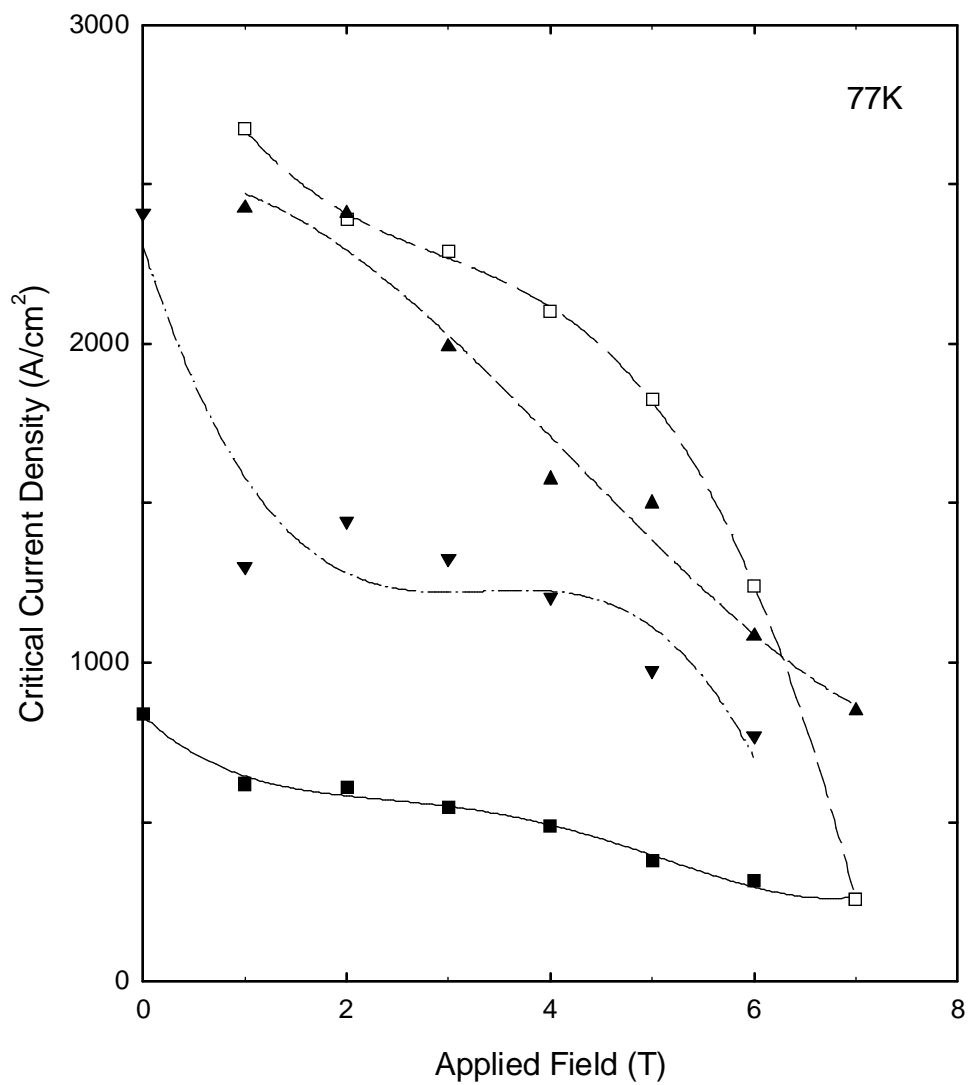


Figure 1-4) Plot of transport $J_c(B)$ for flux-grown bulk YBCO bicrystals with $H//c$, 77K for an intragranular region (▲), and the 3°[001] tilt (□), 15°[001] tilt (■), 90°[010] part tilt/part twist (▼) bicrystals. Adapted from Babcock et al.[4].

Further investigation of certain bulk samples revealed that, a nearly field-independent, though small, critical current component remained[20,22] for magnetic field-sensitive, Josephson-like boundaries even at high fields. This residual critical current is not well explained as a property of a typical Josephson Junction, as few reports on low T_c JJ addressed high field properties directly. A report by Yanson[23] did show experimentally that structural inhomogeneities in a Sn-Sn tunnel junction resulted in a plateau in the $J_c(B)$ character, in direct contrast to the typical Fraunhofer-like $J_c(B)$. More recently, Bulaevskii et al.[24] extended this analysis to the high field case to develop a “brick wall” model of current transport in Bi-oxides c-axis JJ boundaries, where the observed macroscopic transport current in Bi tapes is the residual current of the c-axis JJ. Another feasible explanation is that high angle grain boundaries have a small strongly-coupled path, in parallel with a majority weakly-coupled connection.

The variety of behavior exhibited by grain boundaries of similar misorientations shows that misorientation is not the only factor controlling boundary character, thus focusing attention on other possible variables. One such factor that is not yet well understood is the role of impurities and other composition variations at the grain boundary. The atomic disorder of the grain boundary permits rapid diffusion of oxygen, as well as permitting impurity contamination. Local oxygen deficiency has been shown to be important, as grain boundary regions have been correlated with weak-coupling by electron energy loss spectroscopy[25]. Impurity segregation effects are potentially important because of the possibility of SrTiO₃ substrate contamination in thin film bicrystals and the

potential for CuO-BaCuO₂ contamination from the flux in flux-grown bicrystals. These two systems have provided the source material for most of the experiments on grain boundary behavior. Thus, it would be more desirable for probing the intrinsic grain boundary disorder effects on the electromagnetic properties of bicrystals to obtain boundaries that are produced in a less contaminant-rich environment.

How are these results relevant to bulk scale applications of YBCO? Bulk scale applications of any high temperature superconductor almost certainly require that some degree of misorientation from one grain to another be tolerated. In the past few years, several methods of combating the granularity of YBCO by various texturing routes have been demonstrated. The most dramatic has been the Ion Beam Assisted Deposition (“IBAD”)[26] process. On a randomly oriented Ni-alloy (Hastelloy) tape, a biaxially textured yttrium-stabilized zirconia (YSZ) film is sputtered with one ion beam (Ar⁺), while a second, assisting ion beam (O+Ar) bombards the film to induce texture. A YBCO film of up to ~1μm thickness is then deposited on the YSZ. Such tapes can have J_c(75K, 0T)~10⁶A/cm² with little evidence of weak links in magnetic fields[27]. It is important to note that the YBCO in IBAD tapes is not fully aligned; rather full width at half maximum (FWHM) of the (103) rocking curves of the YBCO range from 10.5°[27], to as high as 20°-30°[26]. It should be noted that the creation of the aligned YSZ substrates is quite time consuming.

Another promising report involves the use of textured metal substrates created by rolling, called Rolling Assisted Biaxial Textured Substrates (“RABiTS”)[28]. It involves a

textured substrate, presently Ni, which has been cold rolled and recrystallized to a sharp cube texture. This is followed by depositing a layer of the noble metal Pd and then CeO₂ and/or YSZ as an appropriate aligned deposition template for the YBCO. The resultant substrate has 95% of the grain boundaries with misorientations of 10° or less. A 0.75μm thick film had a $J_c(77K, 0T)=3 \times 10^5 A/cm^2$. While the J_c is not quite as high as IBAD, it should be technologically simpler to scale up.

The third promising report on texturing of YBCO is a thick film approach, called Magnetic Field/Liquid Assisted Texture (“MFLAT”)[29]. It involves the high field (7T) magnetic alignment of YBCO thick films during partial melting on silver. While the critical current densities are more modest, $J_c(77K, 3T)=2 \times 10^3 A/cm^2$, they involve samples of much larger grain size (dimensions of tens to several hundred μm) and total thickness (1mm). Thus the I_c values are larger than samples made by the IBAD and RABiTS techniques, with ~100A for MFLAT, in comparison to 50A for IBAD, at 77K and 1T[30]. The thick film J_c values of the MFLAT process are a significant improvement across grain boundaries in sintered YBCO with similar grain dimensions, and the FWHM of the (103) rocking curve is 9°[31].

These positive reports underscore the importance of studying and understanding the electromagnetic properties of grain boundaries of general misorientation. These samples have misorientations with significant tilt and twist components, yet the bicrystal experiments in the past have focused on the geometrically simpler thin film (TF) and flux-grown (FG) bicrystals. This was because the grain boundary misorientations can be clearly

defined, compared to existing grain boundary models, and the samples are suitable for high resolution transmission electron microscopy (HRTEM). How well the simpler geometries can be used to predict behavior in the more general misorientations is not well known. In fact, there is evidence to suggest that the behavior in the general misorientation bicrystals may be less sensitive to misorientation than TF bicrystals, despite their more complex geometry[32,33]. Other researchers have investigated general misorientation boundaries in the YBCO family[34,35,36,37,38,39,40,32,41], but the work presented here provides the most thorough and complete combination of misorientation and electromagnetic analysis to date on these types of grain boundaries.

The organization of the thesis is as follows: in **Chapter 2** I will present background information on sample processing, the electromagnetic definitions of coupling character, and brief explanations of the grain boundary models used in describe superconducting bicrystals. In **Chapter 3** I will describe the experimental procedures and discuss the results of the initial UW melt-textured YBCO experiments, during ~1990-1994[22]. In **Chapter 4** I will describe the second round of melt-textured experiments, featuring “melt-out” samples, analyzed from ~1994-1996[42,43,33]. I will then attempt to draw conclusions from both sets of data, with a look towards the implications towards the future of YBCO bulk applications. Appendices on crystallographic misorientation descriptions and laser cutting of YBCO are included for reference.

Chapter 2 : $\text{YBa}_2\text{Cu}_3\text{O}_{6+x}$: Processing, Electromagnetic Behavior and Grain Boundaries

The initial goal of my thesis was to perform electromagnetic experiments on sintered bulk YBCO similar to the thin film experiments by Dimos et al.[14]. The motivation was that the magnetic field dependence of J_c for bicrystals had not been studied, and that thin film results might not be representative of the true nature of intergranular coupling in YBCO, perhaps due to substrate contamination of the thin film grain boundaries. Grains in sintered YBCO could be grown only as large as $\sim 100\text{-}250\mu\text{m} \times 50\mu\text{m} \times 50\mu\text{m}$, and were part of a three-dimensional polycrystalline matrix (**Figure 2-1**). To attempt a bicrystal experiment, samples would have to be thinned to $\sim 50\mu\text{m}$ and isolated from adjacent grains, a difficult feat on this brittle compound. Around this time, a process called melt-texturing[44] was developed for creating large grains of YBCO. Grains could be grown with dimensions on the millimeter size scale, greatly easing the difficulty of isolating single grain boundaries. Before the details of such experiments are described, it is useful to review knowledge about the YBCO phase diagram and the processing techniques that lead to the development of the materials examined herein.

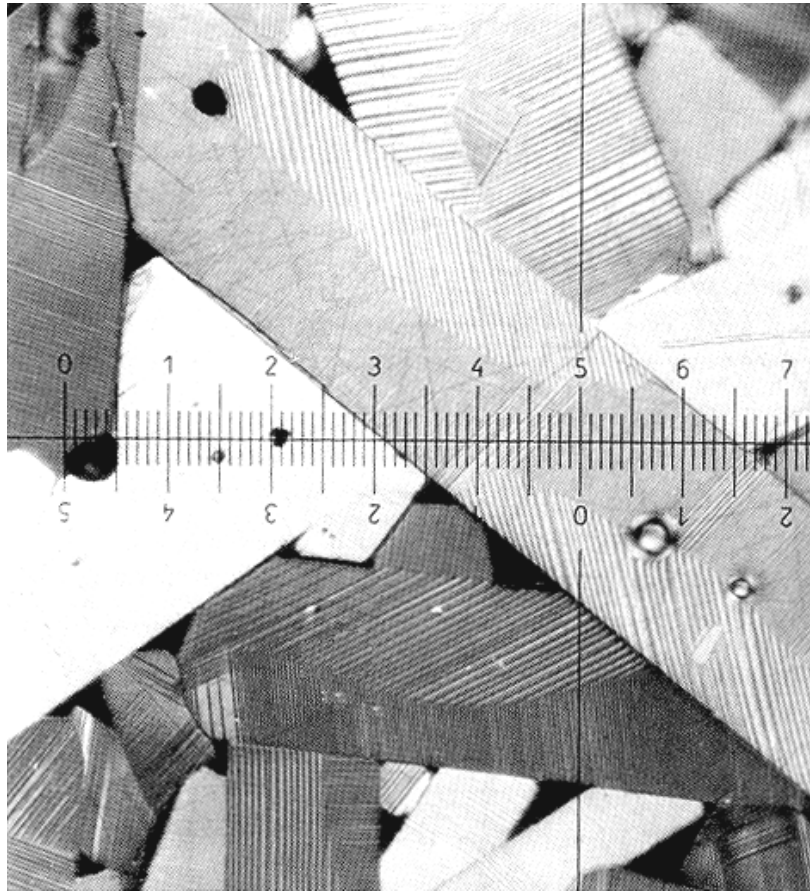


Figure 2-1) The typical microstructure of polycrystalline sintered YBCO, view under polarized light, from Verhoeven[45]. The brightness contrast between the grains is due to the crystal misorientation, and the striations visible within the grains are twin boundaries (major tick=10 μ m, minor tick=1 μ m).

In describing the electromagnetic character of grain boundaries, terms like “weak-links”, “strong-coupling”, “weak-coupling”, etc. are often used in a confusing and non-standard manner in the literature. It is therefore useful to review the definitions of these terms and the conditions under which they should be applied.

The influence of microstructure on properties has been well established in material science. To this end, it will be helpful to introduce some of the grain boundary

microstructural models used to explain the electromagnetic characteristics seen in past bicrystal experiments, and what might be expected for the more complicated general misorientation grain boundaries that are the subject of this thesis.

The $\text{YBa}_2\text{Cu}_3\text{O}_{6+x}$ Phase Diagram

The $\text{YBa}_2\text{Cu}_3\text{O}_{6+x}$ (“123” or “YBCO”) compound was discovered in 1987[46], shortly after the discovery of the first high T_c ceramic superconductor, $(\text{La,Ba})_2\text{CuO}_{4+x}$ [47]($T_c=38\text{K}$). When fully oxygenated, i.e. when x approaches 1, T_c approaches 92K (as most research is done on oxygenated samples, $x>0.9$, many researchers also refer to the 123 compound as $\text{YBa}_2\text{Cu}_3\text{O}_{7-\delta}$, where $\delta<0.1$). The 123 phase has a perovskite structure[48], defined as the basic compound formula ABX_3 , where A and B are metallic cations and X is a non-metallic anion (**Figure 2-2**). The superconducting phase is orthorhombic ($a=3.819\text{\AA}$, $b=3.886\text{\AA}$, $c=11.68\text{\AA}$ [49]), and the de-oxygenated, insulating phase tetragonal ($a=3.589\text{\AA}$, $c=11.84\text{\AA}$ [50]). The tetragonal to orthorhombic transition, occurring during the cool from 123 phase formation, results in the formation of twin boundaries along the (110) and $(1\bar{1}0)$ planes. Macroscopic clusters of twin boundaries can be seen in polarized light micrographs. They are the signature of the orthorhombic 123 phase (**Figure 2-1**). Twin intersections at 90° generally indicate that the c -axis is perpendicular to the viewing plane, although it is possible that the viewing plane contains $[110]$ or $[1\bar{1}0]$ (but (001) is the far more common cleavage plane). Parallel twin

traces indicate that the c-axis is in the viewing plane, and an intermediate twin boundary angle indicates an intermediate inclination[51] (**Figure 2-3**).

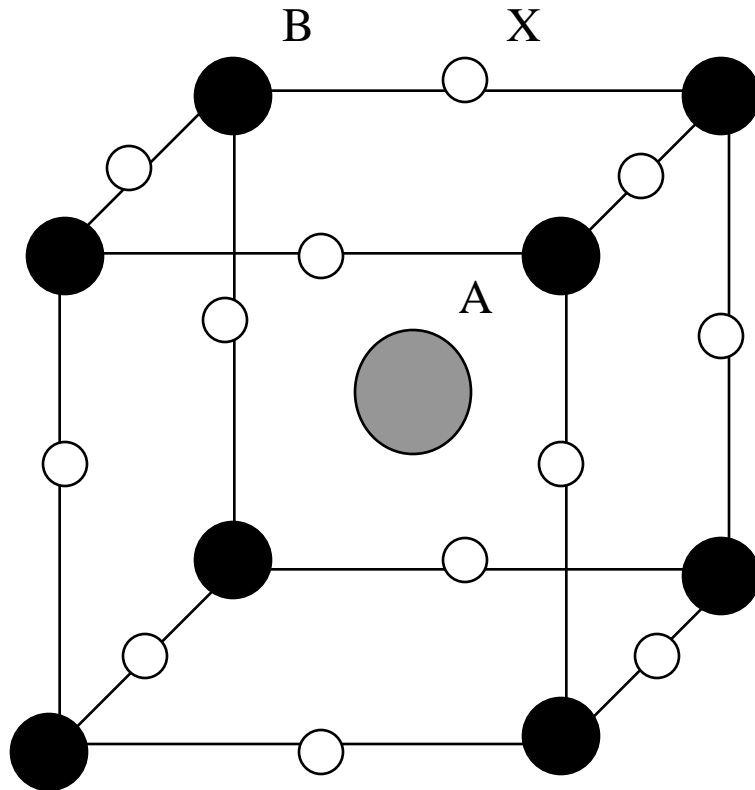


Figure 2-2) Drawing of the perovskite crystal structure, where A and B are metallic cations and X is a non-metallic anion. The YBCO unit cell is composed of three of these perovskite unit cells stacked: the center cell has Y as the A cation, and the top and bottom cells have Ba as the A cation. In both cases, Cu is the B cation and O is the X anion, as shown in Figure 2-4.

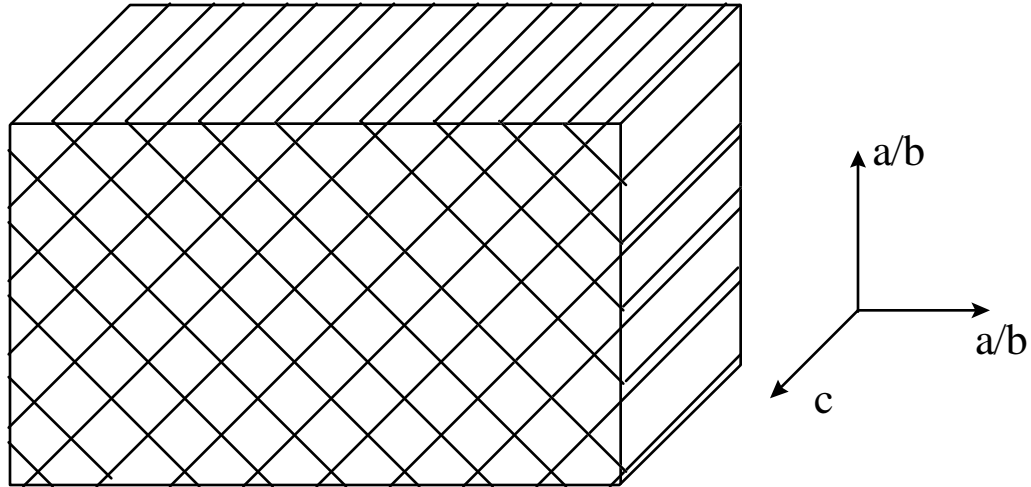


Figure 2-3) Schematic diagram of twin trace pattern. A 90° cross pattern generally indicates viewing plane normal to c axis, parallel twins indicate viewing planes parallel to c-axis.

The 123 structure consists of two Cu-O chains in the ab plane, sandwiching the BaO, Y and kinked CuO₂ planes, (**Figure 2-4**). Current conduction is anisotropic, flowing primarily along the CuO₂ planes (ab planes) rather than along the c axis. The anisotropy of normal state conductivity is 50-100 at 100K[52], and the anisotropy of magnetization $J_c \sim 20$ at 4K[53]. Oxygen concentration controls the key 123 phase properties: it determines whether the sample is tetragonal and insulating, or if the sample is orthorhombic and superconducting. **Figure 2-5** shows the effect of the oxygen concentration between O₆ and O₇ on the T_c[54](these oxygen vacancies are most likely to occur on the O1 and O5 sites in **Figure 2-4**). More recently, it has been shown that the peak T_c actually occurs at x=0.94. Above x=0.94, the compound is overdoped and the T_c decreases to 87.6K for x=1[55]. Unlike the BSCCO compounds, which have a Cu-O plane separation along the c axis larger than the ξ_{0c} , in YBCO the distance between the planes is slightly less than ξ_{0c}

and so the c-direction is not weakly-coupled. This fact explains why twist or tilt misorientation components have minimal effect on the coupling in YBCO[14,33] but are critical in BSCCO[56].

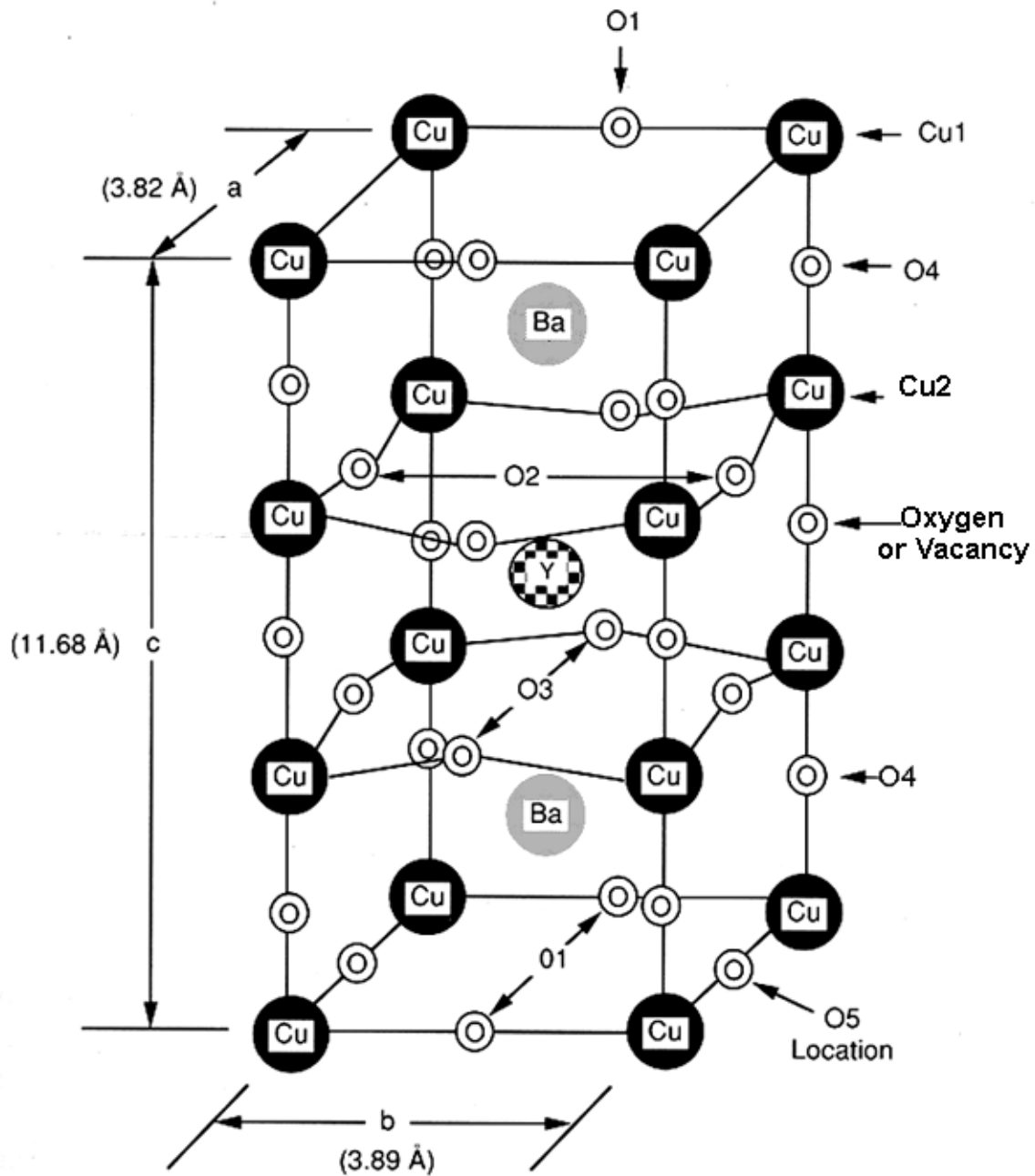


Figure 2-4) Drawing of the YBCO unit cell, orthorhombic and fully oxygenated to O_7 . The CuO_2 planes are kinked. Vacancies for $O < 7$ occur mainly at the O1 and O5 locations, with some on O4 as well[57]. Drawing from ref. [48].

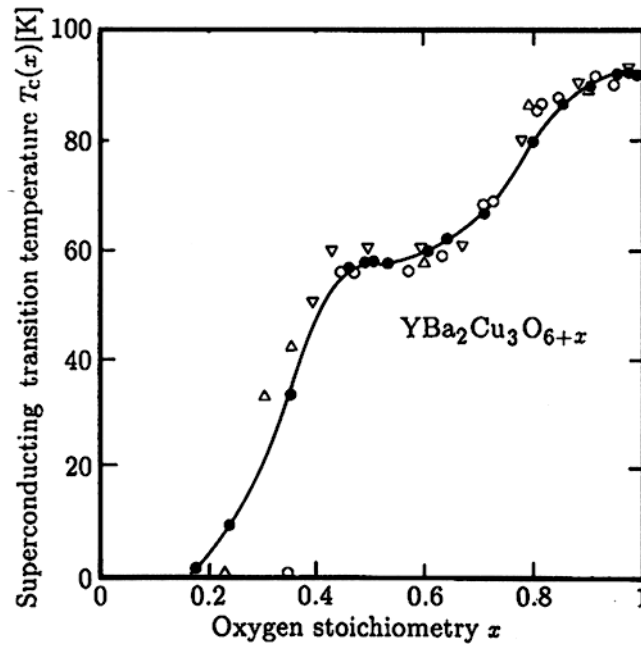


Figure 2-5) Graph of the T_c of $\text{YBa}_2\text{Cu}_3\text{O}_{6+x}$ as a function of oxygen stoichiometry (x). Solid points are calculation, open points are experimental data[58,59]. From Poulsen et al.[54].

The $\text{YBa}_2\text{Cu}_3\text{O}_{6+x}$ phase is one of several rare-earth (RE) variants of the “123” phase. The rare earth (“RE”) compounds containing La, Nd, Sm, Eu, Gd, Dy, Ho, Er, Tm, Yb, and Lu are all superconducting[60], with similar T_c and H_{c2} values, while the Pr-compound is insulating and Ce does not form the phase. The RE=Y compound has been the most widely studied because it is the most readily available and cheapest of the rare earths. It is also important to note that each rare earth 123 compound has a slightly different phase diagram, with different melting temperatures, etc. In fact, for Nd-123 and Sm-123, Nd/Sm forms a solid solution with Ba, which recently has led to the discovery of enhanced flux pinning in melt-textured Nd-123 and Sm-123[61].

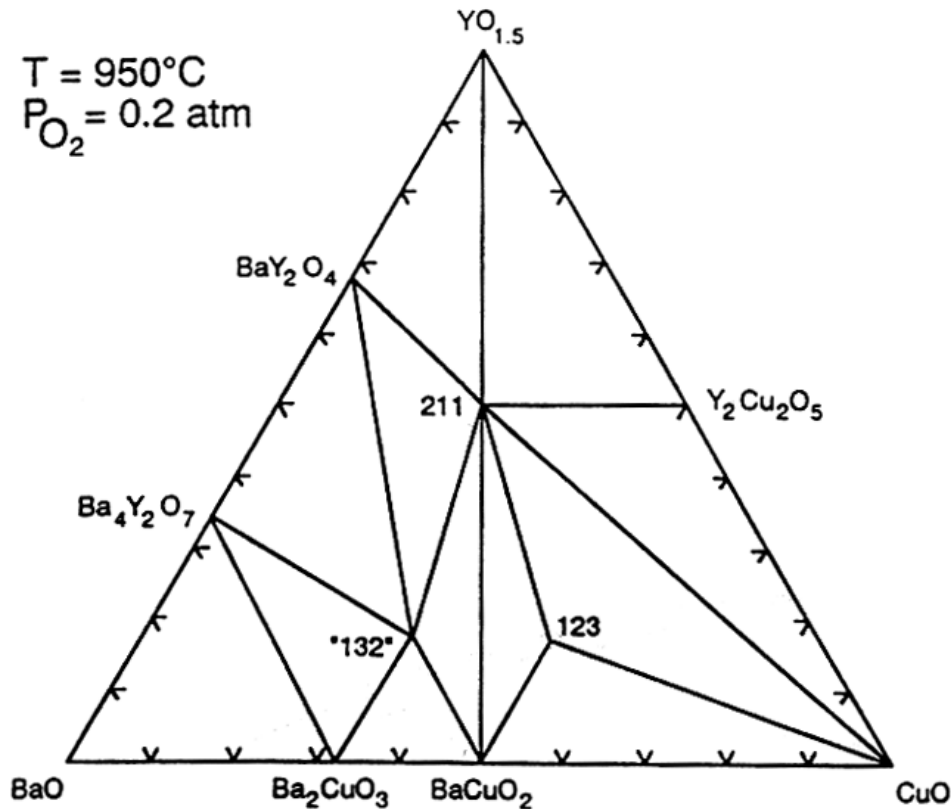


Figure 2-6) The $\text{YO}_{1.5}$ -BaO-CuO pseudoternary phase diagram at 950°C in air. The tie lines indicate that the 123 phase is stable with the 211, CuO, and BaCuO₂ phases at 950°C . These are the common impurity phases detected when trying to form 123. Phase diagram from Beyers and Ahn[62].

A pseudo-ternary phase diagram is needed to describe the complex four component Y-Ba-Cu-O system. On each of the vertices of such a phase diagram lie the three cation oxides: YO, BaO, and CuO, and each triangular cut represents an isotherm. **Figure 2-6** shows a 950°C cut in air of the pseudo-ternary phase diagram for the Y-Ba-Cu-O system. The tie lines show the phases that coexist during the formation of 123 from a stoichiometric

mix of oxide powders in the proper cation ratio; Y_2BaCuO_5 (“211”), CuO , and BaCuO_2 . These insulating second phases can be found in varying amounts in the final sintered material depending on the accuracy of the mix of powders and the time allowed for phase reaction. Grain size can range from $1\mu\text{m}$ up to $\sim 100\mu\text{m}$ in samples when grain growth is encouraged[63,64].

Single crystals were desired for studies of the intrinsic intragranular properties of YBCO. The primary crystallization phase field, the region of the pseudoternary diagram from which phase-pure single crystalline YBCO will result, is quite small, and is not directly above the stoichiometric 123 composition. This region was found at about the same time by many authors, and is shown by the shaded region in **Figure 2-7**[65]. Small crystals, typically in the tens or hundreds of microns in dimension can be formed by cooling slowly from these Ba- and Cu-rich melts. The procedure by which the pure flux-grown (FG) bicrystals were made for the initial UW bicrystal experiments involved crystallization from such melts using a Au crucible. The process yields less than 1% of YBCO crystals with dimension on the order of $0.5\text{mm} \times 0.5\text{mm} \times 0.2\text{mm}$ [66]. Despite the small sample size, complete oxygenation times require many hundreds of hours as single crystals are fully dense. The main oxygenation path is along the ab plane, as the oxygen diffusion coefficient is 4 to 6 *orders* of magnitude slower along the c axis[57]. Crystals with dimensions in the ab direction of larger than a few mm will take exceedingly long (\gg weeks) to fully oxygenate.

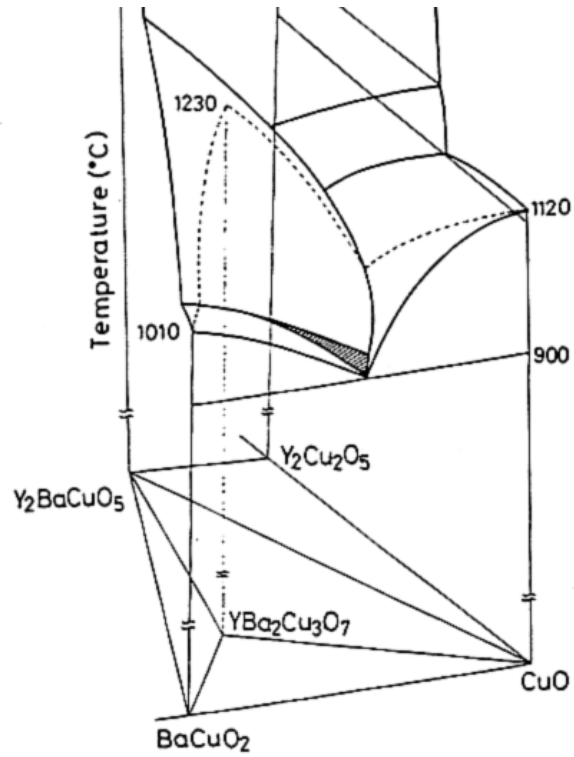


Figure 2-7) Space model of the YBCO phase diagram with the primary crystallization field for 123 shaded. Note that this field is quite small and is Ba- and Cu- rich with respect to the 123 composition. Phase diagram from Maeda et al.[65].

Melt-Texturing of $\text{YBa}_2\text{Cu}_3\text{O}_{6+x}$

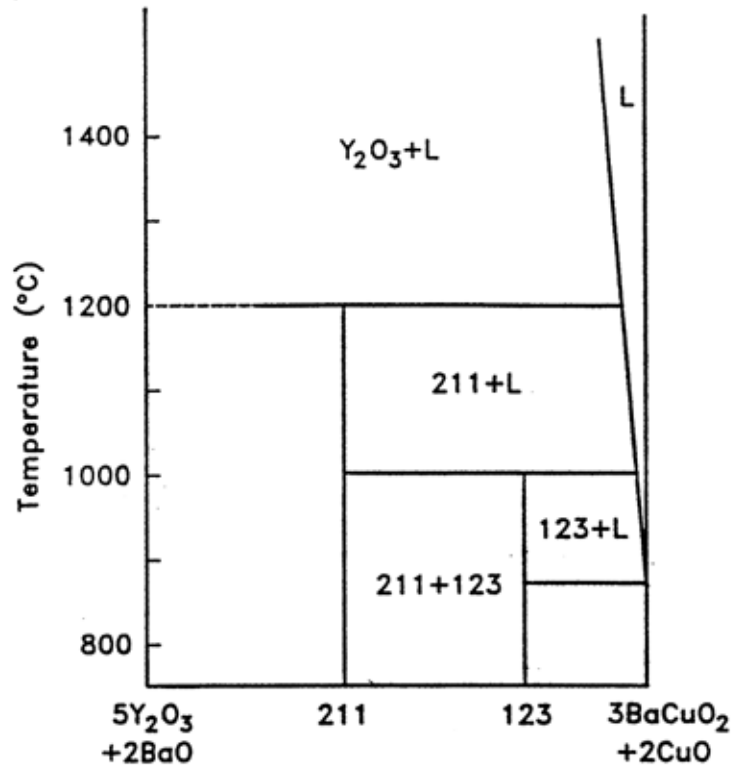


Figure 2-8) Vertical binary slice of YBCO pseudoternary in air (Figure 2-6). Phase diagram from Murakami et al.[67]

From a vertical slice of the YBCO pseudoternary phase diagram (**Figure 2-8**), we see that the melting of $\text{YBa}_2\text{Cu}_3\text{O}_{6+x}$ (123) at the 1000°C peritectic results in a liquid with solid Y_2BaCuO_5 (211), and then at 1200°C results in a liquid with solid Y_2O_3 . However, it is impossible to cool directly from a 123-composition liquid to phase pure 123; the kinetics

of the peritectic reaction are such that the reaction to 123 is never fully complete, and this results always in some amount of 211. The schematic **Figure 2-9** illustrates the formation of 123 during the peritectic reaction. As the Ba- and Cu-rich liquid combines with the 211 to form the solid 123 phase, the 123 phase becomes thicker and thus an increasing barrier to the completion of the reaction. This process of cooling a stoichiometric, or near stoichiometric (because of the added 211 phase), 123 liquid composition is known as melt-texturing and was first developed by Jin et al.[44]. The 123 was rapidly melted above the peritectic in oxygen and directionally solidified by slow cooling through a temperature gradient of 50°C/cm to 900°C, with a slow cool (10°C/hr) to facilitate oxygen uptake. This melt textured material had large (~mm) oriented regions with randomly distributed 211 particles (~20%-40% volume, dimensions ~10µm-40µm) and transport J_c in the 10^3 - 10^4 A/cm² at 77K with weak field dependence. The typical melt-textured microstructure is shown in **Figure 2-10**. Initially, the microstructure was thought to consist of thin (~10µm) aligned platelets, as features mistaken for grain boundaries were observed (**Figure 2-11**)[68]. These were later shown to be cracks containing CuO second phase. Such cracks are not continuous across the specimen, thus allowing convoluted but uninterrupted current paths through the c-axis of the sample (**Figure 2-12**)[69]. Thus large 123 grains (containing substantial 211 particles) are formed; these are not stacks of thin aligned platelets. Quenching experiments before and after oxygenation have suggested that these cracks form during the oxygenation step, most probably as a result of the tetragonal to orthorhombic transition[70,71].

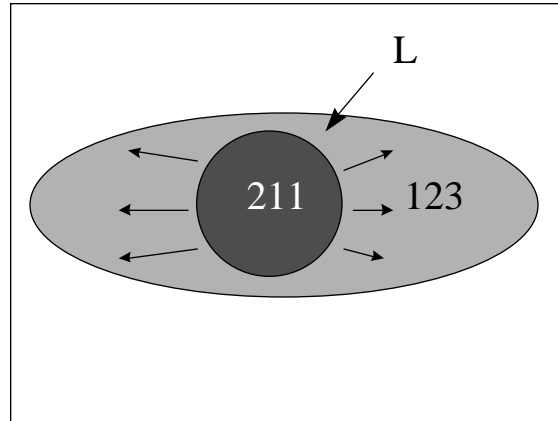


Figure 2-9) Schematic diagram of 123 grain nucleation and growth. Note that the growth of 123 shell around the 211 hinders completion of the peritectic reaction. Diffusion and growth is much faster in the ab plane than in the c-direction.

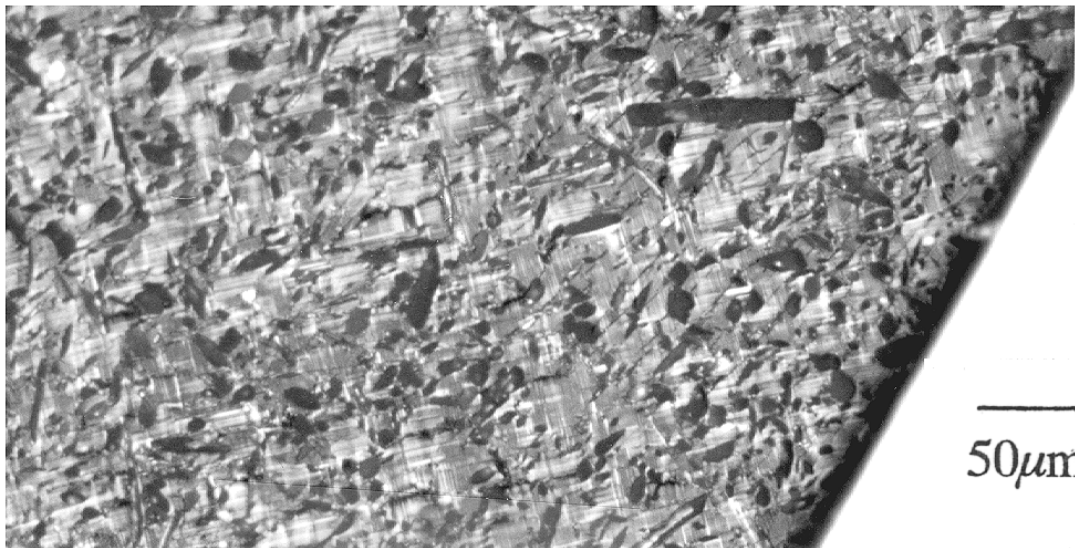


Figure 2-10) Typical microstructure of a melt-textured YBCO grain, viewed under polarized light. The primary twinned phase is 123. Because the twin traces are $\sim 90^\circ$ from each other, this indicates that the c-axis is approximately normal to the sample surface. The darker, elliptical second phase, with around 30% of the volume, is 211.

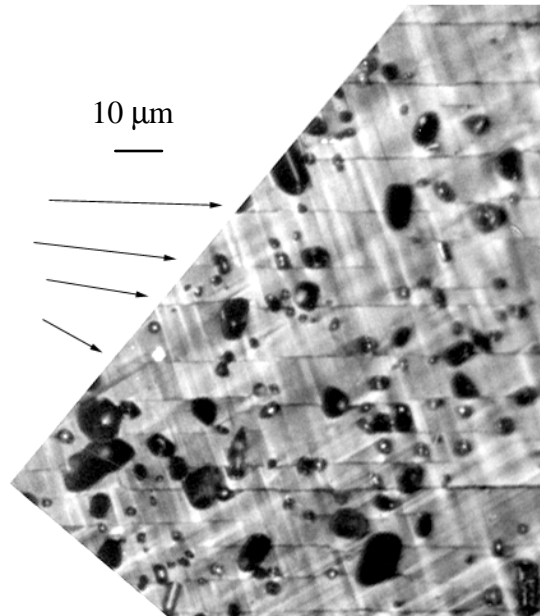


Figure 2-11) Cracks (or gaps), originally thought to be platelet twist boundaries, are indicated by the arrows. The twin trace pattern (the smaller angle between the twins is less than 90° but greater than 0°) indicates the c-axis of the sample is inclined from the sample surface (see Figure 2-3) and hence the cracks in the ab-plane are visible.

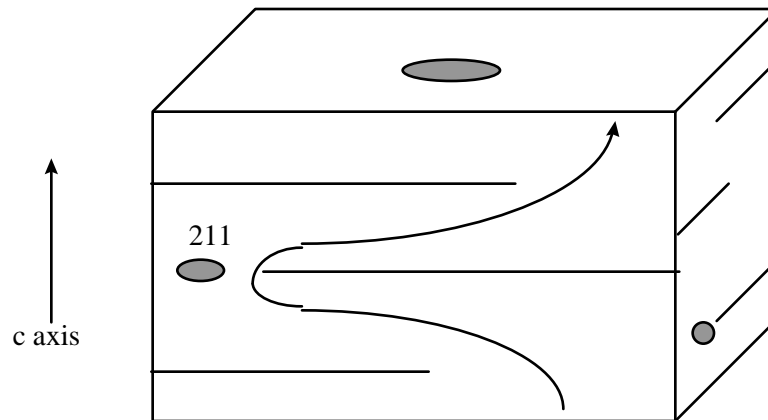


Figure 2-12) A drawing illustrating that the lines in the ab direction of melt-textured 123 are not grain boundaries but gaps as a result of the growth process filled with second phase, such as CuO,[69] or cracks due to the tetragonal to orthorhombic transition[70,71]. They do not extended across the width of the sample, and so current can flow along the c-axis of the specimen without crossing a grain boundary. Drawing adapted from Alexander et al.[69].

The effect of the ~30% volume of 211 particles found in conventional melt-textured (“MT”) material has been the subject of much debate and study. Most controversial has been the effect of 211 on flux pinning. As the J_c values of MT crystals are typically an order of magnitude higher than those found in pure single crystals, despite their lower fractional volume of superconductor, a direct enhancement of pinning by the 211 was proposed[72]. But for a second phase to exert its maximum pinning effect, it needs to be on the order of the coherence length, and the 211 grains are on the order of 10 μ m, four orders of magnitude too large. Studies on the effect of adding 211 to the 123 starting material, which enhances the volume % of 211 in the final matrix, were undertaken to establish the effect of 211 on flux pinning and critical currents. As a whole these experiments are inconclusive, as some groups report increases in J_c [73], some decreases[74] and some no effect[75,76]. More recently it was proposed that it is the 211/123 interface, and its assorted stacking faults and dislocations that are pinning the flux[77]. The amount and size of 211 also has been shown to have an effect on the twin spacing[78]. Decreasing the size of the 211 appears to decrease the twin spacing to dimensions necessary to appreciably influence pinning[79]. A TEM study of samples made with a variant of the melt-texture processes, has shown that there are numerous ~100Å size 211 precipitates, as well as the more commonly seen micron-size scale 211 particles[80,81].

Various modifications and improvements to the melt-texture process have developed in the past 7 years. It was originally a batch process, performed with a

stationary sample and hot zone. In an attempt to make melt-texturing a continuous process, various techniques by which the sample is drawn slowly through the furnace hot zone were tried[82]. While the procedures were successful to various extents, both the extremely slow speed of the process (<1mm)[81] and the tendency for new grains to nucleate remain impediments for large scale conductor applications.

Some modifications to the melt-texture process have been designed to increase pinning so as to make YBCO a suitable material for levitation applications (especially flywheels). These are likely to be the first applications of bulk YBCO, as the ability to trap significant flux at 77K (up to 3.1T with proton irradiation[83]) is unique among the high temperature superconductors. For this application, samples are designed to be single crystals, and so intergranular coupling is not an issue. An early successful attempt to increase the pinning was through the quench melt growth (“QMG”) technique[84]. In this technique, 123 is heated into the Y_2O_3+L region (**Figure 2-8**) and then quenched to retain small Y_2O_3 particles. When subsequently melt-textured, a finer dispersion of 211 particles results. This in turn leads to a more complete $211+L \rightarrow 123$ reaction and enhanced flux pinning. Pt additions (0.5wt%) further refine the 211 particles to $<1\mu m$ [85,86], also producing a more complete peritectic reaction. Additives, including $BaSnO_3$ and $BaTiO_3$, can modestly increase flux pinning [87,88,89]. A more recent pinning enhancement technique involves melt-texturing the Nd-123 compound. This material has a solid solution between Nd and Ba (site interchange between Nd and Ba is possible), and in earlier experiments this interchange reduced T_c . Murakami et al.[61] demonstrated that if the melt-texturing occurs in a reduced oxygen atmosphere (1% O_2 /99%Ar), the substitution is

minimized and material with $T_c \sim 95\text{K}$ can be formed, after subsequent oxygenation. In fact, the slight cation site interchange that does occur seems to enhance pinning at about 1T and this substitution enhances H^* , with $H_c^* \sim 8\text{T}$ [90], about 3T higher than for melt-textured Y-123.

In an attempt to create larger grains for levitator applications, a single crystal seeding technique has been developed[91]. A Sm-123 (or other RE-123 compound with a higher melting point than Y-123) seed is placed on a large Y-123 puck before melt texturing. This nucleates the 123 phase grain growth on melting the puck. The process can result in large single domain samples (up to $\sim 3\text{cm}$ in dia.[92]) with large levitation forces at 77K. An interesting side note on this procedure: if there are two seeds on a puck and the seeds are misaligned, the single crystal growth fronts will impinge, creating a controlled misorientation bicrystal[93,94].

Interest in minimizing possible impurities from the grain boundaries in melt-textured YBCO led to the development of the melt-out melt texture process[95]. It has long been known that trace amounts of certain impurities, like carbon, can significantly degraded intergranular properties in sintered and melt-textured YBCO[96,97]. In melt-textured YBCO, possible boundary contaminants include those that have been found in sintered material (C, Cl, Mo, Zr, Sr, etc.)[98], as well as the second phases left over from the incomplete peritectic reaction (BaCuO_2 , CuO). The melt-out procedure involves melt-texturing on a 211 substrate block (**Figure 2-13**). This 211 block is believed to wick out impurities - as much as 40% of the original sample volume is absorbed into the block. Parikh et al. [32] claimed strongly-coupled behavior out to 28° of misorientation for these

melt-out samples. While their misorientation and electromagnetic characterizations were not persuasive, it was the idea of clean bulk-scale grain boundaries that would lead to these samples being chosen for the experiments of the later part of this thesis.

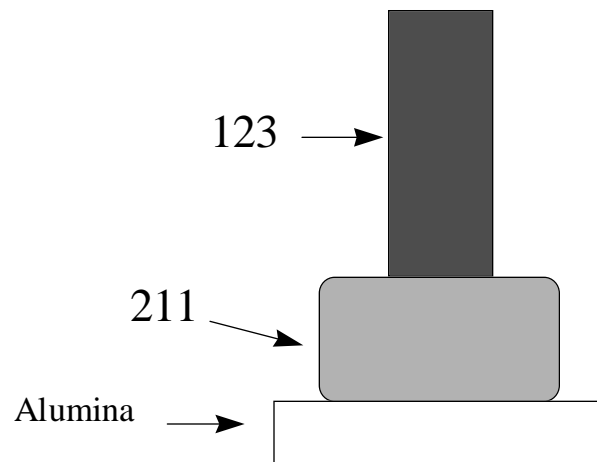


Figure 2-13) A simple drawing of the melt-out, melt-texturing process before texturing begins. The sintered 123 bar is melt-textured on a 211 bar. During melt-texturing some 30-40% of the liquid, including possible impurities, is wicked into the porous, low density 211 block. Drawing adapted from Willen and Salama[95].

Determining the Coupling Characteristics of the Grain Boundary

In describing the electromagnetic properties of grain boundaries, terms like “weak link” and “weakly coupled” are often incorrectly used interchangeably. Strictly speaking, a “weak-link” grain boundary indicates only that the grain boundary J_c is less than that of the grains. With this definition, a grain boundary that provides even the slightest degradation of current flow is a weak link, even if the degradation is due to an experimental artifact, e.g., a crack along a portion of the boundary. If a grain boundary transmits 90% of the grain’s critical current even at high magnetic fields, it still is technically a weak-link despite being a grain boundary that would not impede high current applications. The terms “weakly-coupled” or “strongly-coupled” are more appropriate and illustrative, as they give qualitative assessments from a standpoint of practical applications, and are defined below.

A strongly coupled boundary may be described as having an intergranular $J_c(B)$ that is similar to the intragranular $J_c(B)$. For T not near T_c and H not near H^* (the case of YBCO at 77K), this will mean that the intergranular J_c is not degraded by the application of small magnetic fields (**Figure 2-14**). At high magnetic fields, the intergranular $J_c(B)$ exhibits flux pinning, single crystal like characteristics, including flux-flow dissipation in the V-I trace (**Figure 2-15**). The flux pinning behavior can have an exponential relationship to magnetic field[99], such as $J_c(B,T)=\alpha(T)\exp[-\mu_0 H/\beta(T)]$ where $\alpha(T)$ and

$\beta(T)$ are temperature dependent fitting parameters, as this relationship has been shown to apply for epitaxial YBCO thin films[100]. It is the lack of sensitivity of the J_c to magnetic field that is considered the hallmark of strongly-coupled behavior, not the absolute value of the J_c . A UW 14° boundary was considered strongly-coupled despite having a zero field J_c of $<10^3 \text{ A/cm}^2$ [4]. It was the demonstration that this critical current was not diminished by low applied magnetic fields that supports the strongly-coupled description. There are a number of extrinsic factors (e.g. cracks, low/non-optimized intragranular flux pinning) that would contribute to low transport J_c without conveying information about the intrinsic nature of the order parameter at the grain boundary.

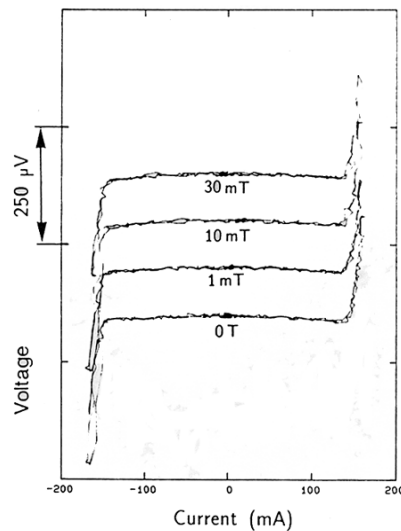


Figure 2-14) Typical V-I traces for a strongly-coupled 90° grain boundary. The key feature is that low applied magnetic fields do not diminish the I_c . Plot taken from Babcock et al.[4]

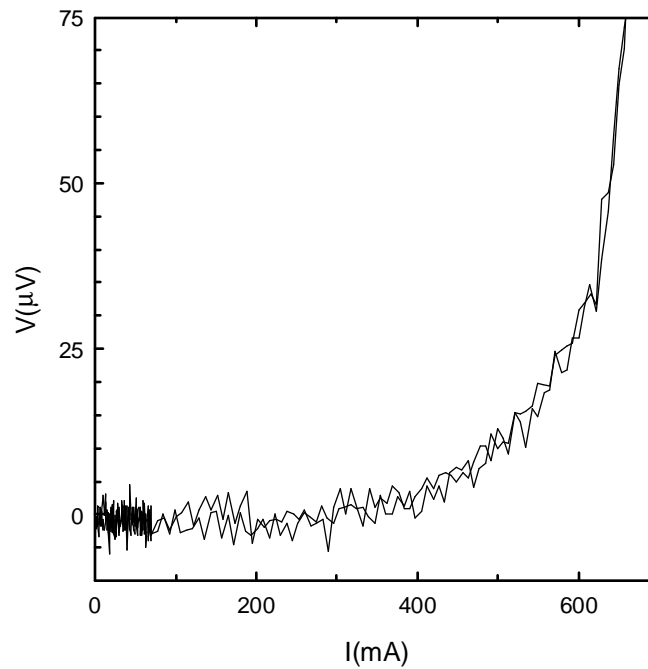


Figure 2-15) Plot of the smooth flux-flow V-I characteristic of a strongly-coupled melt-textured 5° grain boundary at 0.4T and 77K.

A weakly coupled grain boundary can be defined as having intergranular electromagnetic properties that are strongly depressed by the application of small magnetic fields (on the order of Gauss or tens of Gauss), and having a resistive transition with ohmic character above I_c (**Figure 2-16**). From this resistive transition the grain boundary resistivity (ρ_{nd} , a normal state parameter used to quantify the quality of a junction[101]) can be determined ($\rho_{nd} = R_n A$, where R_n is the ohmic resistance and A is the boundary cross-section). The $J_c(B)$ sensitivity indicates that the GB is acting as a Josephson junction (JJ) and thus has a qualitatively and quantitatively distinct $J_c(B)$ behavior from that of the

grains (**Figure 2-14, Figure 2-15**). The JJ behavior may be complex: it may be a tunnel junction, where the barrier is insulating (SIS), a proximity coupled junction, where the barrier is a normal metal (SNS), or a weak superconductor junction, where the barrier is a superconductor of depressed T_c (SS'S). Modeling my weakly-coupled bicrystals to a SIS, SNS, or SS'S model was not pursued as a focus of this thesis.

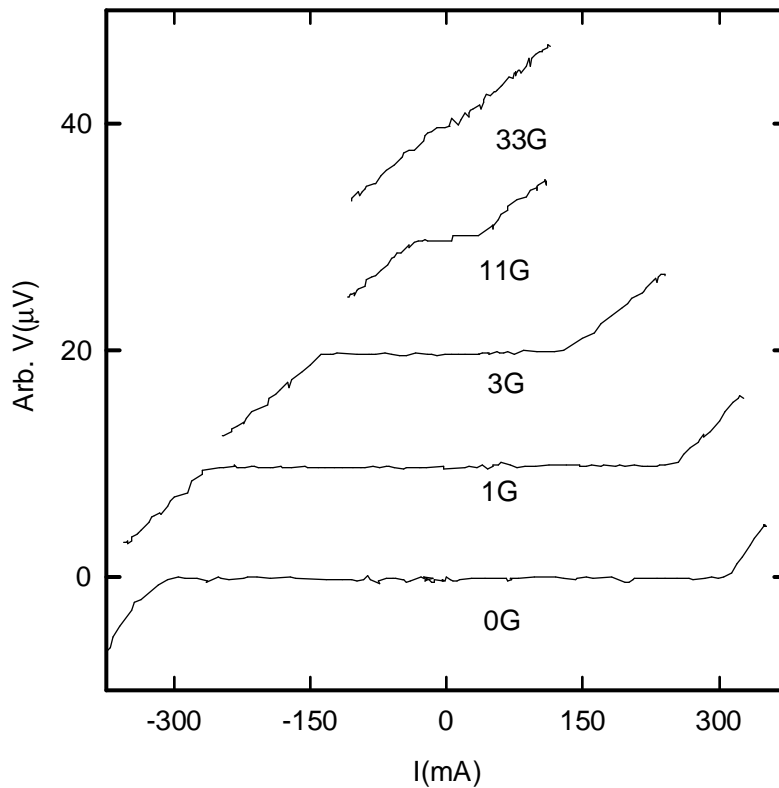


Figure 2-16) Plot of V-I curves of UW melt-textured high angle ($55^\circ [2 \ 3 \ 1]$) bicrystal MB4C1. Low magnetic fields greatly decrease the supercurrent from the zero field value, and the resistive transition is ohmic.

The behavior of Josephson junctions in high magnetic fields had not been extensively studied, as low T_c junctions were not designed for high field current transport. Still, Owen and Scalapino[102] showed theoretically (later confirmed experimentally[103]) that for a large ($L > 10\lambda_J$; L is the width of the junction bridge, λ_J is the Josephson penetration depth) one-dimensional JJ, the traditional short JJ Fraunhofer pattern has overlapping secondary maxima. This results in a $J_c(B)$ envelope with the smoothness of the envelope depending on the size of the junction. Yanson[23] has also shown in Sn-Sn JJ that inhomogeneities along the junction will also result in a similar residual current behavior. More recently Bulaevskii et al. developed the “brick wall” model for current transport in the Bi-oxides[24] based on the Yanson work[23]. The central feature of this model was that the current transport in tapes was limited by a Josephson current through the c-axis twist grain boundaries in high fields. Thus the high field residual current seen in high angle grain boundaries in high temperature superconductors is often asserted as being Josephson in nature.

Essential Structural Features of Grain Boundaries

As discussed in the **Chapter 1**, the width of grain boundaries in YBCO, approximately one coherence length, leads directly to a depressed superconducting order parameter and inherent potential for the grain boundary to be weakly coupled[8]. To understand the electromagnetic properties of grain boundaries in YBCO, it is important to review the key structural characteristics of grain boundaries. The grain boundary is the interface at which two crystals of different crystallographic orientation meet (**Figure 2-17**). Dislocations at the grain boundary accommodate the mismatch between the lattices. Due to the disorder at the interface, grain boundaries are regions of quick diffusion and impurity segregation, and may be weak physical links. I will now briefly introduce some basic grain boundary concepts relating to low angle grain boundaries and high angle grain boundaries.

For a low angle, symmetric tilt grain boundary, the dislocation spacing formula of Equation 2-1 can be obtained from the geometry of **Figure 2-17**. The dislocation spacing is D , the misorientation angle is θ , and the Burgers vector is b . The Burgers vector can be determined via TEM, and in **Figure 2-18** we see the dislocation spacing vs. misorientation angle plot for a simple [001] tilt boundary using experimentally found Burgers vectors[104]. Noting that the coherence length in the ab plane in YBCO is $\sim 1.5\text{nm}$, the spacing may be predicted to pinch off strongly coupled supercurrent channels at $\sim 10^\circ\text{-}15^\circ$, even without taking into account the finite size of the dislocation cores. While symmetric

tilt about a low index rotation axis is not the geometry of my samples, it is the claimed geometry of the original thin film bicrystal experiment[13] to which my results will be contrasted.

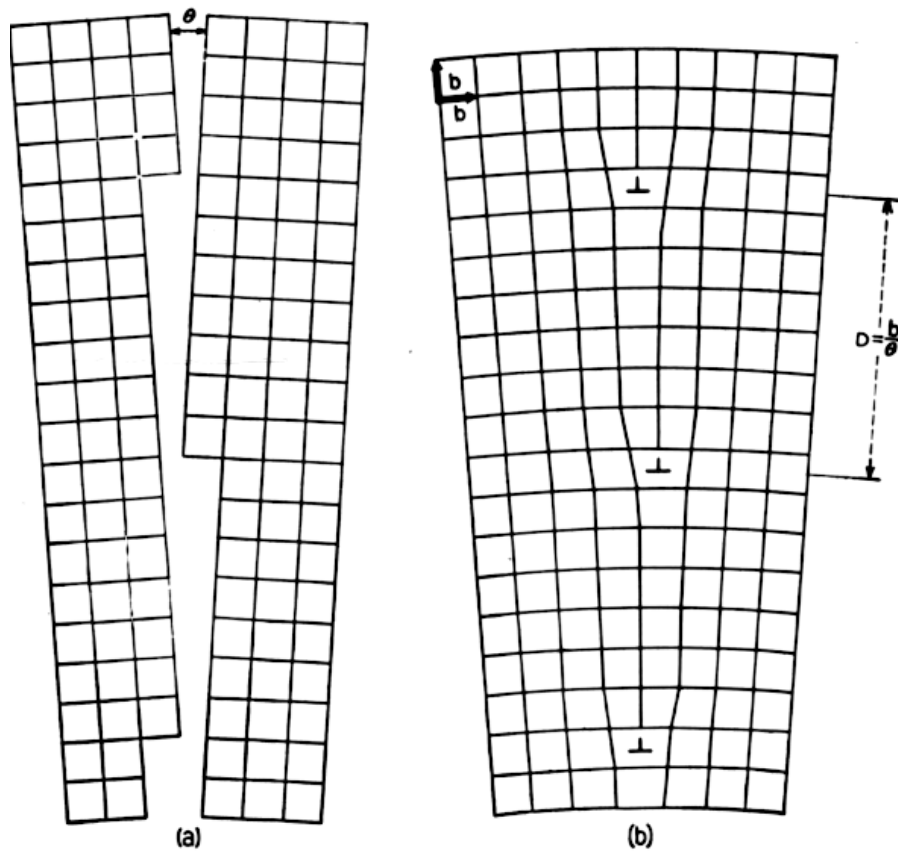


Figure 2-17) a) Two cubic crystals are misoriented by θ about [001]. b) When the crystals are joined, the mismatch can be accommodated by elastic strain and edge dislocations (\perp) spaced b/θ , where b is the burgers vector. Drawing from Read[105].

Equation 2-1

$$D = \frac{|b|}{2 \sin\left(\frac{\theta}{2}\right)} \approx \frac{b}{\theta} \text{ (for small } \theta \text{)}$$

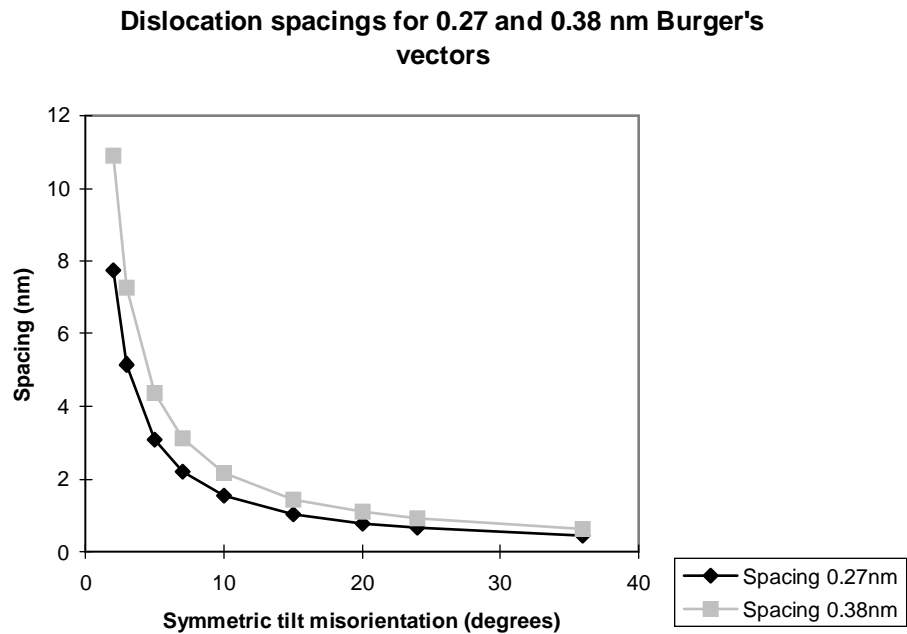


Figure 2-18) Plot of dislocation spacing in a [001] tilt grain boundary as a function of misorientation angle for two different burgers vectors observed by I-Fei Tsu[104]. Plot from Tsu[104].

When considering general misorientation low angle grain boundaries, the GB disorder is far more complex and Frank's formula (Equation 2-1) is needed to describe the dislocation spacing. In Frank's formula, \mathbf{V} is a vector chosen that lies in the boundary plane (and will hold for all such vectors), \mathbf{u} is the rotation axis, \mathbf{b}_i is a Burgers vector of type "i", and $\mathbf{N}_i = (\mathbf{n} \times \xi_i) / (2D_i \sin(\theta/2))$, where \mathbf{n} is the grain boundary normal, ξ_i is the

tangent vector to the dislocation type “i” and D_i is the dislocation spacing[105]. Determining the dislocation spacing via Frank’s Formula for each of the sets of dislocations of general misorientation grain boundaries is non-trivial. The minimum number of sets of dislocations (3) in a general misorientation grain boundary would result in 6 independent equations, of which hard to find experimental parameters are needed. Therefore, accurately describing dislocation spacings for each of my general misorientation grain boundaries was not pursued as the focus of this thesis. It is noted that for the same degree of misorientation, the maximum dislocation spacing in a general misorientation grain boundary (with 3 sets of dislocations) should be no larger than the dislocation spacing of a simple tilt boundary (with one set of dislocations). In other words, general misorientation GBs should have less superconducting channel area than the simple tilt counterpart at the same misorientation.

Equation 2-1

$$\mathbf{V} \times \mathbf{u} = \sum \mathbf{b}_i (\mathbf{N}_i \bullet \mathbf{V})$$

For high angle boundaries ($\theta \sim > 15^\circ$) (either simple tilt misorientation or for general misorientation), the dislocation cores begin to overlap and it becomes increasingly difficult to describe the grain boundary as being comprised of discrete dislocations. Regions of atomic matching at the interface can still be found by considering a Coincidence Site Lattice (CSL) model[106]. In the CSL model, special low coincidence grain boundaries are shown to arrive by periodic matching of atomic structure of the two grains that

compromise the bicrystal (**Figure 2-19**). These boundaries are called low Σ boundaries, where the Σ corresponds to the inverse of the volume density of coincident lattice points. If one overlays the crystal structure of one grain on the other past the grain boundary plane, certain lattice points from each crystal may overlap or coincide in a repetitive cell-like pattern. The number of lattice points in a cell is the Σ value, and so increasing coincidence is reflected in lower Σ values. **Figure 2-20** illustrates that grain boundary energy can have a non-monotonic relationship to misorientation angle. The preferential formation of bicrystals at low Σ misorientations is evidence of special grain boundary properties in YBCO[107]. The actual density of these coincident points at the grain boundary will depend on the placement of the grain boundary plane; hence faceting would be expected to play a role as to the actual content of atomically matched material across the boundary interface. Variations of the CSL are perhaps more directly appropriate for YBCO, as the CSL is intended for cubic systems or other systems as long as the squares of the lattice parameter ratios ($a^2:b^2:c^2$) is rational[108]. The YBCO system can be approximated as a stack of 3 cubic units; still it is unclear whether the CSL approach is appropriate[109]. The Constrained Coincidence Site Lattice model allows the unit cells to expand or contract their axial ratios so as to become a CSL boundary[110]. In YBCO, this would mean the adjustment of the c-axis length and hence the oxygen concentration. Therefore, the region near a high angle, CCSL YBCO boundary may give up oxygen so as to be a lower energy boundary[111]. Regardless of the model used, there is reason to believe that high angle boundaries can have regions of atomic matching across the interface if a boundary facet intercepts a low Σ facet. Note that this is the matching of singular

lattice points, not entire unit cells, and this effect of partial matching of a unit cell across an interface on superconducting properties has not been established.

A more detailed description of the crystallography of general misorientation bicrystals, as well as the definitions of tilt and twist grain boundaries can be found in Appendix A.

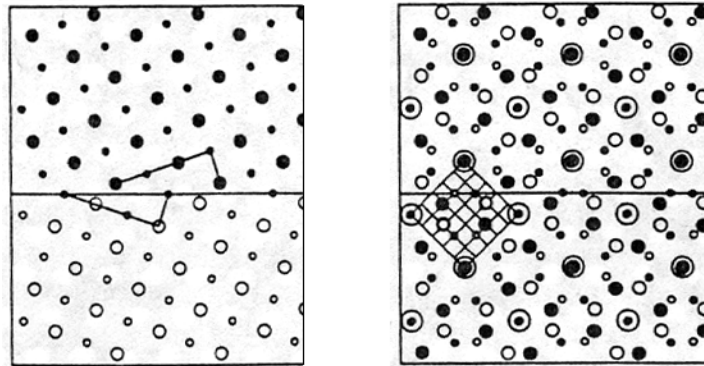


Figure 2-19) The graphical definition of Σ . The left image shows the atomic positions that comprise the two crystal lattices of the grains of a bicrystal. The right image shows the overlap the atoms from one grain of a bicrystal onto the other grain, and a pattern of coincident points that may appear. The number of atoms that comprise each coincident cell is the Σ value, the lower the number indicating the higher the coincidence. Figure from Merkle[112].

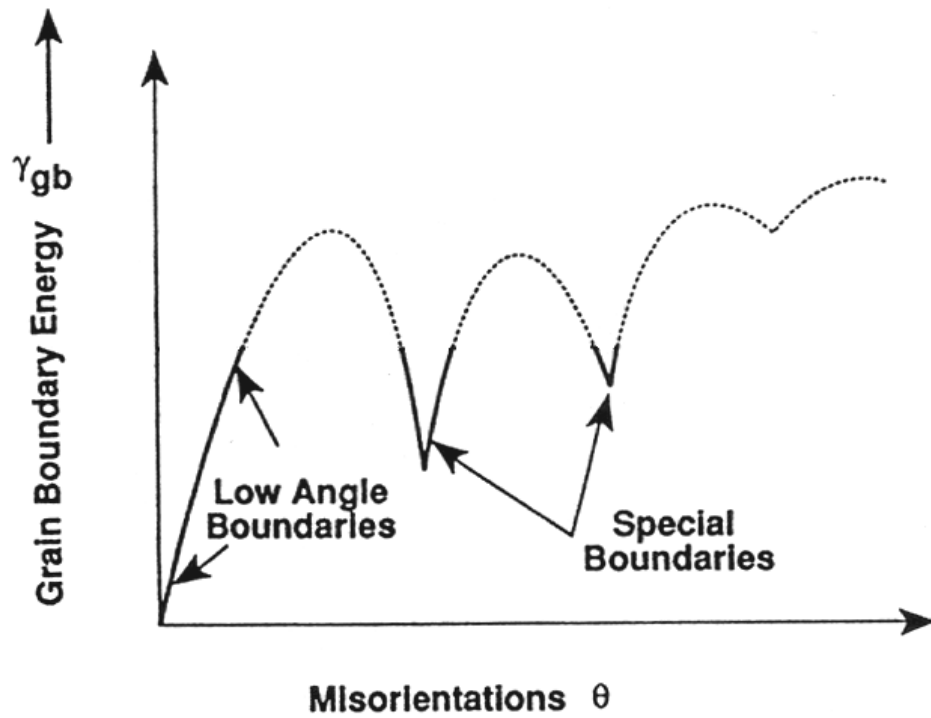


Figure 2-20) Schematic plot of grain boundary energy vs. misorientation angle. At certain higher angle misorientations there exists special low energy grain boundaries. Plot adapted from Chan[113].

Chapter 3 : Initial Melt-Textured $\text{YBa}_2\text{Cu}_3\text{O}_{6+x}$ Bicrystal Experiments

In this chapter I will present the experimental background, results, and discussions pertaining to the initial melt-textured experiments carried out from ~1990-1994. The results obtained from these studies provided the key motivation to the concluding experiments described in **Chapter 4**.

Sample Fabrication

Melt-textured samples from two sources were used in these melt-textured bicrystal experiments. The majority of these samples were made by myself at the University of Wisconsin-Madison and are identified by the prefix “MB”(bicrystal) or “MT” (in-line tricrystal). The rest of these samples were obtained from S. Jin at A.T.&T. Bell Labs, and are identified with the prefix “SJ3151B”.

The fabrication procedure for the samples made at the UW was derived from that of Salama et al.[5] (**Figure 3-1**). Samples of melt-textured YBCO were made with varying amounts of 211 additions (0-20 mole%), in part to investigate the effect of the added second phase on grain boundary properties. As mentioned in the introduction, 211 was thought to enhance pinning, but it also was claimed that the 211 particles attracted impurities away from the boundary[114]. To create melt-textured YBCO, it is desirable to first make single phase superconducting YBCO that is free of carbon[115] and other impurities. For our earliest samples, the starting YBCO material was made at the UW by

calcining the appropriate cation ratios (1:2:3) of Y_2O_3 , $BaCO_3$, and CuO powder. The appropriate gram weights for a ~20 gram batch were measured out on a Sartorius digital scale (± 0.0001 gram precision), in an argon-filled glove box to avoid moisture absorption by humid air. These powders were then removed from the glove box, mixed in a standard coffee grinder, and pressed at 10^4 PSI in into 1" dia. x 0.25" thick pellets. These fragile pellets were placed into alumina boats and calcined in a tube furnace at $880^\circ C$ for 24 hours with flowing air at 3 standard cubic feet per hour (SCFH). Trace amounts of CO_2 and H_2O were removed from the air by flowing through drierite and ascarite. The resultant pellets had a matte black appearance, with a hard and brittle texture. Although the calcining of YBCO was generally successful, pre-calcined YBCO from Allied Signal was eventually used as it was of good quality, readily available, and saved a time-consuming step.

After pressing, the pellets were sintered below the melting point for 48hr. at $880^\circ C$ with an air flow (through drierite and ascarite) of 3 SCFH. For samples with added 211 phase, the 211 powder was added in the appropriate mole% before pressing (mole% of 0%, 10%, and 20%). The 211 was created by mixing and pressing the appropriate cation ratios (2:1:1) of Y_2O_3 , $BaCO_3$, and CuO powders into pellets, and calcining at $920^\circ C$ for 48 hrs. in 1 SCFH of flowing air. This resulted in a light green ceramic with a chalk-like texture, which was then powdered in a coffee grinder before adding to the YBCO. No bicrystals of 0% were measured electromagnetically due to visibly large amounts of impurities at the grain boundaries. One UW 10% 211 ("MB4B1") and eight UW 20% 211 samples ("MB4Cx" and "MT4Cx") were successfully measured (see **Results, Table 3-1**).

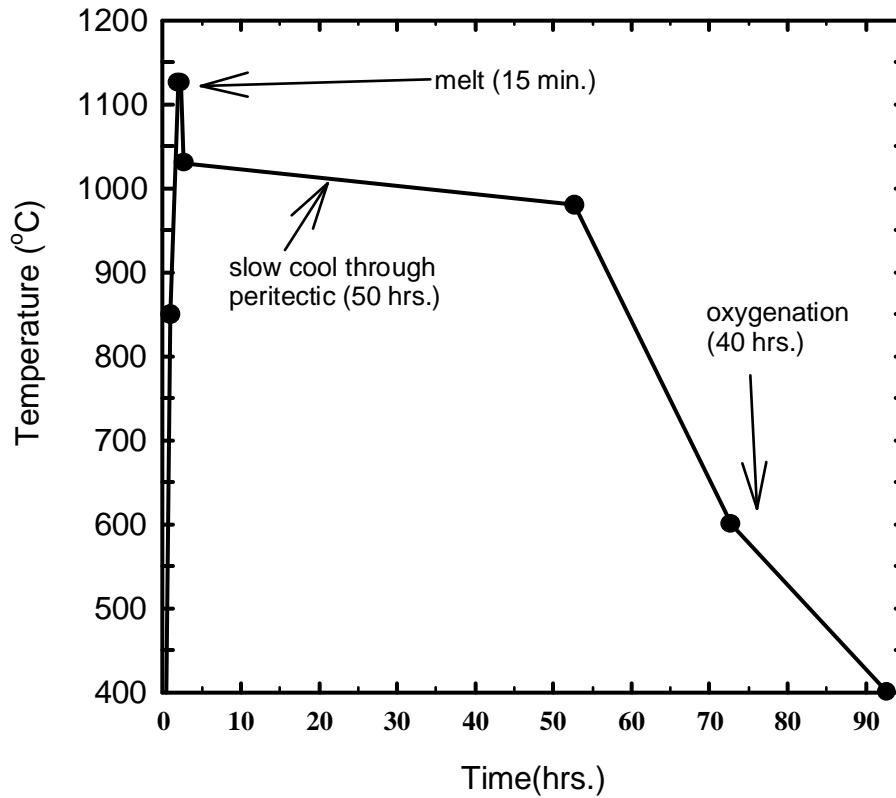


Figure 3-1) The melt-texture process: plot of temperature vs. time, based on the procedure developed by Salama et al.[5]. The quick initial heating creates a melt of 211+liquid. The key grain growth step is the 50 hrs. slow cool through the peritectic. Oxygenation occurs below 600°C.

After the YBCO pellets were sintered, they were cut in half with a diamond saw, and placed on an MgO powder buffer layer[116] in alumina boats for melt texturing. A buffer layer is desired because alumina reacts with the YBCO melt, contaminating the sample by forming the low T_c $\text{YBa}_2\text{Cu}_{3-y}\text{Al}_y\text{O}_{6+x}$ phase[117]. MgO does not readily react

with YBCO at high temperatures due to its high melting point. Melt-texturing was done in a quartz tube with 1atm. flowing O_2 in a microprocessor-controlled high temperature furnace (max. temp $\sim 1250^\circ C$). This was programmed as follows: 1hr. heat to $850^\circ C$, 1hr. heat to $1125^\circ C$, hold for 15 min. to create a L+211 melt, cool to $1030^\circ C$ in 30min., then slow from $1030^\circ C$ to $980^\circ C$ over 50hrs cool through the peritectic (**Figure 3-1, Figure 2-9**). This latter step is the key to large grain growth. After grain growth, the furnace is cooled from $980^\circ C$ to $600^\circ C$ in 20hrs. and $600^\circ C$ to $400^\circ C$ in 20hrs. During these last two steps the sample undergoes the tetragonal-orthorhombic transition and oxygen is taken up by the sample such that it approaches full oxygenation. The AT&T samples were manufactured by the melt-texture route of Jin et al.[44] and contained 20% added 211 phase.

Identification of the superconducting and secondary phases was achieved through a variety of methods. Observation of the appropriate powder x-ray peaks for the YBCO was the most formal, but the least convenient, as this required powdering the pellet. Peaks for YBCO and 211 were clear, but due to the limits of x-ray diffraction sensitivity, phases below $\sim 5\%$ could not be detected by this method. Metallographic analysis under polarized light was excellent for melt-textured samples, as the various phases are easily identifiable. As described in **Chapter 2**, the 123 phase is the majority phase and is visibly twinned. The 211 phase appears as slightly darker, untwinned, oval-like regions within the 123 crystals, totaling $\sim 20-40\%$ by volume, while $BaCuO_2$ and CuO appear as bright, small agglomerations in certain areas of the sample, sometimes at the grain boundaries (**Figure 3-2, Figure 3-3**). A simple, non-destructive technique to verify the presence of

the high T_c phase is to cool the sample down with liquid nitrogen to ascertain if it levitates above a permanent magnet. This technique can quickly demonstrate if a significant fraction of the material is superconducting, but it is not quantitative.

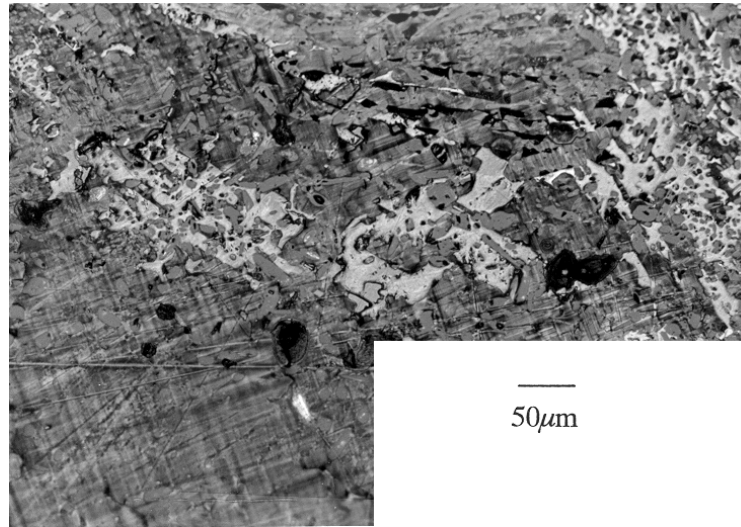


Figure 3-2) Polarized light micrograph of the amorphous non-superconducting and BaCuO₂ and CuO phases resulting from an incomplete peritectic reaction during resolidification from the melt (light gray in the image). The majority, matrix-phase is YBCO.

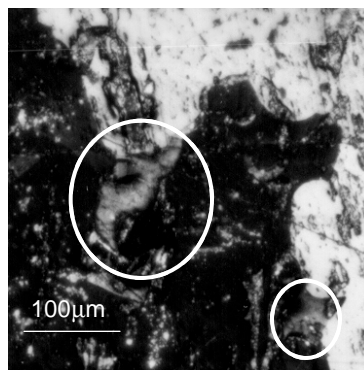


Figure 3-3) The circled regions of this polarized light micrograph highlight large, amorphous, non-superconducting phases at the grain boundary. Contamination at this size scale will clearly result in an insulating grain boundary.

Bicrystal Isolation

Bicrystals were extracted from the bulk melt-textured material in a multiple step process. First, longitudinal slices were cut across each textured half disk with a diamond saw lubricated by methanol or ethanol. These slices, initially ~0.5mm-1mm in thickness, were randomly fractured so that they would fit on a 1cm diameter aluminum polishing stub. The slices were affixed to the stub with Crystal Bond (a strong wax-like adhesive used in microscopy preparations) heated to ~100-200°C on a hot plate. This assembly was then fitted into a Gatan Disc Grinder, which allowed adjustments to the polishing surface plane with a precision on order of microns. It was important to mount the sample in this manner so that it was easily removable after polishing for subsequent electromagnetic experiments; mounting in a thermoset polymer puck (as is standard practice in polishing metallographic samples) would prevent extraction. The samples were ground with SiC grinding paper (220 grit and 600 grit) and then polished with 0.3 μ m alumina in methanol suspension on a Buehler nylon polishing cloth. Initially a 0.05 μ m alumina in methanol suspension final polish was used, but it was determined that the 0.3 μ m solution was adequate for resolving the finest structure of interest, the twin boundaries. Samples were ground and polished to a final thickness of ~50-100 μ m to assure that there was only one grain boundary through the thickness of the sample. Sample thickness was approximately measured by use of the calibrated focus depth of the

40X objective on a Olympus BHM microscope (1 knob unit $\sim 1\mu\text{m}$), and later more precisely determined with Mitituyo precision calipers after the sample was removed from the polishing stub. Samples were removed by re-melting the crystal bond and/or soaking in acetone, and methanol or ethanol was used to clean off the acetone. Grain structure was clearly visible (**Figure 3-4**) after the polishing step.

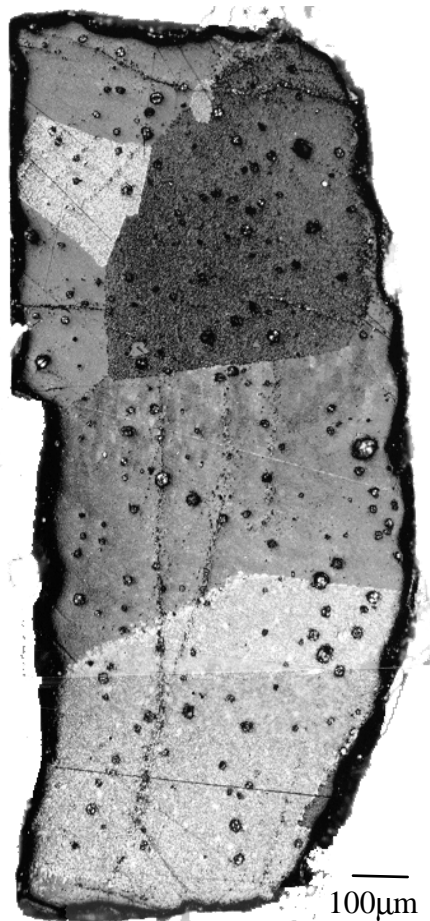


Figure 3-4) Polycrystalline melt textured sample from AT&T[44], thinned and polished, and viewed under polarized light. The different regions of contrast represent grains of different orientation. The very small dots are 211, and the larger circles are voids.

In the early experiments, the sample had to be sequentially fractured until a bicrystal of large enough size was obtained. The surface had to be large enough for the contacts (this required $\sim 150\mu\text{m} \times 150\mu\text{m}$), and ideally large enough for an x-ray pole figure ($\sim 250\mu\text{m} \times 250\mu\text{m}$). Both sides of the sample had to be polished and photographed to prove that sample had just one grain boundary (**Figure 3-5**). Another early method for bicrystal isolation was considerably more time-intensive but had the benefit of allowing more control as to which bicrystal was to be selected from the polycrystalline matrix. The method involved polishing and photographing the four long sides of a rectangular slice. It then could be decided which bicrystal to isolate by grinding and polishing from the opposite sides (**Figure 3-6**) of the desired boundary.

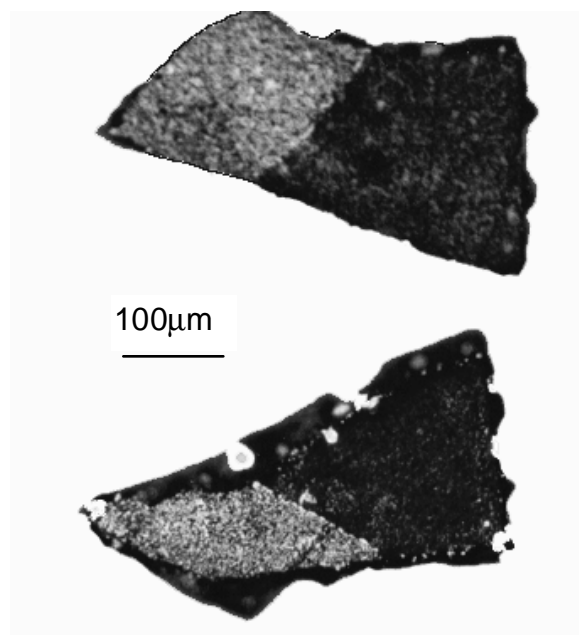


Figure 3-5) Polarized light micrograph of the top and bottom surfaces of sample SJ3151B3, which has been thinned to $50\mu\text{m}$. The boundary goes completely through the sample.

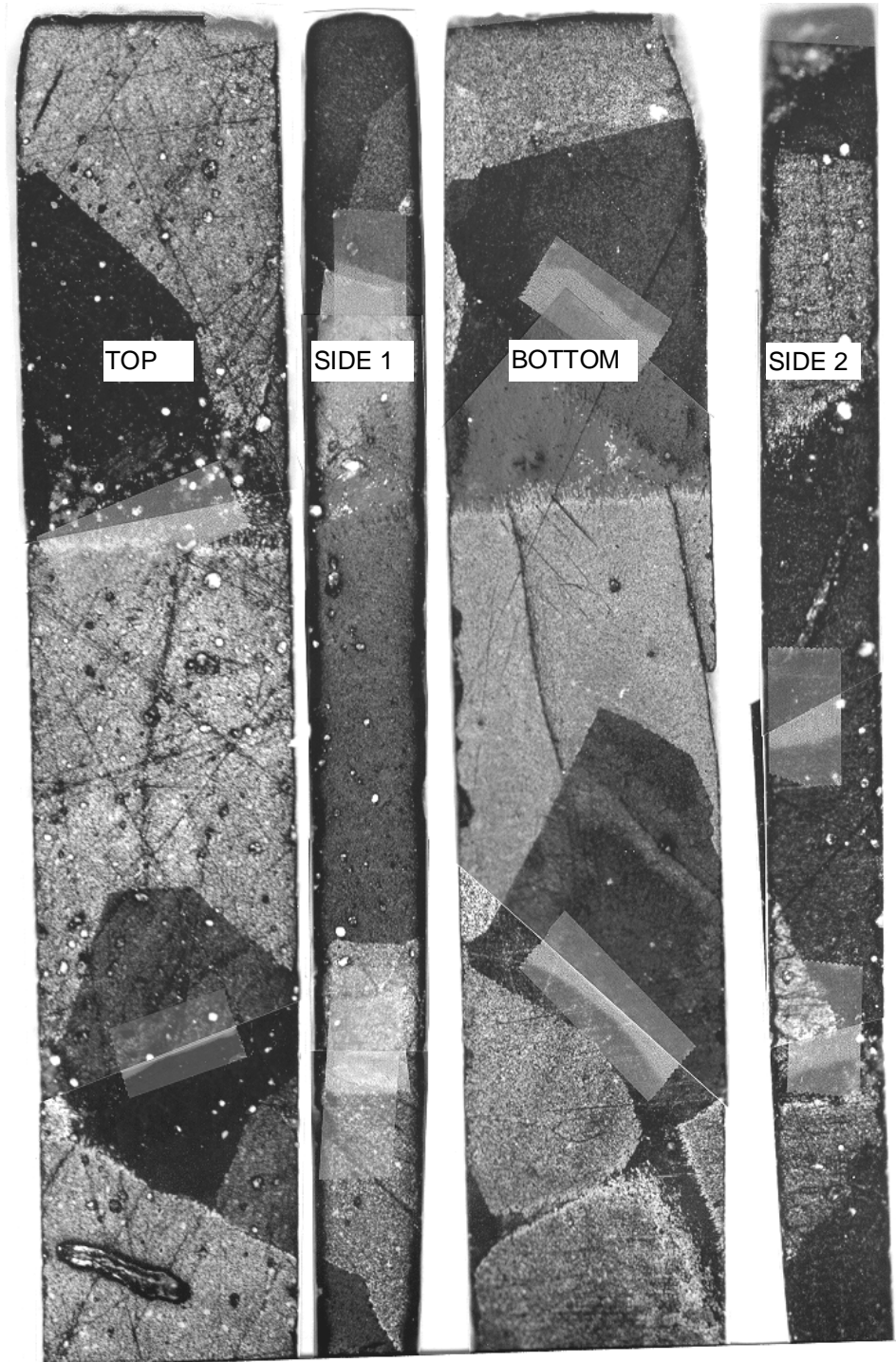


Figure 3-6) Polarized light micrograph of a melt-textured sample from AT&T[44] that was polished in bar form on four sides. Placing these images together, one can choose a direction to polish from so as to isolate a desired bicrystal.

Misorientation Determination - X-Ray Pole Figures

The characterization of the absolute orientation of individual crystals of melt-textured (MT) YBCO and the relative misorientation between two crystals is far more complicated than in the flux grown or thin film cases. In these latter two cases the misorientation is relatively simple; in thin films, the misorientation is constrained by the substrate. For flux-grown (FG) bicrystals the c-axis is generally perpendicular to the surface, which allows for simple inspection of the angle between the two sets of twins to attain the crystal misorientation. In MT samples, the c-axes are in general not normal to the surface, so that the simple twin misorientation cannot be used, and the crystal misorientation between adjacent grains does not necessarily involve rotations about low index poles. Moreover the grain boundary plane is not straight even on a macroscopic scale, meandering throughout the sample (**Figure 3-7**). Thus the *crystal* misorientation can be determined but not the full *grain boundary* misorientation (crystal misorientation plus grain boundary plane inclination). The crystal misorientation scheme used in this thesis is the one-axis, one-angle misorientation scheme (e.g., $20^\circ[3\ 1\ 0]$) preferred by material scientists[118]. When the common axis is not one of low index, visualization can be difficult, but this description simplifies the misorientation into one angular component (the Euler angle description has three angular components). The issue of the general effect of the macroscopic grain boundary plane direction is addressed in a later experiment

(Chapter 4). For a fuller explanation of the misorientation description and an example on how experimental data is converted into an angle/axis pair, see Appendix A.

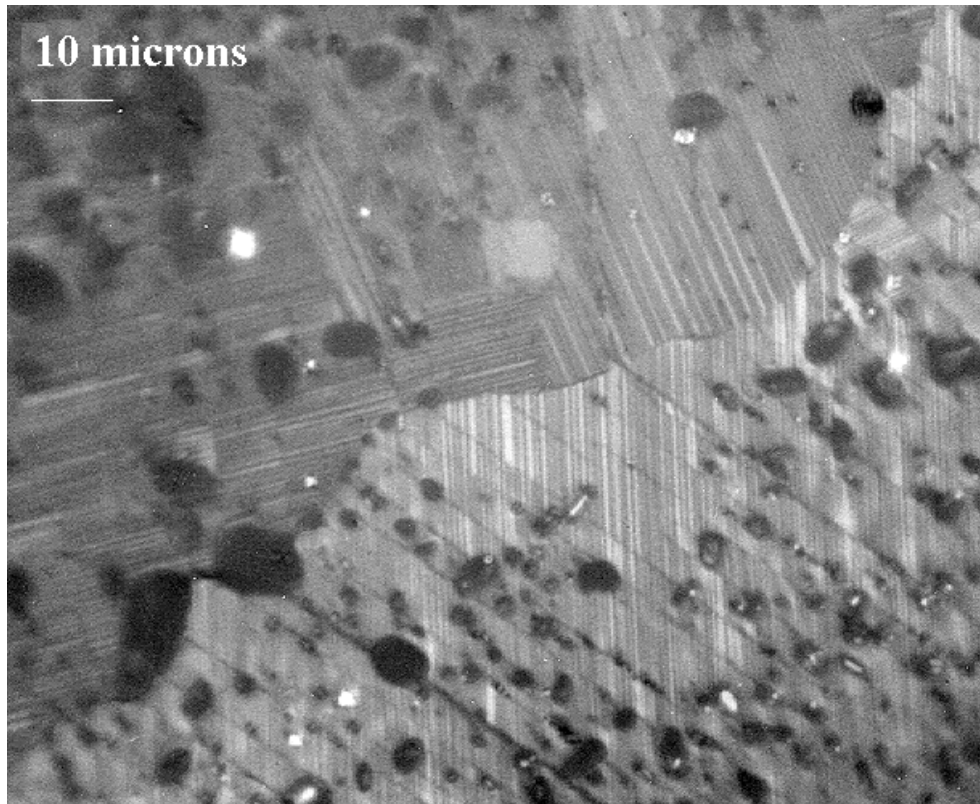


Figure 3-7) A melt-textured high angle grain boundary (MT4C2.2 - $57^\circ[17 \ 11 \ 2]$) viewed under polarized light. Twins do not intersect at 90° , indicating that both grains have inclined c-axes. The grain boundary plane is macroscopically wavy.

A quick way to qualitatively determine the misorientation is by the cross-boundary contrast under polarized light. It is known that anisotropic materials have different optical characteristics for grains of different orientations under polarized light[119], so that for a material of the same phase, grains of increasing misorientation will have increasing

contrast. Reflected polarized light contrast can also indicate oxygen depletion in YBCO[120], as well as the presence of second phase.

One popular experimental method for determining the misorientation of bicrystals in materials science, X-Ray Laue photography, was not feasible for these MT bicrystals as the equipment required very large grains (several mm). Moreover the large number of randomly oriented 211 particles would clutter the x-ray photograph. However, a second x-ray experimental technique, a modified x-ray pole figure technique, was used successfully. A pole figure is generally used for determining the texture of polycrystalline material[121]. Recently, the texture of YBCO MT samples[122,123] have been determined by the Schulz Reflection Method. At the UW, the experimental pole figure setup I used included a Scintag PAD V Diffractometer with Four Circle Sample Holder for raw data collection and a variety of software programs for control of the system and analysis of the data. The x-ray wavelength used was $\lambda_{\text{CuK}\alpha}=1.54\text{\AA}$. For MT bicrystal misorientation determination, there are only two crystals in the sample, so what is searched for are the singular occurrences of poles from the two crystals. Since the individual crystals were often quite large ($\sim >250\mu\text{m}\times 250\mu\text{m}$), there is enough signal for poles from single grains to be detected. The experiment was done by fixing the Bragg condition to a pole of interest (e.g., for the (006) pole, $2\theta=46.64^\circ$) and scanning ϕ over a the surface of a partial sphere around the sample surface normal (**Figure 3-8, Figure 3-9**). The angles 2θ and ω are the traditional Bragg-Brentano diffraction angles; these are set at specific values for peak (and off-peak, if desired) data collection, the value depending on the pole being measured. The angle χ represents the rotation of the sample holder around an axis in the plane of the sample

surface. The χ angle can range from 0° to 80° with reflection methods (transmission methods are required for the final 80° to 90° and can only be done on samples $< \sim 20\mu\text{m}$ thick). The angle ϕ represents the rotation of the sample holder about the surface normal. This angle is always scanned from 0° to 360° . Coupled with the χ movement, this creates the cone of scanned surface from which the poles of the bicrystal were detected, and the results are then plotted on a stereographic projection.

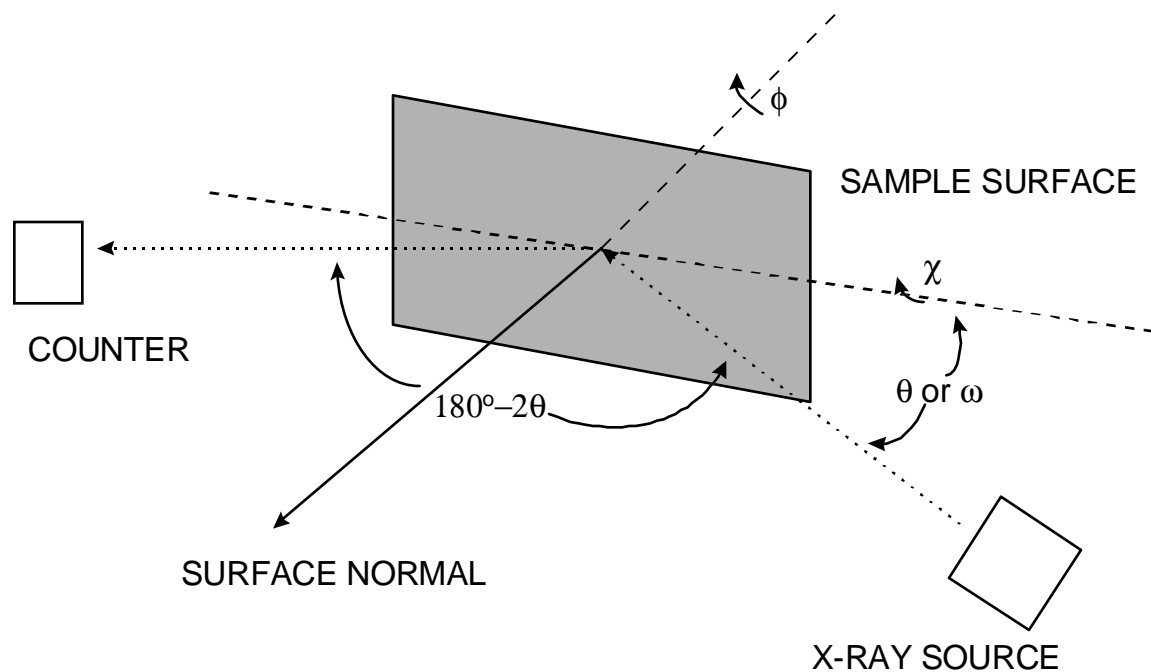


Figure 3-8) Schematic diagram of the x-ray pole figure apparatus showing how the key angles θ , χ , and ϕ are related to the x-ray source, detector, and sample.

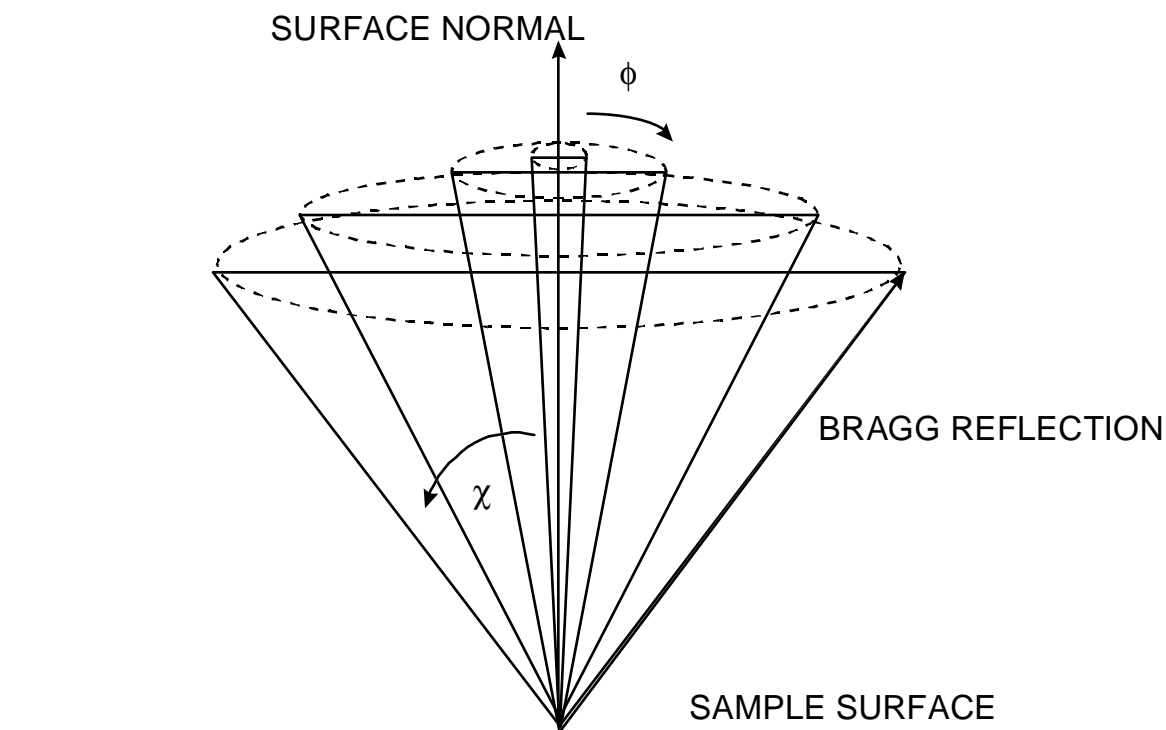


Figure 3-9) Schematic diagram to show how rotations of ϕ produce Bragg reflections which lie on a conical surface. Maximum χ in reflection mode is $\sim 80^\circ$ and ϕ rotates the full 360° for each χ .

Traditional pole figures evaluate the texture of a polycrystalline material with small grain size, and so the step size is traditionally rather large (5°) in χ and ϕ . With my bicrystals such a step size would skip many poles, so a much smaller step size (2° or 1°) was required. Still, the pole figure gives only the approximate location of the pole. A pole figure is based on the user defined value for 2θ , but the actual 2θ peak locations can shift from the predicted due to the oxygenation state of the sample, defocusing effects (because the sample surface is slightly in front of the x-ray focal plane), etc., and so each pole reported in a pole figure must be manually checked. **Figure 3-10** shows an initial,

unrefined pole figure which is used to obtain the approximate χ and ϕ positions of the poles of interest. It is important to remember that the software used to display this information expects a polycrystalline matrix, and will artificially extend out the range of χ and ϕ in which significant signal is actually detected. At each approximate location, a 2θ scan is run and the peak intensity is recorded to verify its intensity (**Figure 3-11**). The sample is then stepped by increments of 1° in χ and ϕ (note that the true angular distance resulting from stepping in ϕ will depend on the χ value) so that an intensity map giving the peak's centroid is created (**Figure 3-12**). Poles which I have studied include the (006) pole (c-axis pole) at 46.64° 2θ , the (020) at 46.70° and the (200) at 47.50° (the a- and b-axis ("a/b") poles) and several other low index poles, like the (110) at 32.85° and the (103)/(013) poles at 32.54° and 32.82° . The a/b poles occur at the same location on a stereographic projection, due to twinning. The fixed and known relationship between the various poles of the same crystal allows easy discrimination between poles of the two crystals (**Figure 3-10**). The c and a/b poles are mutually separated by 90° ; the (110) is both 45° from a/b and 90° from c; the (103)/(013) poles are 45° from a/b and 45° from c, etc. Knowing this information, and with only two crystals, it is easy to identify which poles belong to which grain. Placing all the pole information on a stereographic projection gives the orientation of each crystal with respect to the surface normal, as well as the misorientation between the two crystals. This data was then transformed into the misorientation matrix and the axis/angle misorientation description (see **Appendix A**). If it was desired to find out which poles belonged to a specifically identified grain, a material of

appropriate thickness and with 2θ pole peak locations not interfering with the poles of YBCO (e.g., aluminum), was placed on one grain to block the x-rays, and another pole figure is performed on the uncovered grain. It is noted here that an x-ray pole figure with $\lambda_{\text{CuK}\alpha}=1.54\text{\AA}$ does not penetrate the entire thickness of the sample and that the pole figure is dependent mostly on reflections near the surface. For example, signal from $\sim 15\mu\text{m}$ deep within a YBCO sample will have only 10% of the strength of the signal coming from the surface layers.

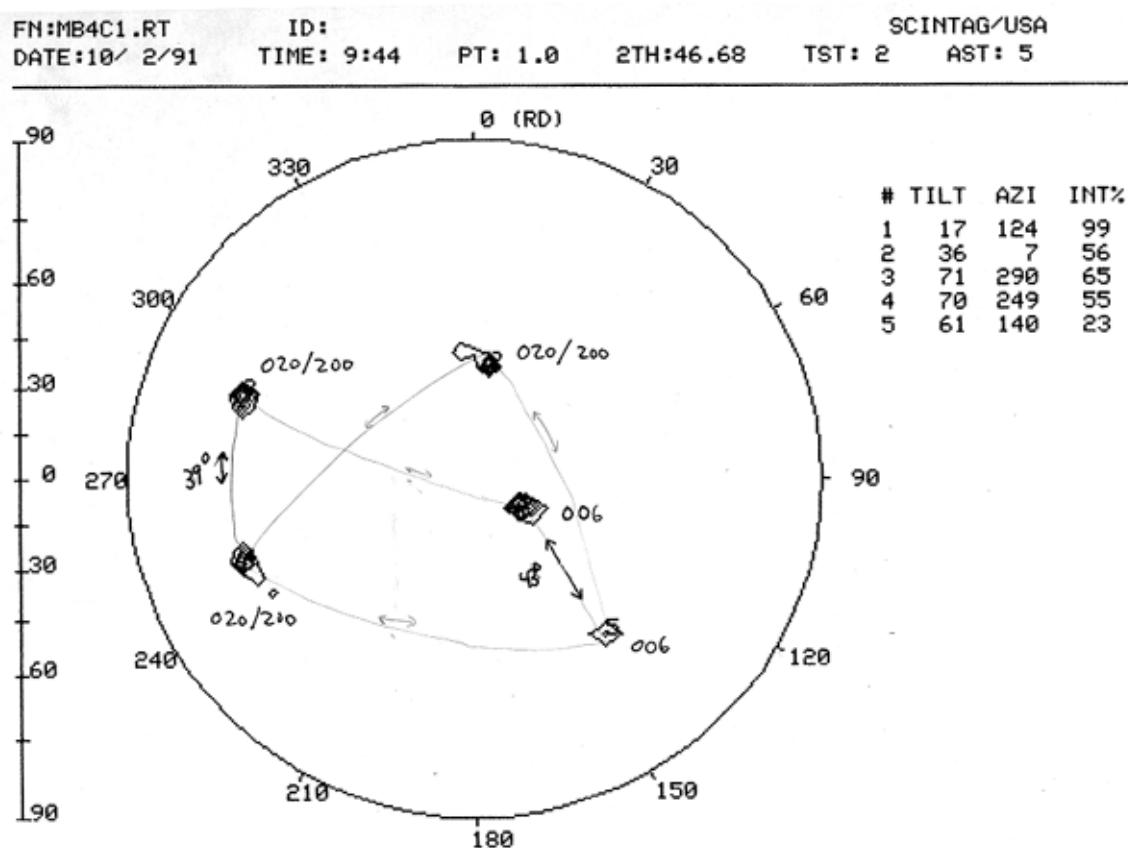


Figure 3-10) Automatic “raw” pole figure data for sample MB4C1. The location and width of the labeled poles are used to approximate the pole centroids. They are then located manually by scanning in 1° increments.

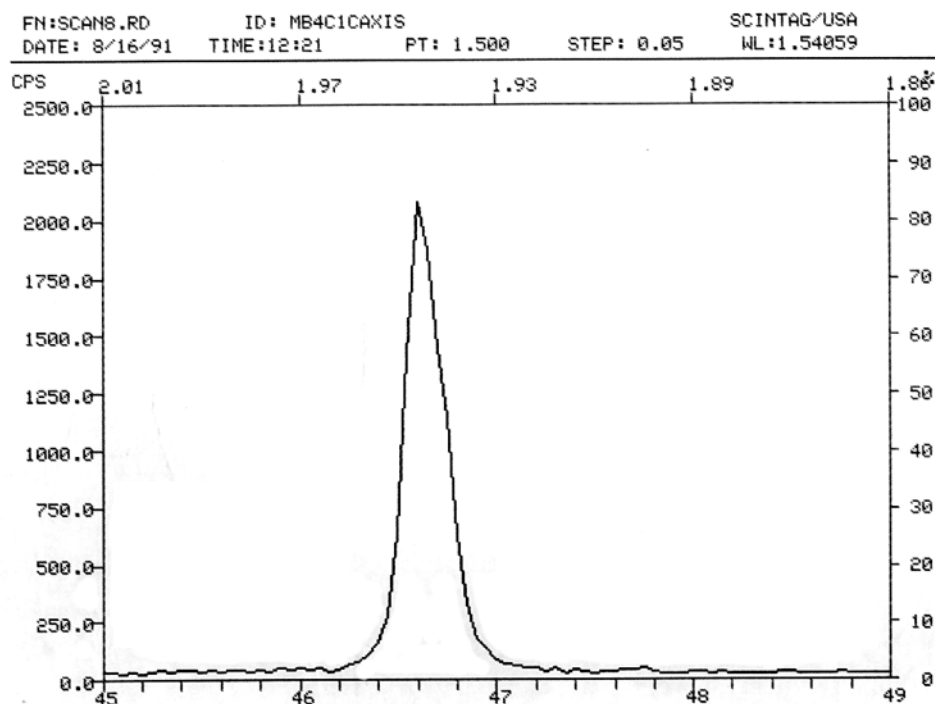


Figure 3-11) A 2θ scan for the (006) pole of a sample (MB4C1) located at $\chi=62^\circ$ and $\phi=277^\circ$ shows a peak intensity of ~ 2100 counts per second at $2\theta=46.6^\circ$.

$\phi \downarrow, \chi \rightarrow$	77	78	79	80
96	X	X	1600	X
97	X	1500	1800	X
98	2500	3300	2500	1500
99	X	1800	1500	X

Figure 3-12) Map showing the centroid of a c-axis via the peak counts per second values (X=not measured) at an experimentally determined $2\theta=47^\circ$ for sample KS4B2. The centroid is at $\chi=78^\circ$, $\phi=98^\circ$, width $\sim \pm 1^\circ$.

Another experimental technique for misorientation determination involves use of an Electron Backscatter Detector in a Scanning Electron Microscope (SEM)[124]. Kikuchi patterns are obtained on a florescent screen and a computer program can be used to obtain the orientation of the crystal in question. The great benefit of this technique is the high speed of data collection and the capability of testing very small samples (e.g., sintered grains since the technique requires only about $1\mu\text{m}^2$ of surface). One sample, SJ3151B3, was analyzed in this manner at the facilities of Argonne National Laboratory with B. Vuchic.

Electromagnetic Testing

After bicrystals were cut and their misorientation determined, they were contacted for electromagnetic measurement. Originally, samples were to be patterned with gold voltage contact pads and probed directly in situ with micromanipulators[125] as current was fed into the sample. This method was discarded in favor of the more flexible method of attaching small wires directly to the sample. The bicrystals were mounted on small ($\sim 0.8\text{mm} \times 7.5\text{mm} \times 13.5\text{mm}$) sapphire substrates (an electrical insulator with good thermal conductivity) which could be mounted on a variety of test rigs. Bicrystals were first fixed to the sapphire with silver epoxy, which was cured on a hot plate ($\sim 200^\circ\text{C}$) for ~ 2 minutes. Wires of varying thickness, from $10\mu\text{m}$ - $100\mu\text{m}$ (the choice depend on the available contact area), were then attached to the sample with the same silver epoxy. The contact footprint (wire+epoxy) was generally ~ 2 - 3 times the wire diameter. After curing at 200°C , the bicrystals were further oxygenated at 400°C for 1 hour, a treatment which also allowed the silver to diffuse through the surface and make good electrical contact. The contact resistivity of the samples was typically in the $\sim 10^{-5}$ - $10^{-4}\Omega\text{cm}^2$ range.

Cracks are a major concern when dealing with melt-textured YBCO. With small samples, cracks can propagate across an entire cross-section, leading to dissipation, heating, and destruction of the sample. At the very least, cracks are an extrinsic source of dissipation and so mask the true effect of the grain boundary. Care was taken to avoid

selecting bicrystals with cracks, and to note if a crack that propagated after selection (due to thermal cycling) was responsible for dissipation in a sample.

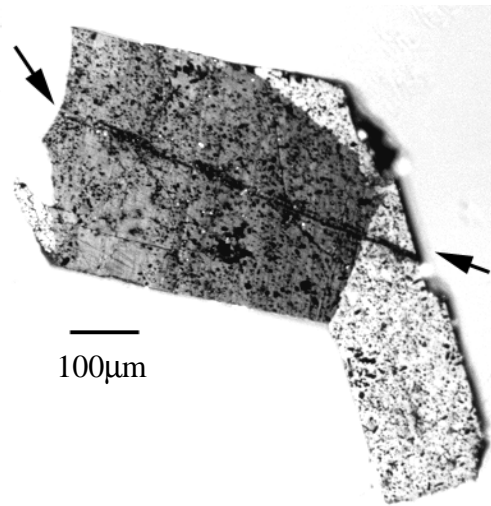


Figure 3-13) Polarized light micrograph of a UW MT sample was not measured because of the crack which extended across both grains.

The standard experiments performed on these melt-textured samples were AC variable temperature resistance traces and constant temperature DC V-I traces as a function of magnetic field. The AC system was composed of a Lakeshore 91C temperature controller, EG&G/PARC Model 124A Lock-In Amplifier with Model 116 Differential Preamp and a Kepco 2A Bipolar Operation Power Supply (BOP) (**Figure 3-14**). The AC technique was chosen for low noise and to eliminate thermal offset voltages, as well as to allow a more sensitive measurement of any low voltage T_c tails. The drive AC current and the voltage response were read by the lock-in amplifier set to a specific frequency (in our case, 43Hz). Small voltages could be compared to the out-of-phase signal to verify if the

dissipation was above the noise level ($\sim 10\text{nV}$ or less). The sample temperature and voltage is recorded as the sample is cooled in a He gas filled rig to 77K (or 4K if necessary).

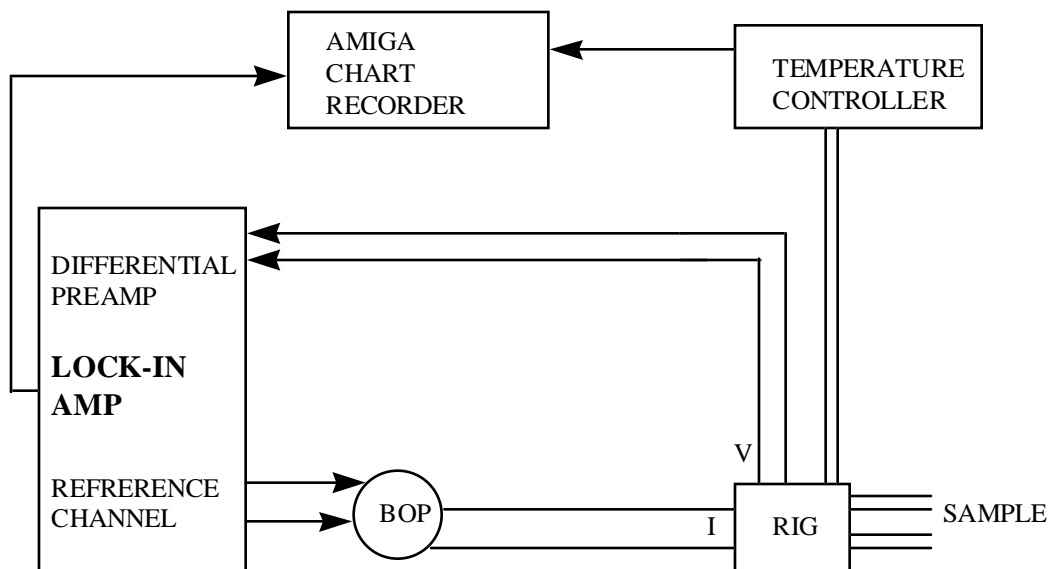


Figure 3-14) Schematic diagram of the AC T_c experimental system. The sample is cooled in a He gas filled rig, down to either 77K or 4K. The temperature sensor in the rig is read by the temperature controller and relayed to the computer chart recorder. The voltage signal (at the same frequency and phase as a generated current of a known level) is read by the lock-in amplifier and sent to the computer chart recorder. Data is displayed as voltage versus temperature, but this is easily converted to resistance versus temperature as the current level is preset.

The DC V-I system was originally composed of a two Keithley 195A multimeters, and a Kepco 2A BOP which was controlled by hand or by a ramp generator. The voltage was read by a Keithley 150B or a Keithley 155 microvoltmeter (**Figure 3-15**). A separate constant current source was used to power the copper coil magnet to apply small magnetic fields (up to ~ 30 mT). Data were collected by Amiga computers running x-y chart programs.

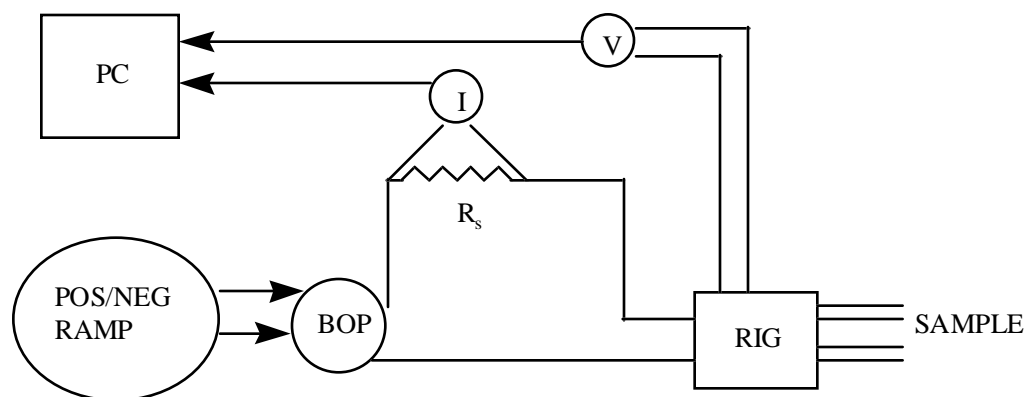


Figure 3-15) Schematic diagram of the DC V-I measurement setup. A ramp controller manually triggered a BOP to provide the current for the sample while a DC voltmeter read the response.

Two magnets were used in conjunction with the above experiments. For low magnetic fields (up to several tens of mT), a copper coil mounted on the sample rig was sufficient. High magnetic fields were achieved in a Nb-Ti superconducting 7T magnet with a liquid helium pool boiling sample space.

Results

Table 3-1: Summary of misorientation, T_c , grain boundary J_c electromagnetic coupling, and grain boundary resistivity (ρ_{nd}) for UW and AT&T manufactured MT bicrystals.

Name	Misor. Angle θ	Misor. Axis	T_c (onset)	T_c (R=0)	$J_{c(g.b.)}$ 0G,77K, A/cm ²	Coupling	ρ_{nd} ($\Omega\mu\text{m}^2$) 77K
MB4C3a	15°	[2 1 0]	91K	89K	3950	mixed	0.3
MB4C3b	15°	[2 1 0]	91K	90K	3400	mixed	0.3
MT4C2.1	22°	[1 0 0]	92K	90K	3500	mixed	0.3
SJ3151B3	45°	[6 $\bar{3}$ $\bar{5}$]	92K	88K	1140	weak	1.3
MB4C4	48°	[1 1 0]	91K	89K	750	weak	8.0
MB4C1	55°	[$\bar{2}$ 3 $\bar{1}$]	92K	90K	75	weak	2.8
MT4C2.2	57°	[$\bar{17}$ $\bar{11}$ 2]	92K	90K	425	weak	8.7
SJ3151B4	69°	[5 6 0]	90K	84K	670	weak	14
<i>MB4C5</i>	6°	[$\bar{19}$ $\bar{4}$ 5]	74K	67K	9000(4K)	<i>strong</i>	<i>N/A(4K)</i>
<i>MB4B1</i>	28°	[1 0 0]	85K	48K	1200(4K)	<i>weak</i>	<i>7.9(4K)</i>
<i>MB4C6</i>	36°	[1 4 1]	74K	60K	500(4K)	<i>weak</i>	<i>4(4K)</i>

The misorientation angle/axis pair and electromagnetic data are summarized in **Table 3-1**, **Figure 3-16**, and **Figure 3-17**. Six of the samples had $T_c(R=0)$ values and R(T) traces typical of optimally oxygenated YBCO (**Figure 3-18** and **Table 3-1**), in that they had a linear, metallic normal state behavior and $T_c(R=0)$ values~89-90K. Two samples

(the “SJ” set) had transitions that started at 91K, but these had $T_c(R=0)$ values less than ~ 90 K with resistive tails (**Figure 3-19**) believed to be caused by dissipation at their grain boundaries. Three samples had T_c values below 77K (the italicized data in **Table 3-1**).

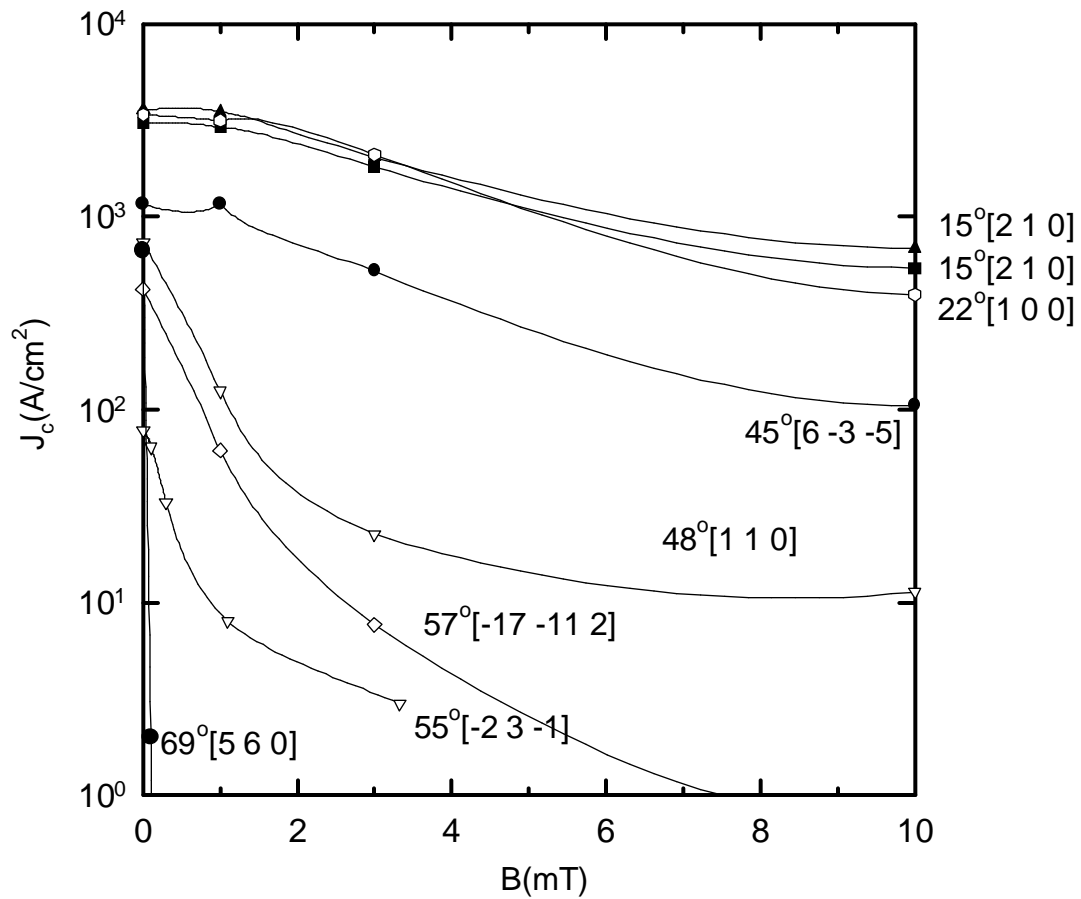


Figure 3-16) Plot of $J_c(B, \theta, 77K)$ characteristics for melt-textured bicrystals at low magnetic fields. Zero field J_c decreases and the field dependence of J_c increases with increasing misorientation.

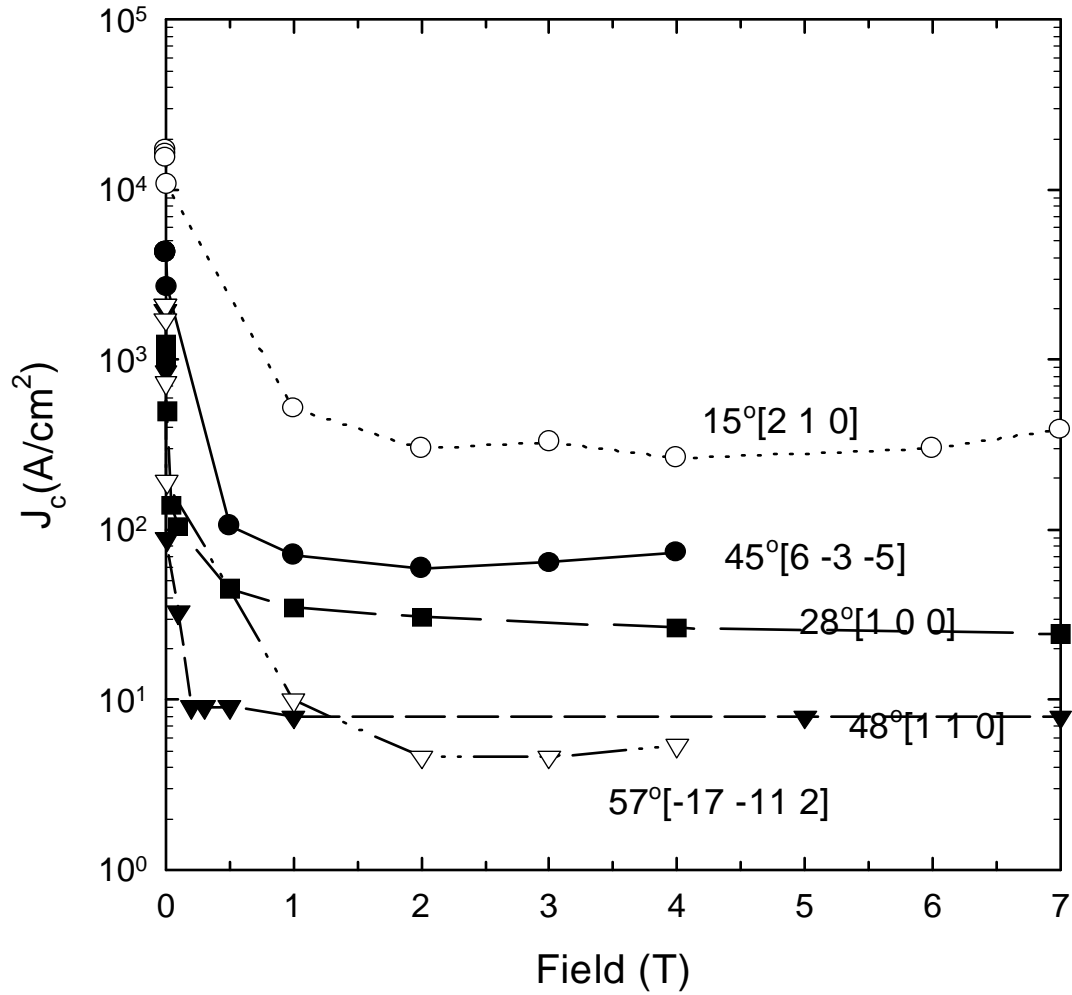


Figure 3-17) High field residual critical currents measured in five melt-textured high angle boundaries at 4K. Higher angle boundaries tend to have lower J_c values.

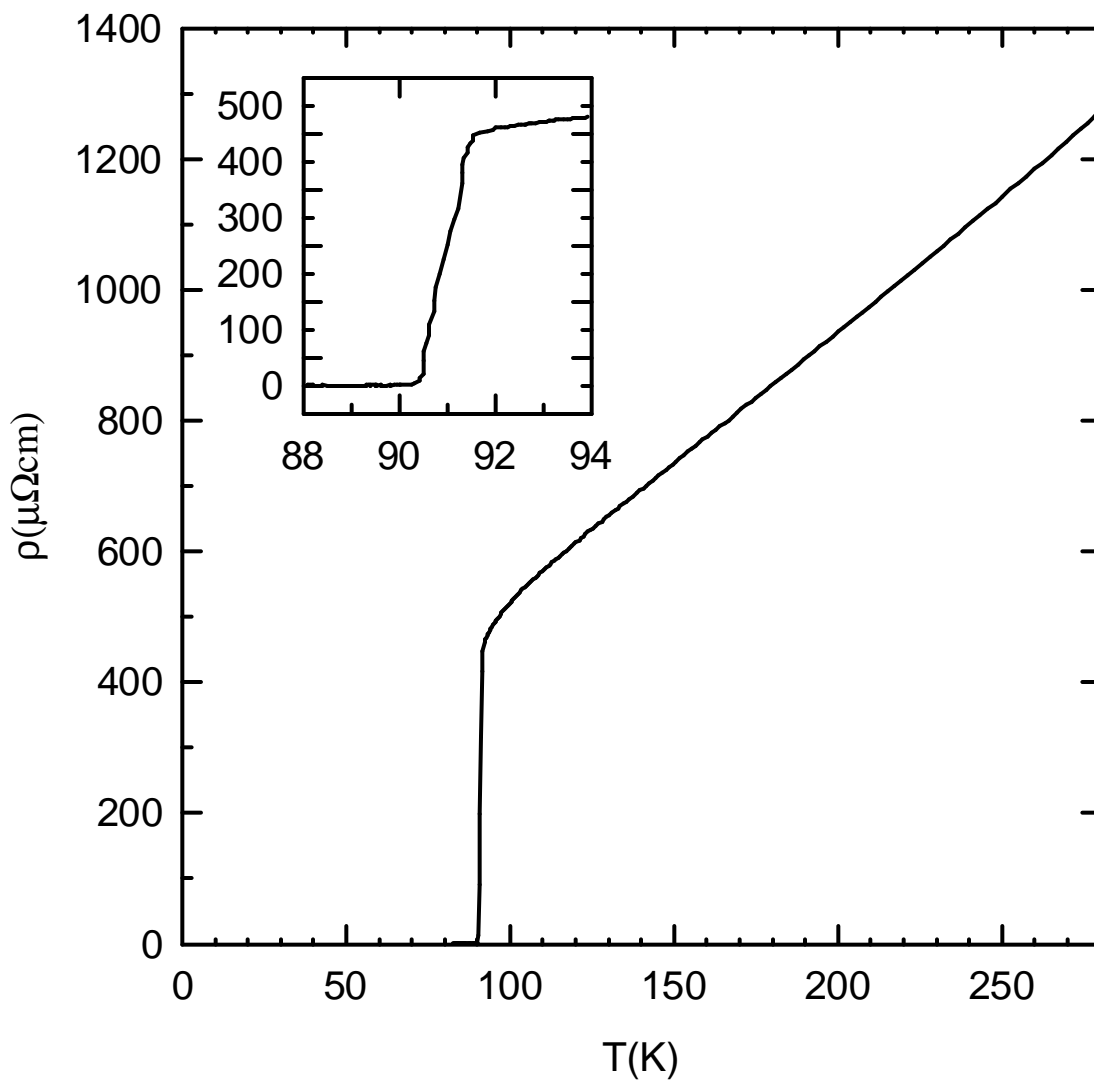


Figure 3-18) A typical AC Resistive T_c trace across a melt-textured boundary (sample MB4C3b). The T_c onset is at $\sim 91\text{K}$, with zero resistance occurring at $T=90.2\text{K}$.

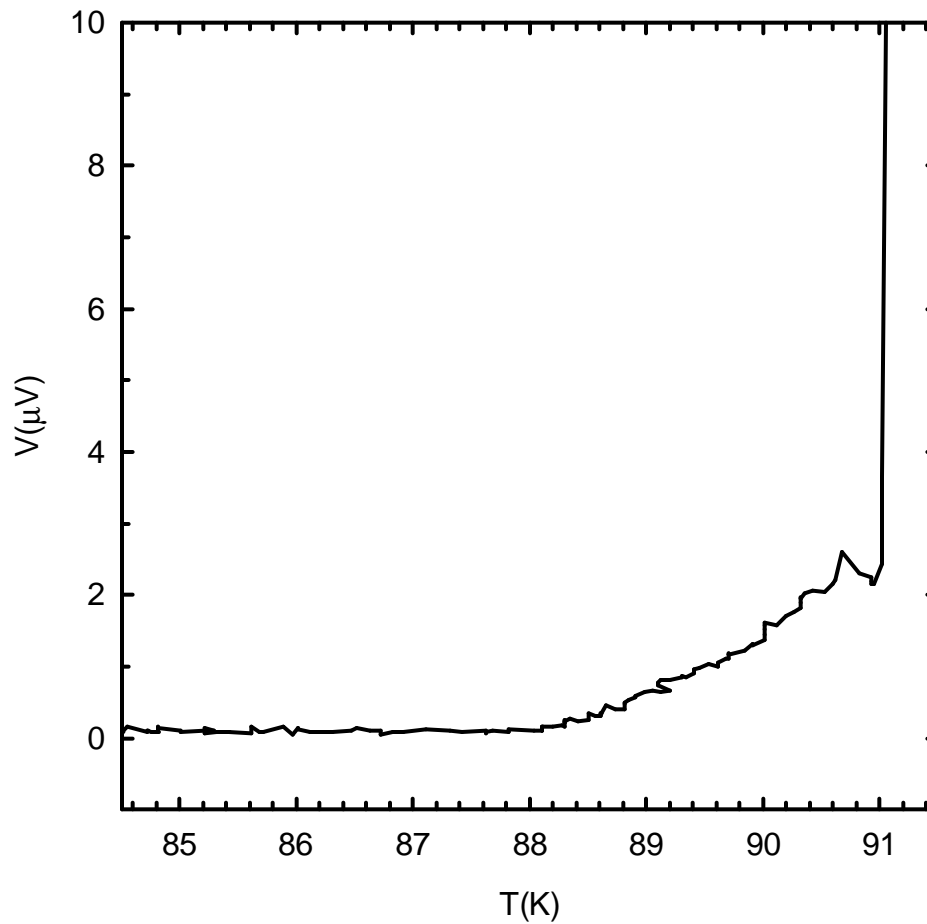


Figure 3-19) For sample SJ3151B3 the T_c onset is at 91K, but a resistive tail, believed to be due to dissipation at the grain boundary, is visible down to 88K for a measuring current of 10mA ($J \sim 100\text{A}/\text{cm}^2$).

The V-I traces of all samples were Josephson-like (**Figure 2-14**) at low fields, showing an abrupt transition behavior rather than exhibiting the rounded behavior of flux flow observed in fully coupled boundaries[4]. From the 77K data summarized in **Figure 3-16**, we see that there is however a considerable variety of J_c sensitivity to low magnetic fields. As the misorientation angle increased, the zero field J_c decreased and the samples became more sensitive to applied field. While most of the samples had J_c values at 77K that were depressed below our measurement capability when multi-Tesla fields were applied, two smaller angle samples did show a plateau-like J_c behavior out to the highest magnetic field measured (7T) (**Figure 3-20**). At 4K, all measured bicrystals featured the sharp low-field drop-off characteristic of weak-coupling, followed by the much milder $J_c(B)$ dependence at higher fields (**Figure 3-17**) usually associated with strong coupling behavior.

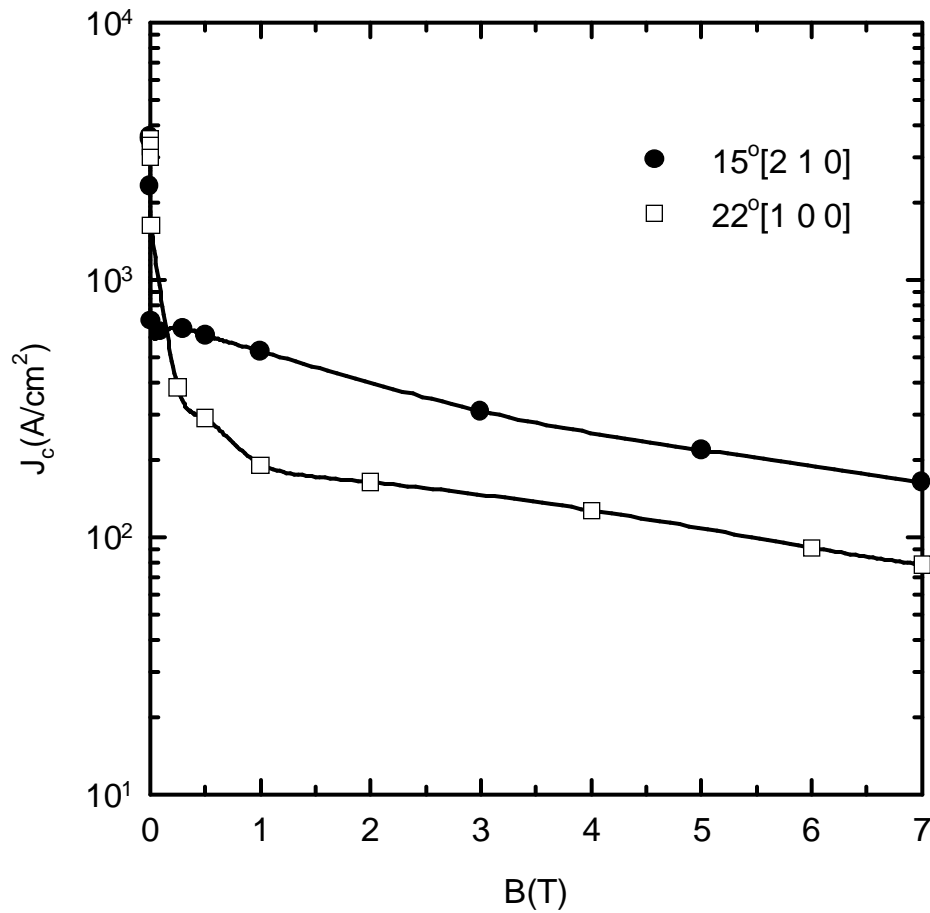


Figure 3-20) Two bicrystals exhibited a sharp low field depression of J_c but then exhibited a much slower fall off in strong fields at 77K (B is not $\parallel c$ for either sample).

Discussion

The T_c values for the first 8 out of the 11 samples presented in **Table 3-1** were close to the expected 92K value for YBCO. Resistive tails, which depress $T_c(R=0)$, can easily occur for weakly-coupled samples when the measuring current is on the order of the critical current. As for the three samples that had $T_c(R=0)$ below 77K, there are several possible explanations. One is that samples incorporated Al from the alumina ceramic sample boat during melt-texturing, as Al incorporation has been shown to significantly depress T_c [117]. This is a reasonable explanation for samples MB4C5 and MB4C6 as the depressed onset of the T_c (~74K) indicates that the intragranular regions also had depressed T_c , and Al incorporation would effect the intragranular regions as well the grain boundaries. For sample MB4B1, which had an onset T_c of 85K, near the expected value, a more likely scenario is Ba-Cu-O second phase contamination at the grain boundary. Sample MB4B1 had 10% of added 211, the only bicrystal not to have 20% of added 211. The effect of adding 211 was that there was far less $BaCuO_2$ and CuO in both grains and grain boundaries.

All the samples exhibited some weakly-coupled characteristics in low applied magnetic fields. However, a most striking observation is that the magnitude of $J_c(0T, 77K)$ decreased and the field dependence of J_c increased in a progressive manner as θ increased

(Figure 3-16). This result appears to indicate that the transition from strong coupling at smaller angles to weak coupling at higher angles is progressive, rather than abrupt.

The grain boundary resistivity ($\rho_n d$) is a normal state property that often correlates with the superconducting character. It has been traditionally used to characterize Josephson Junctions (JJ)[101]. It can be found experimentally through the relation $\rho_n d = R_n A$, where R_n is the dynamic resistance from the V-I trace and A is the grain boundary area (d is the grain boundary thickness, an unknown quantity). From **Table 3-1** it is shown that $\rho_n d$ increases with increasing misorientation, and has values comparable to those (~ 1 to $90 \Omega \mu\text{m}^2$) earlier reported by Larbalestier et al.[20] for weakly-coupled flux-grown bicrystals and to the values of ~ 0.02 to $8 \Omega \mu\text{m}^2$ reported by Dimos et al. [14] for thin film bicrystals. Thus these MT grain boundaries apparently have similar normal state properties.

Another point of interest in the results is the appearance of a largely field-independent $J_c(B)$ in fields above $\sim 1\text{T}$ at 4K (**Figure 3-17**). A somewhat similar characteristic was observed in some bicrystals at 77K (**Figure 3-20**). In polycrystals, this behavior has sometimes been attributed to the residual supercurrent of a minority percolative path[126] of small cross section. However, others suggested that the field independent $J_c(B)$ may be due the behavior of individual grain boundaries, not necessarily percolation[127,128]. These results support the latter suggestion, in that a field-independent $J_c(B)$ is seen even for bicrystals. Somewhat similar characteristics were observed by Daümling et al.[129] on a $25^\circ[001]$ symmetrical tilt thin film bicrystal whose

characteristics in zero field at 5K could be modeled as a resistively-shunted JJ. Thus it appears that a finite high field, quasi-plateau character might be attributed to JJ behavior, a possibility originally discussed by Yanson[23] in the context of the residual current of a tunnel junction. Another explanation is that there are minority strongly-coupled regions in parallel with majority JJ regions. At zero field, all regions contribute to the critical current. As magnetic field is applied, the JJ regions no longer carry current and all the supercurrent is now carried by the strongly coupled regions. Probing the possibility of the two channel model in further detail, with high sensitivity V-I measurements and magneto-optic imaging, is an important part of the experiments described in **Chapter 4**.

In summary, the data from these initial experiments suggested that simple descriptions based on the rather digital concepts of weakly and strongly coupled boundaries are not adequate to describe the $J_c(B,\theta)$ behavior of general misorientation, melt-textured bicrystals. The data are much more consistent with a channel model, in which there is a considerable transition range between these limiting classifications. This transition range, perhaps lying from $\sim 10^\circ$ to 25° in general misorientation, features electromagnetic characteristics which exhibit both low field J_c sensitivity like a Josephson Junction and a significant high field critical current like a flux-pinning boundary.

Chapter 4 : Experiments with Melt-Out, Melt-Texture (MOMT) YBCO

The results in **Chapter 3** raised important questions as to the details and completeness of the transition from strong to weak coupling as misorientation angle increases, while at the same time underscoring the experimental difficulties of testing melt-textured bicrystals. This chapter details later experiments undertaken with perhaps “cleaner” samples (those made by the melt-out process). These experiments also benefited from improved bicrystal isolation techniques, magneto-optic imaging and more sensitive electromagnetic characterization.

The influence of grain boundary (GB) properties is difficult to determine when impurity contamination overwhelms the intrinsic properties. As noted in **Table 2.1**, three out of the 11 earlier bicrystals had significant enough GB contamination to severely depress the intergranular T_c . Clearly it is important to test samples with the cleanest grain boundaries available. To that end, melt-textured samples were made available from A. Parikh and K. Salama of the Texas Center for Superconductivity at the University of Houston (TCSUH). These samples were made by the melt-out melt-texture (MOMT) process[40], described in **Chapter 2**. This process is believed to result in less second phase and to leave fewer elemental impurities in the samples, although these points have not been explicitly verified. The key feature of the MOMT process is that melt-texturing on 211 blocks wicks away unreacted second phase liquid that otherwise tends to settle in the GB. The liquid absorbed into the 211 support block may also take away impurities like Cl which

could migrate to the GB[130]. Hence it is believed that these samples to be among the cleanest melt-textured grain boundaries available and ideal samples for bicrystal experiments.

The previous method of melt-textured bicrystal isolation, random fracture, resulted in extremely low yields of usable bicrystals and did not easily allow for preselection of a specific bicrystal from the polycrystalline matrix. A laser cutter system, capable of cutting a trough 30 μm wide through a sample 80 μm thick, was purchased to allow both specific bicrystal selection and a high yield rate of bicrystals from parent polycrystalline samples. The laser cutter also allowed isolated bicrystals to be subdivided further to probe the effect of the meandering GB plane. Recall that the characterization of my general misorientation grain boundaries is technically incomplete. Besides the angle/axis pair, the direction of the GB plane normal is needed for the full GB description[131]. This value was ignored however, as the boundary plane wandered extensively throughout the sample, making it impossible to describe the GB plane by any unique normal for a macroscopic melt-textured sample. I have also asserted that the crystal misorientation was the key parameter in GB character, and that the effect of the GB plane would be secondary. This idea was supported in thin film studies of Dimos et al.[14] on thin film twist and tilt samples. With the laser cutter, it became possible to cut a bicrystal into sub-samples with different macroscopic GB plane directions to perhaps as narrow as $\sim 5\mu\text{m}$ wide. Samples this narrow are not mechanically stable nor simple to contact for transport measurements, therefore my narrowest laser-cut bicrystal was 100 μm wide, and most were $\sim 250\mu\text{m}$ wide. Laser cutting allowed testing of the claim that the effect of the macroscopic GB plane would be

secondary to effect of crystal misorientation. Details of laser cutting and the specific laser cutter used in these experiments can be found in **Appendix B**.

The unusual flux-pinning like, high field critical currents on otherwise Josephson-like samples seen in **Chapter 3** are explored further in this chapter. Understanding whether these currents result from strongly coupled bridges or Josephson currents appears to be very important to future bulk transport applications for YBCO. If this residual current is due to strongly coupled bridges, it is of utmost interest to find out why such fractions are strongly coupled. Knowledge of this “good area” microstructure could be used to increase the “good area” fraction and to retard the onset angle of weak coupling.

Two new tools were used to probe these residual currents. One is magneto-optic imaging, a method by which a magnetic-field-sensitive film is used to image flux penetrating different regions of a sample (and GB). The other is probing the irreversibility field (H^*) across the boundary and within the grain using extended E-J measurements. Koch et al.[132] showed that the curvature of the E-J characteristics could be used to determine the location of the irreversibility line (i.e. the field $H^*(T)$ at which J_c goes to zero) of single crystal YBCO. Using this procedure, I identified H^* both for the inter- and intra-granular regions of my bicrystals. The goal of this analysis was to add a new tool which might help us understand the crossover from strong to weak coupling.

Sample Fabrication and Isolation

All but one of the bicrystals examined in this chapter were melt-out melt-texture (“MOMT”) samples from TCSUH. I received three large (~2cm × 2mm × 2mm each) bar-shaped, polycrystalline samples: KS1, KS4, and KS5. These samples were further cut with an ethanol-lubricated diamond saw, and then thinned by grinding to less than 100 μ m. Grain structure was identified in a polarized light microscope, and five general misorientation bicrystals, KS1B1, KS4B1, KS4B2, KS4B3 and KS5B1, were subsequently isolated by laser cutting. These bicrystals were further sectioned into smaller sub-samples, both to check the effect of the macroscopic GB plane and to lower the measuring current needed to reach I_c (high I_c can result in sample burnout even with pulsed current). Laser cutting resulting in bicrystals that were long enough (~2mm) to allow the placing of four voltage contacts, two in each grain, to measure the intragranular, as well as the intergranular critical currents.

The sole non-MOMT bicrystal measured in this chapter was extracted from a seeded bicrystal supplied by T. Luhman at Boeing. This melt-textured YBCO sample was made by a Sm-seeded growth technique[133], modeled after the ISTEC Sm-seed growth technique[134]. Two Sm-123 seeds were fabricated by a procedure similar to that used for the melt-texturing of Y-123. Sm-123 can be used as a seed because it melts at a higher temperature (the peritectic decomposition temperature of Sm-123 is ~1060°[135]),

and the seeds were cut such that the seed's ab planes were parallel to the sample surface. Two seeds were then placed on a sintered YBCO puck (approximately 5cm in diameter), the seeds being misaligned by the appropriate a/b misorientation. The sample was then melt-textured such that large melt textured grains grew out from the seeds (**Figure 4-1**), and the interference front created a GB.

The Boeing sample was cut and polished in the manner described for previous samples. The small bicrystal did not have the anticipated $\sim 30\text{-}50^\circ[001]$ orientation of the seeds, rather it was $\sim 38^\circ[3\ 1\ 1]$. This was probably because the seeds were not carefully oriented before texturing.

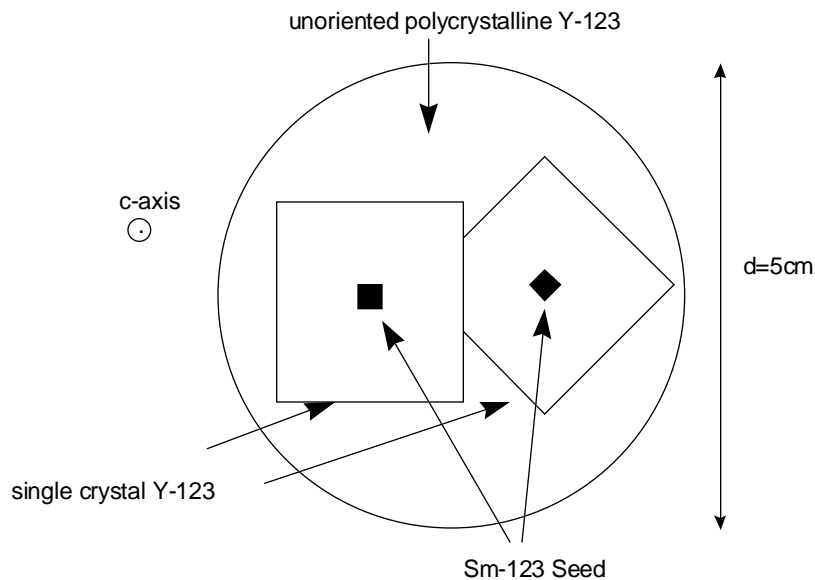


Figure 4-1) Illustration of seeded melt-textured bicrystal growth. Single crystals of aligned Y-123 grow from the Sm-123 seeds and create a grain boundary dictated by the misorientation of the Sm-123 seeds.

New Electromagnetic Techniques - Pulsed Current and High Voltage Sensitivity

Samples were wired as described in **Chapter 3**, but with the addition of intragranular voltage taps. These additional voltage taps were made possible (on all but one sample) by the larger bicrystal dimensions afforded by laser cutting. Samples were laser cut as long, thin rectangular bars (50-85 μm thick \times ~250-370 μm wide \times ~3-4mm long) so that the cross section was small (for lower I_c and lower heating) but the surface area large (for ease of contacting). Current leads were affixed with Ag epoxy to the ends of the samples and voltage taps were placed on the top surface, as shown in **Figure 4-2**. An attempt was made to improve the contact resistivity by sputtering gold pads to the surface (**Figure 4-3**) but this did not significantly lower the contact resistivity, as the contact resistance was about the same as samples without gold pads.

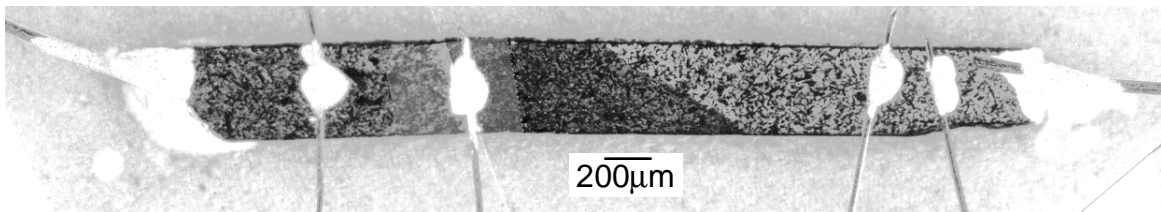


Figure 4-2) Polarized light micrograph of the wiring of a typical laser-isolated bicrystal (KS4B1a). The sample is only 85 μm thick and 370 μm wide, but ~3.5mm long, allowing space for four voltage taps. Note that the current leads are large and designed to feed current into the whole cross-section of the sample.

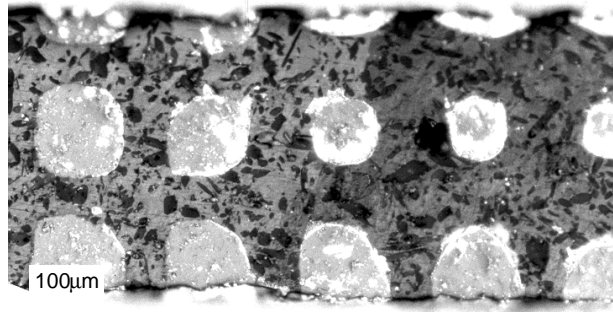


Figure 4-3) Gold pads, ~50-100 μ m in diameter were sputtered on the surface through a copper grid in an attempt to get lower contact resistivity (Sample KS4B1c).

When the currents exceed ~ 1 A, samples would generally quench, causing an incomplete and discontinuous V-I trace. Often the samples would catastrophically melt due to heat dissipation as the voltage onset (either near the current leads or at a weak point, e.g., crack in the sample) overcame the cooling power of liquid nitrogen. The use of pulsed, rather than DC current helped prevent this quenching. The UW pulsed-current system developed by Harry Edelman[136] features a Phillips 5139 function generator, two Hewlett-Packard 3458A voltmeters (one for determining current) and a Kepco 7A BOP (**Figure 4-4**). The function generator sends a 1ms pulse to the BOP, and this current creates a voltage response that has inductive spikes at the beginning and the end of the pulse. The measurement window is between these spikes (**Figure 4-5**). The longer the measurement window, the lower the point-to-point noise, but the larger the artificial baseline (due to the non-linear voltage response). I choose a 0.4ms delay and a relatively large 0.5ms measuring window. Despite this optimization for low noise, the noise level was still $\pm 2\mu$ V, about an order of magnitude higher than the earlier DC V-I measurements of

Chapter 3. Therefore, pulsed V-I traces were often repeated and averaged. While longer than 1ms pulses would allow for a larger voltage measurement window (and hence less noise), it also would increase the chance for sample burnout (even with the short 1ms pulses, some samples still burned out). Rest time between 1ms pulses was 99ms, which was required to allow the sample to cool between pulses when the sample is in the resistive state[136]. Computer control of the system was accomplished with the LabWindows software running on a PC.

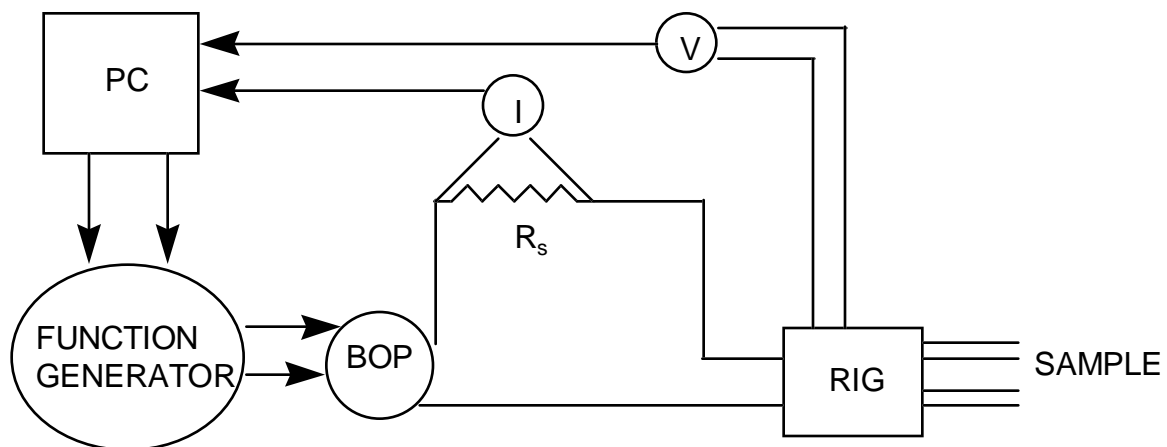


Figure 4-4) Schematic diagram of pulsed current experimental circuit. The computer triggers the function generator which defines the shape of the pulse. The function generator then creates the current pulse through the bi-operational power supply.

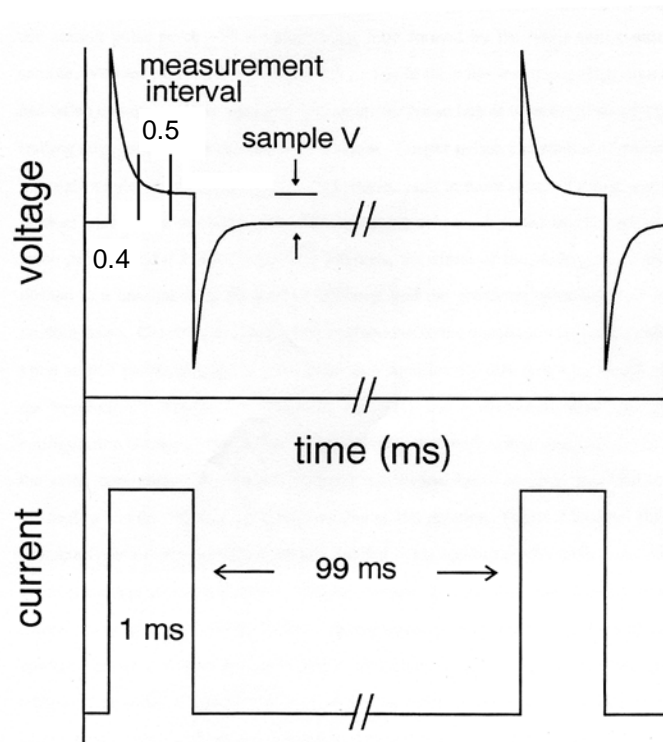


Figure 4-5) Plots of the current pulse and voltage response vs. time. The voltage response to the 1ms pulses has both a leading and trailing inductive spike. The choice of voltage measuring window results in a tradeoff between voltage noise and voltage baseline. Plots adapted from Edelman[136].

High magnetic fields (up to 12T) and variable temperatures were possible with an Oxford Instruments Nb-Ti/Nb₃Sn insert magnet system. For precise low field measurements, a 1T electromagnet was purchased with a LN₂/He cryostat to allow for precise field selection in the regime between 0mT-1.1T (precision of ~0.1mT at low fields).

High voltage sensitivity is needed to probe the glass transition or irreversibility field in high T_c superconductors[132]. My interest was to compare the field at which this transition occurs both across the GB as well as inside the grains. The high sensitivity DC

V-I experimental setup consisted of a Keithley 2001 voltmeter with a 1801 pre-amp, as well as the Keithley 224 Programmable current source (**Figure 4-6**). The voltmeter/pre-amp combination has a possible peak-to-peak noise level of 0.6nV, but noise from the rig, sample to substrate and external connections increased this to several nV. The Keithley current source allowed digital control of the current with a precision of 5nA.

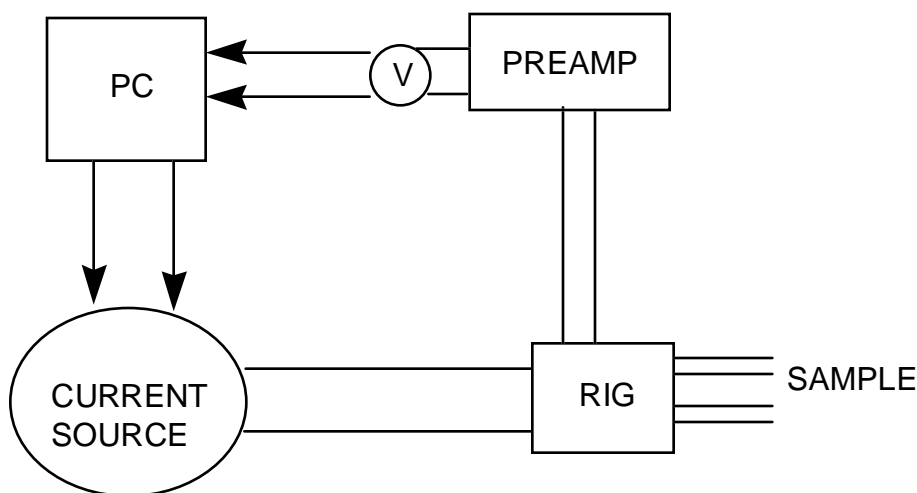


Figure 4-6) Schematic diagram of the high sensitivity V-I experimental setup. The key feature is the Keithley voltmeter/preamp combination which can achieve nV sensitivity under optimal conditions.

Because of the arbitrary orientation of the two grains in each bicrystal and the arbitrary plane of their cut, it is clearly impossible to orient the samples in any systematic way, such that both crystals in the bicrystal have a consistent orientation with respect to the magnetic field. Knowing the surface normal and the misorientation, we mounted the bicrystals such that the field was oriented within approximately 10° of the c-axis of at least one of the two crystals in each bicrystal for the higher field H^* experiments. This was

because the $H \sim ||c$ condition (the low H^* direction, $\sim 5T$ in YBCO) allowed enough field range with the 12T magnet to measure the change in voltage curvature. For all other transport experiments, mounting the sample $\sim H || c$ was not required and usually the sample was mounted so that the c-axes of the crystals was $\sim H \perp c$.

Magneto-Optical Imaging

Magneto-Optical imaging has been used to visualize the flux penetration in high temperature superconductors[137] including the grain boundaries in melt-textured YBCO[138]. My interest was to correlate the electromagnetic properties with magneto-optic observations of the details of the flux pinning inhomogeneities at the GB on a scale on the order of $\sim 5\mu\text{m}$. The UW magneto-optic system was set-up and operated by Anatoly Polyanskii and Alex Pashitski. The key components are a high quality polarized light microscope with video camera, a low temperature (down to 8K) cryostat with magnetic field coil (up to 400 Gauss), a transparent view window, and the Bi-doped Yttrium-Iron-Garnet (YIG) indicator film with in-plane magnetization vector. The polarization vector of light transmitting through the film changes as a function of magnetic field, translating into a color change when viewed through the polarized light microscope. The indicator film must be in close contact with the surface of the sample (the sample must be finely polished and flat), as the polarization is an integration of the magnetic field through the thickness of the sample with a sensitivity bias towards the sample surface in contact with the indicator film. Samples were imaged near the 8K minimum temperature for best contrast.

Electromagnetic Results

Table 4-1: Misorientation angle, common axis and illustrative electromagnetic data for various bicrystals.

Sample Name	Misorientation Angle	Rotation Axis	$\frac{J_c(10mT)}{J_c(0mT)}$ (77K)	$J_c(A/cm^2)$ (0.4T,77K)	ρ_{nd} ($\Omega\mu m^2$)
KS4B3	5°	[1 0 0]	1.0	2640	-
KS4B2a,b	7°	[7 4 1]	0.5-0.95	4900	-
KS4B1a,b,c	11°	[13 3 $\bar{13}$]	0.3-0.5	1450	0.3-0.5
KS1B1a,b	14°	[24 3 5]	0.2	380	1.3
KS5B1a-e	38°	[15 $\bar{14}$ 1]	<0.01	<1	26-65

All the MOMT samples had T_c transitions starting at ~92K, with $T_c(R=0)$ ~89K. **Figure 4-7**, **Figure 4-8**, and **Table 4-1** illustrate the effect of the crystal misorientation on the GB transport current density (J_{gb}) in magnetic fields of up to 400mT at 77K. Samples from this point on will be addressed solely by their misorientation angle both for the sake of brevity and because the misorientation angle is believed to be the key structural influence on the electromagnetic properties. When samples have been subsectioned, they will be referred to by the misorientation angle and subsection letter. For example, sample KS1B1b, which has a misorientation angle/axis pair of 14°[24 3 5], is referred to simply as 14°b.

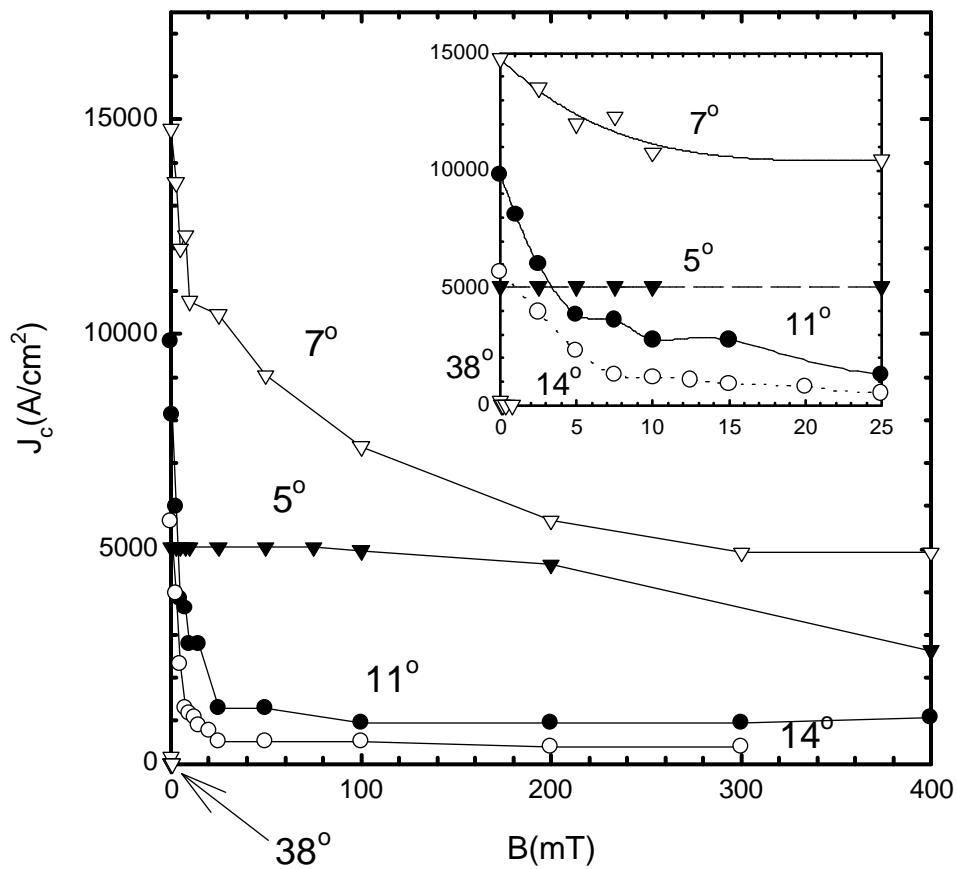


Figure 4-7) Plot of intergranular $J_c(B, 77K)$, determined by pulsed V-I measurements for MOMT samples of general misorientation of 5° through 38° . Inset shows details of the low field behavior.

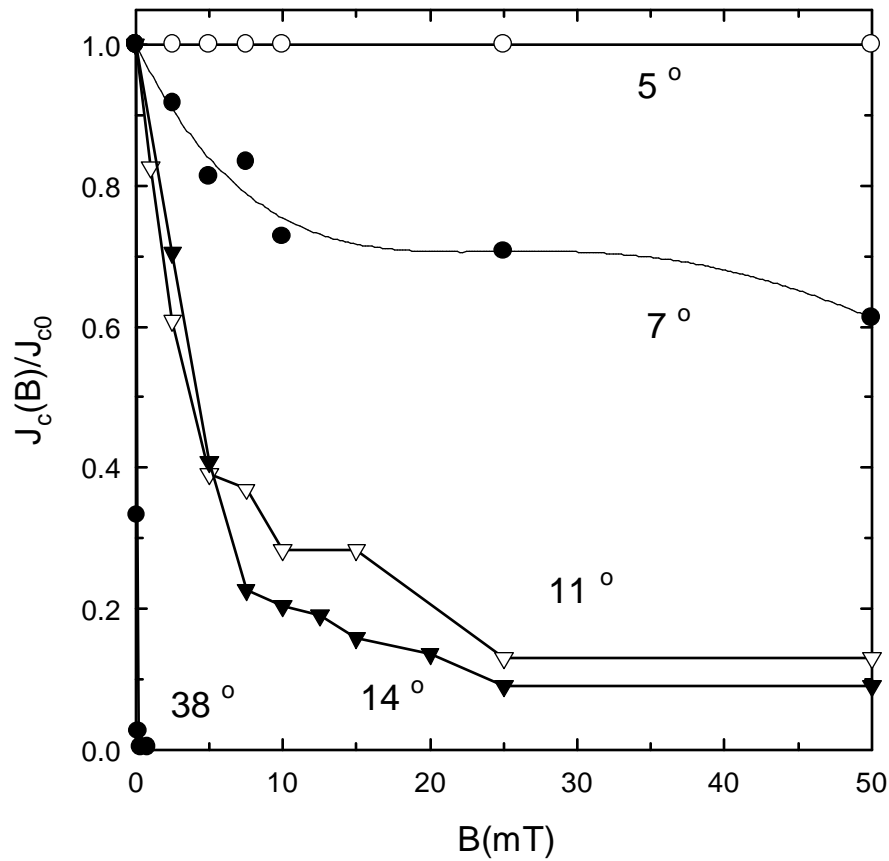


Figure 4-8) Plot of the intergranular critical current density in magnetic field, $J_{c(g.b.)}(B)$, expressed as a ratio of the zero field value at 77K for the samples of general misorientation (5° through 38°).

The magnetic field sensitivity $J_{c(g.b.)}(B)$ of the boundaries increases smoothly and progressively with increasing misorientation angle (θ), from the almost field-insensitive, 5° bicrystal, to the highly field-sensitive, 38° bicrystal (**Figure 4-7, Figure 4-8**). This latter bicrystal had an immeasurably low critical current above 1mT at 77K. As for $J_{c(g.b.)}(B=0T)$,

the zero field, GB critical current density, this decreased with increasing θ , from $>\sim 10^4 \text{ A/cm}^2$ at $\theta=7^\circ$ to $<\sim 10^2 \text{ A/cm}^2$ at 38° . Excepting the 5° bicrystal which had a lower than expected $J_{c(\text{g.b.})}$, perhaps due to microcracking, this decrease was also progressive.

As described in **Chapter 3**, the GB resistivity ρ_{nd} , derived from the ohmic portion of the V-I trace, is a useful normal state parameter for comparing JJ. This value increased dramatically from 0.3-0.5 $\Omega\mu\text{m}^2$ to 26-65 $\Omega\mu\text{m}^2$ as θ increased from 11° to 38° (**Table 4-1**). There was no ohmic behavior for the 5° and 7° bicrystals.

The electromagnetic data on the Boeing $38^\circ[3\ 1\ 1]$ bicrystal was not as extensive as the MOMT samples because above 0.1T the noise level became unacceptably high (tens of μV), although fair quality low field data was achieved. The sample had a T_c onset of 92K and $T_c(R=0)\sim 89\text{K}$. Compared to a MOMT sample of the same crystal misorientation, $38^\circ e[15\ -14\ 1]$, it does appear to have both a higher $J_{c(\text{g.b.})}(B=0)$ and a less sensitive field dependence (**Figure 4-9**). The ρ_{nd} is 1.7, about an order of magnitude less than the MOMT 38° sample.

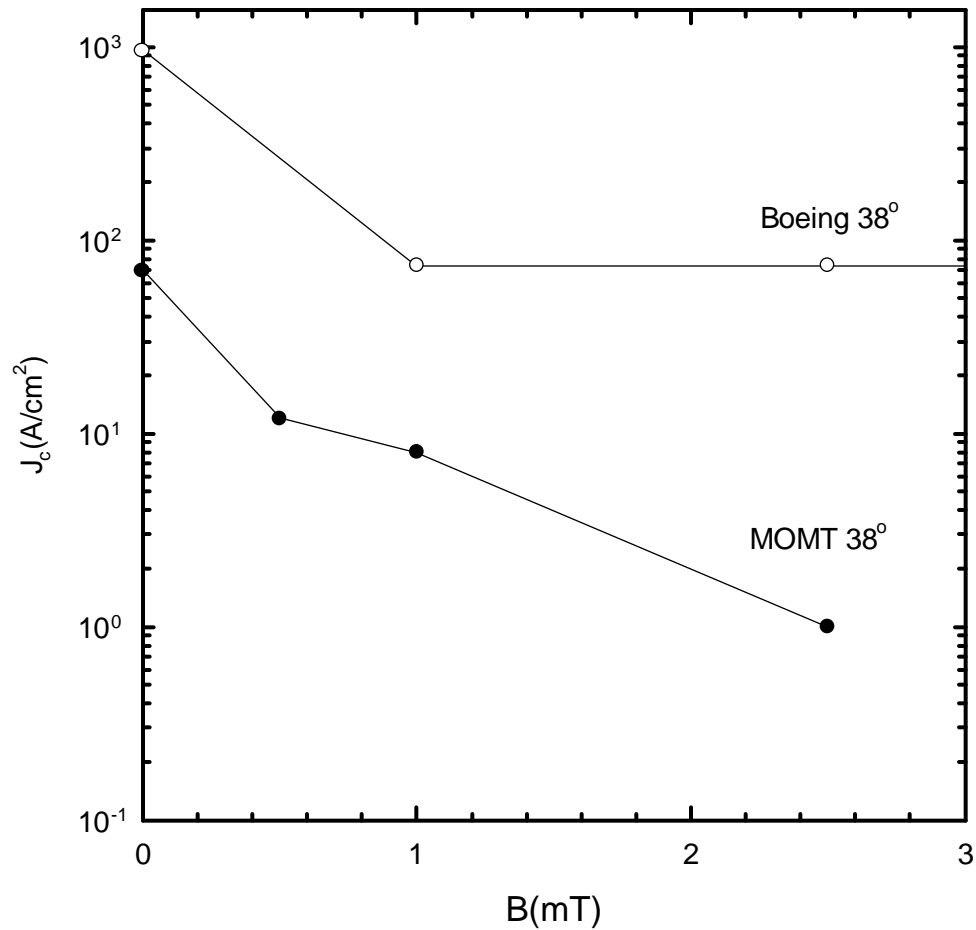


Figure 4-9) A comparison of the intergranular J_c of the $38^\circ[3\ 1\ 1]$ Boeing bicrystal and the $38^\circ e[15\ -14\ 1]$ MOMT bicrystal.

Representative V-J curves (V is plotted rather than the electric field, E, because E is much larger across the GB than in the grains for the higher angle GBs) are shown in **Figure 4-10-Figure 4-13**, for the 11° and 38° grain boundaries and their intragranular

regions. The characteristics shown in **Figure 4-10** and **Figure 4-11** for the 11° bicrystal exhibit a clear change from negative to positive curvature as the applied field is increased, with the change in sign of the curvature defining H^* . The sign change is clearer at lower voltages for the intergranular characteristics (**Figure 4-10**), because there is extra dissipation at higher voltages due to the ohmic component of the loss in the boundary. However, both the grain and the GB have similar $\mu_0 H^*$, ~5.2 T for the GB and ~4.6 T for the grain. **Figure 4-12** shows that the 38° GB has a strong ohmic component at higher V, although there is a marked non-linear characteristic at low voltages and small currents, which has a transition perhaps as high as 7.5T, and at least as high as 5T. For the two grains the corresponding transitions are around ~6.5T (**Figure 4-13**) to ~8.5T. **Table 4-2** summarizes the $\mu_0 H^*$ values measured on the 7°, 11° and 38° bicrystals. They range from ~4 to 8T and were essentially similar to the values obtained from the grains. We thus conclude that the two grains are communicating with each other through the GB and that, although the fraction of channel through which they were communicating is very small for the 38° GB, even this very high angle GB possesses some channels that are not degraded by strong magnetic fields.

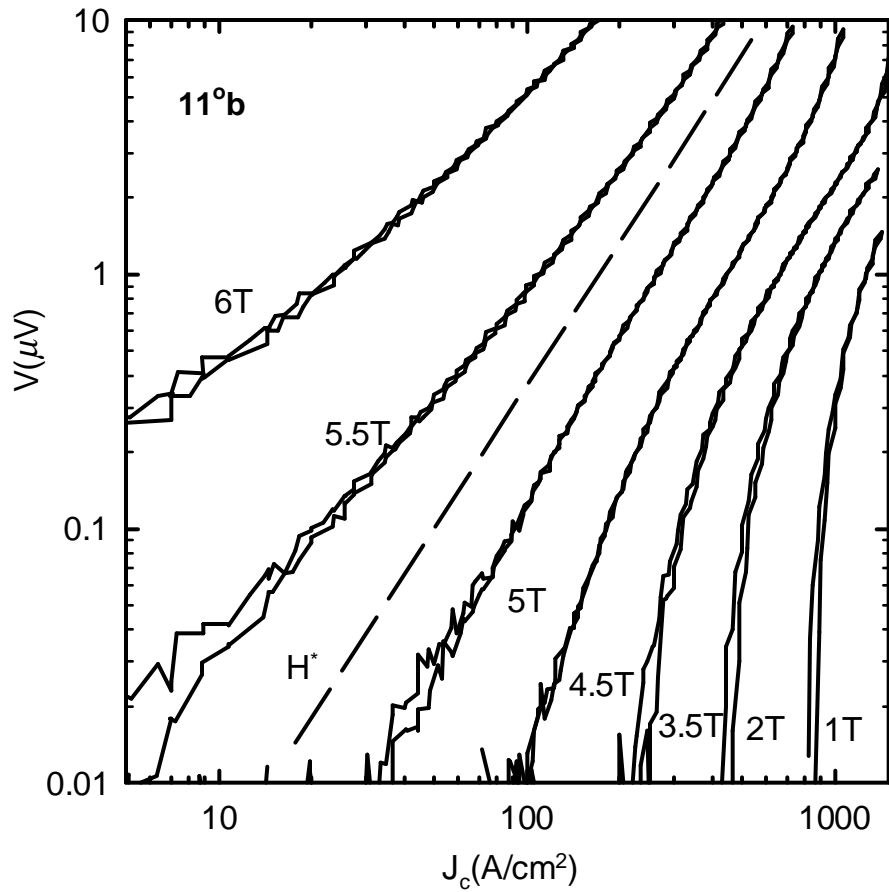


Figure 4-10) Plot of the intergranular log V - J characteristics for sample 11°b at 77K($H \sim ||c$).

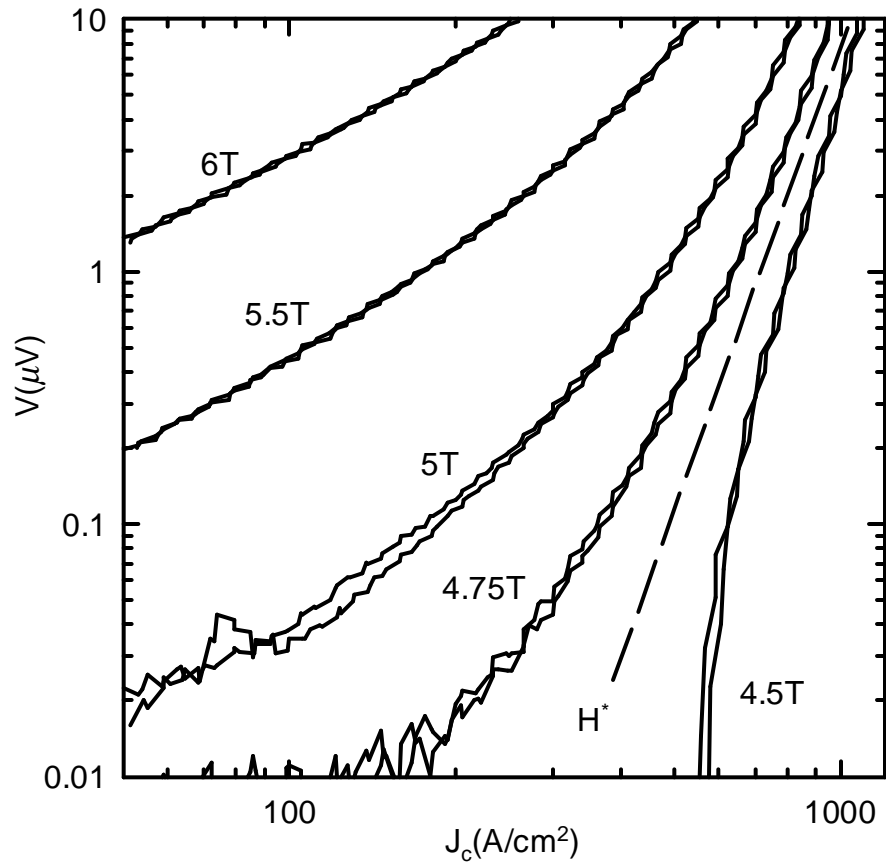


Figure 4-11) Plot of intragranular (grain B) log V-J characteristics for sample 11^b at 77K($H \sim \parallel c$).

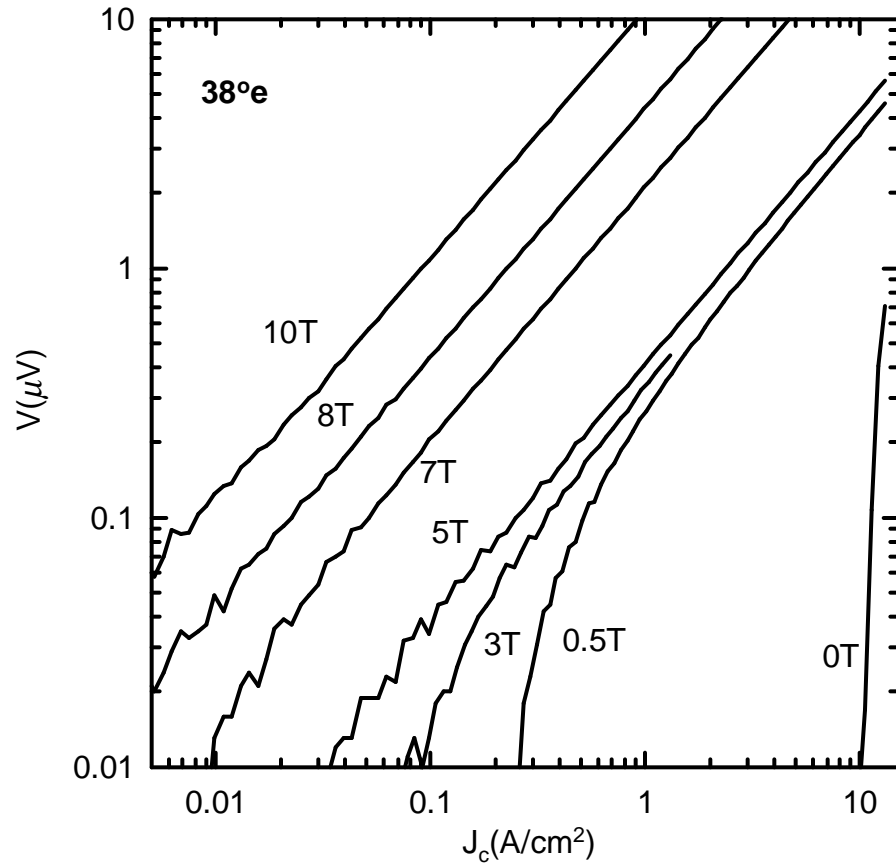


Figure 4-12) Plot of intergranular log V-J characteristics for sample 38°e at 77K.

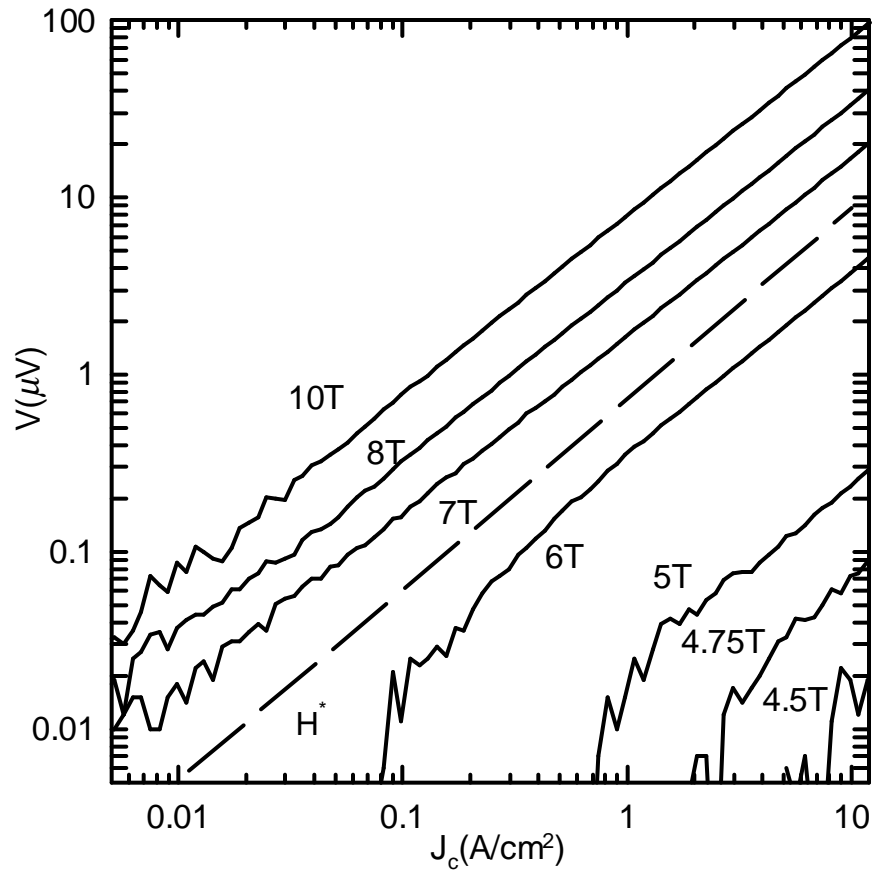


Figure 4-13) Plot of intragranular (grain B) log V-J characteristics for sample 38°e at 77K.

Table 4-2 Comparison of irreversibility fields of the grain boundary and the grains for various MOMT bicrystals at 77K.

Sample Name	Angle	$\mu_0 H^*$ intergrain	$\mu_0 H^*$ intragrain	Angle between c axes and B
KS4B2a	7°	3.75-4T	3-3.5T	~8,12°
KS4B2b	7°	4.5-4.75T	3-5T	~8,12°
KS4B1a	11°	4.5T-5T	5T-5.5T	~10,12°
KS1B1b	11°	5-5.5T	4.5-4.75T	~10,12°
KS5B1e	38°	>5T	6.5-8.5T	~20,55°

It is noted that the 38° sample has a higher H^* than the 7° or 11° samples, and that the two crystals of the 38° bicrystal have somewhat different H^* values. This is believed to be solely a consequence of the orientation of the c-axis of each crystal with respect to the magnetic field (**Table 4-2**). While the orientation of the c-axis with respect to the magnetic field is important for determining the quantitative value of H^* ($H_c^* \ll H_{ab}^*$), it does not affect the validity of our qualitative conclusions.

Magneto-Optical Imaging Experiments

Three melt-out melt textured bicrystals were magneto-optically (MO) imaged: 5°, 11°c, and 14°b. The 5° sample was electromagnetically characterized as strongly-coupled (**Figure 4-8**), and MO imaging provides visual confirmation. In **Figure 4-14**, the polarized light micrograph highlighting the GB is to the left of a MO image taken at 15K in 40mT of applied field. White corresponds to flux penetration and black to flux exclusion. The MO image shows no preferential flux penetration at the GB, although there was considerable flux penetration along ab plane cracks (the c-axes of both crystals are ~9° from the plane of the samples top surface) and the larger 211 particles.

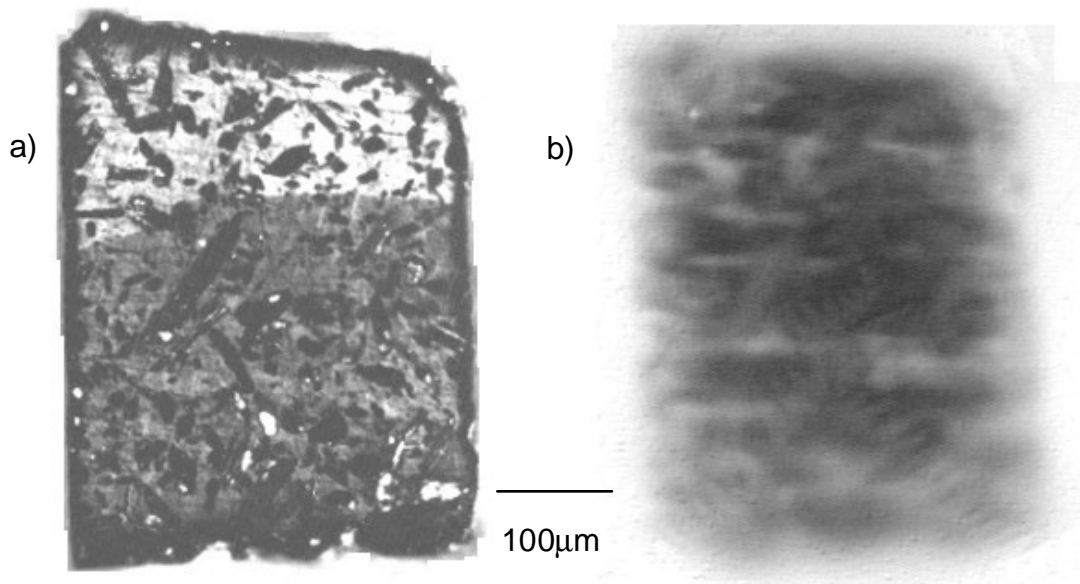


Figure 4-14) a) Polarized light micrograph of the 5° bicrystal b) reflected light MO image at 15K in 40mT. The c-axis of each grain is ~9° from surface plane. Flux penetrates preferentially along cracks between platelets and at large 211 particles but not at the GB

The 11° samples had electromagnetically mixed strong and weak coupling (**Figure 4-8, Figure 4-21**). In (**Figure 4-15**) the polarized light micrograph of sample 11°c is placed alongside a MO image taken at 15K and zero field, after field cooling in 40mT. White regions are areas where flux is pinned, and dark regions are flux-free. The MO image does show that flux had penetrated and escaped preferentially at the GB, consistent with the initially strong field dependence of J_c seen in **Figure 4-8**. However, there do appear to be strong pinning bridges near points A, B and C.

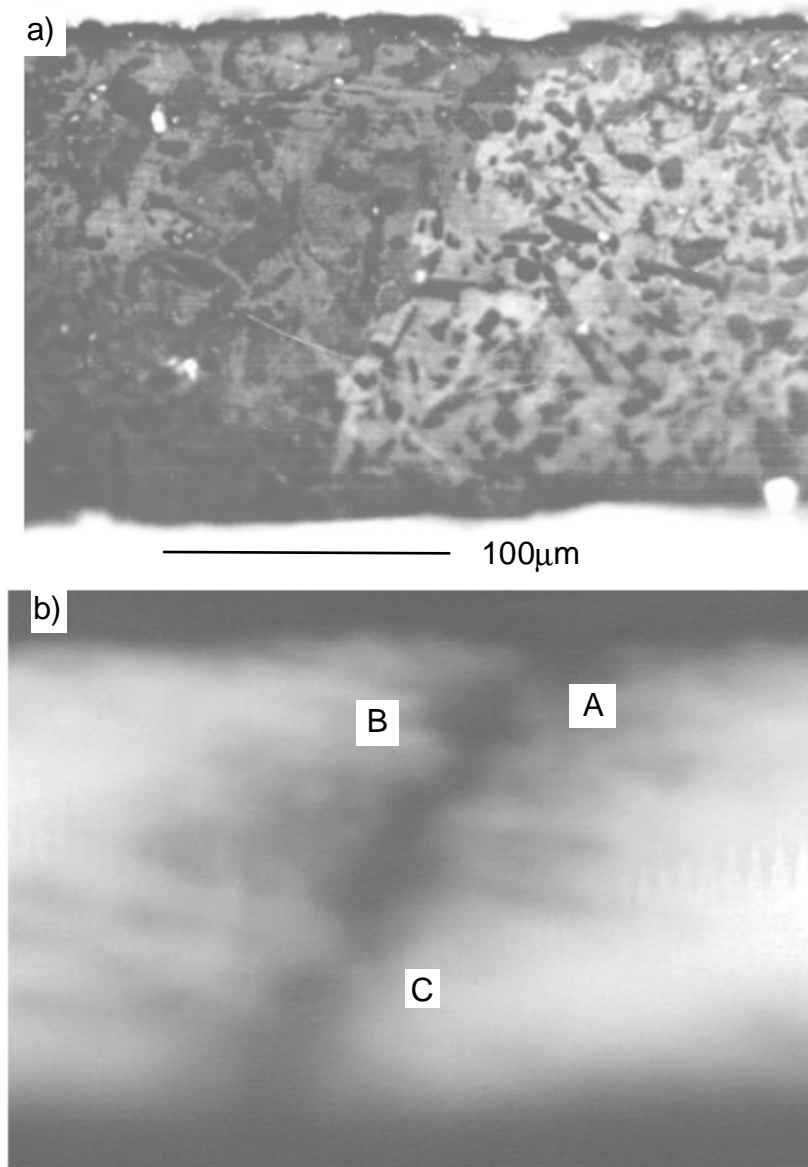


Figure 4-15) Polarized light micrograph of the 11°C bicrystal b) reflected light MO image at 15K in zero field after field cooling in 40mT. Regions A, B, and C pin flux better than adjacent segments of the boundary

The 14b° sample also exhibited electromagnetically mixed strong and weak coupling (**Figure 4-8**). The plots in **Figure 4-17** are the smoothed pulsed current V-I

traces for this sample, and they exhibit clear signs of parallel weakly and strongly coupled components, the strongly coupled component being the minority component with the field-independent trace. In **Figure 4-16**, the polarized light micrograph of 14°b is adjacent to the MO image of 14°b that was field cooled in 400mT to 8K. Darker represent areas of higher flux concentration. The MO image shows that flux preferentially entered the boundary except for a bridge ~15 μ m wide which resisted flux entry in a manner similar to that of the intragranular regions. However, this strong pinning bridge does not appear to be a related to any specific macroscopic feature of the GB.

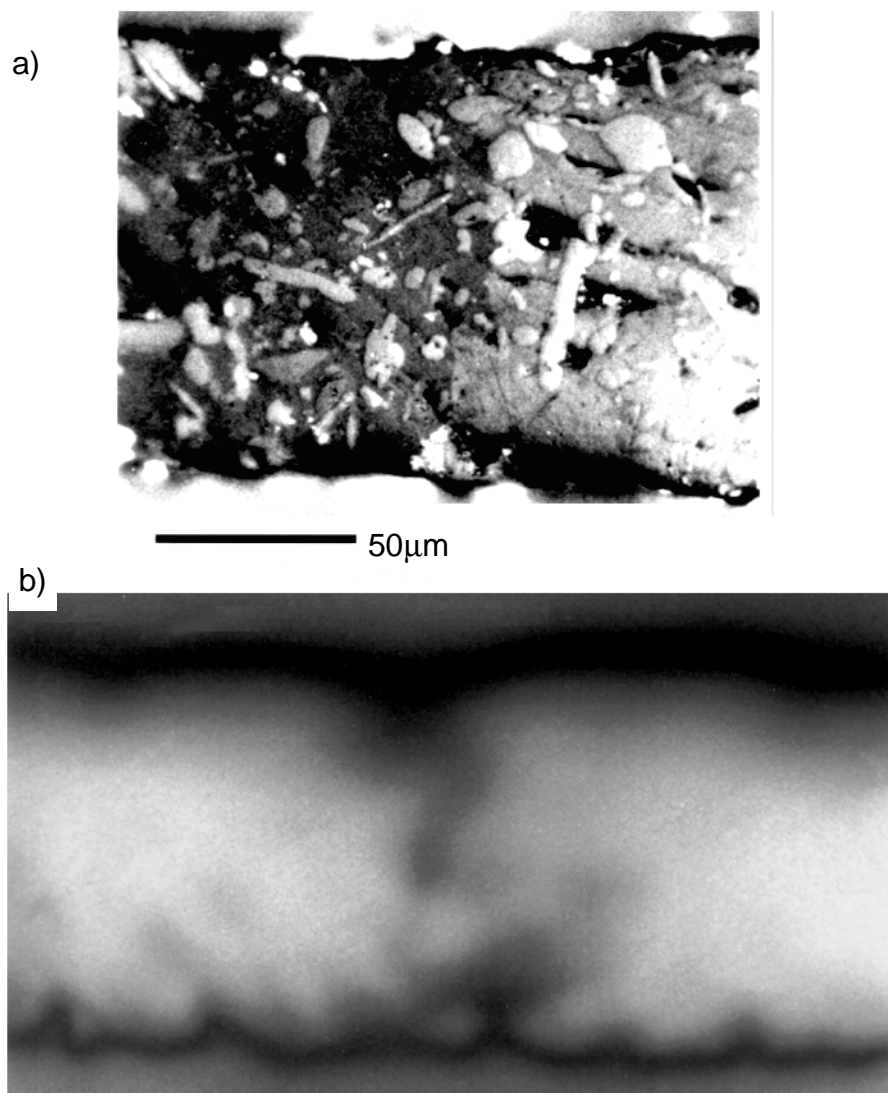


Figure 4-16) a) Polarized light micrograph of the GB in sample 14°b. b) Magneto-optic image of the same region. The image was taken after being field cooled to 8K in 40mT.

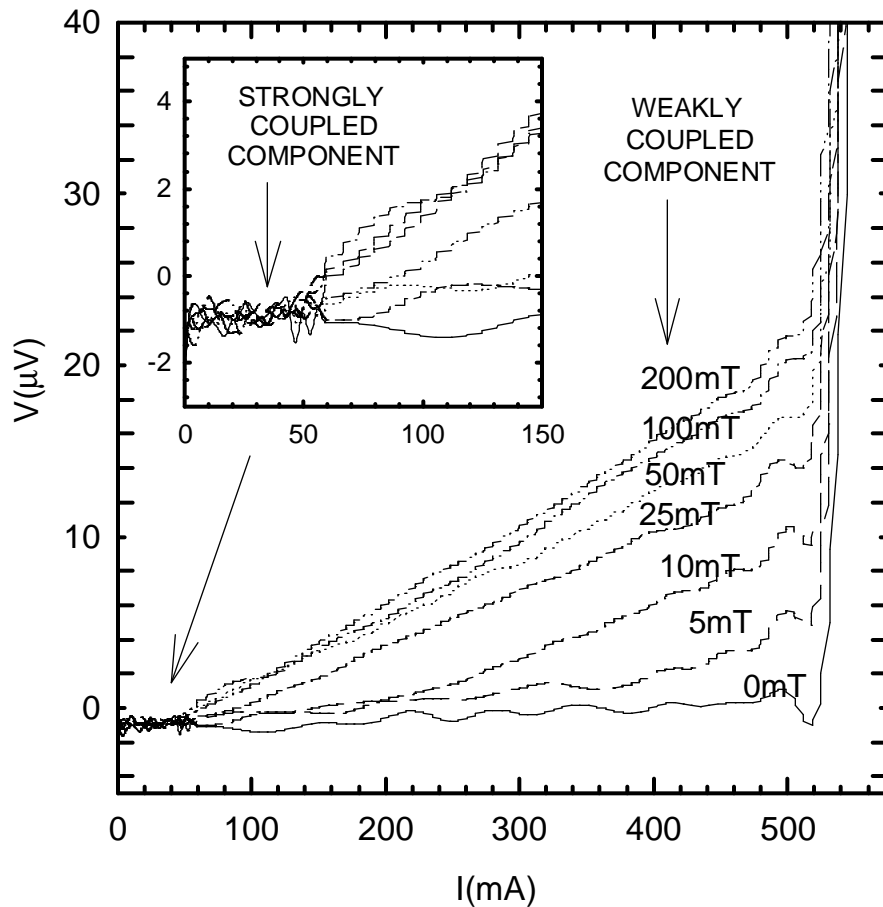


Figure 4-17) Smoothed data from pulsed V-I traces on 14°b as a function of magnetic field. There is a sharp decline in the I_c in low magnetic fields, but the inset highlights a far less field-dependent I_c .

These MO images are consistent with an increase in electromagnetic coupling inhomogeneity as the misorientation angle increases. They also suggest that macroscopic regions of this inhomogeneity can be imaged. It is not clear whether these bridges are

macroscopically homogeneous or whether they contain a higher density of much smaller, strongly coupled bridges than the relatively weaker segments of the boundary. It should also be noted that MO images are most sensitive to the surface layer, thus the through-thickness behavior is not clear from the images.

Results - Role of the Macroscopic Grain Boundary Plane

The influence of the macroscopic GB plane was specifically investigated for the 7°, 11° and 38° bicrystals. The 7° bicrystal had a slowly curving and a step-like portion to the boundary. It was laser cut into two sub-samples 7°a and 7°b, 7°a having the smoothly varying boundary and 7°b having the step-like boundary (**Figure 4-18**). The normalized $J_{c(g.b.)}/J_{c(\text{grain})}$ behavior of the step-like boundary 7°b is a little more field dependent than 7°a at low fields but the behavior is very similar above ~100mT (**Figure 4-19**).

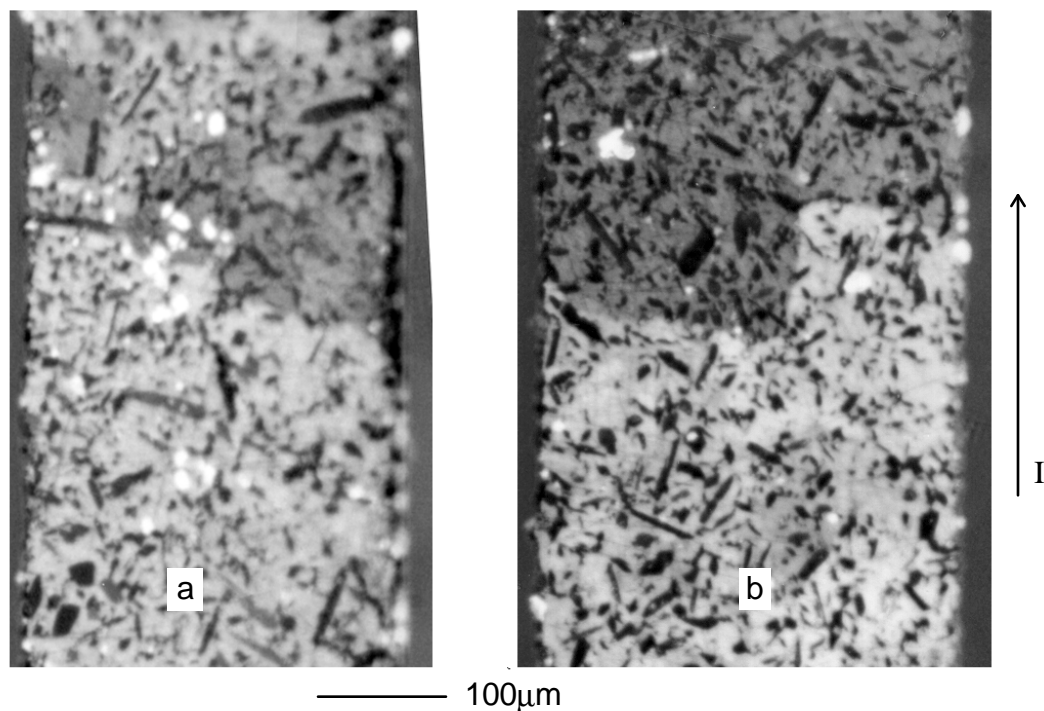


Figure 4-18) Polarized light micrographs of sample 7°a and 7°b. The grain boundary in 7°a is curved while the GB in 7°b has two ~90° kinks. Applied current direction is along the long sample dimension as indicated.

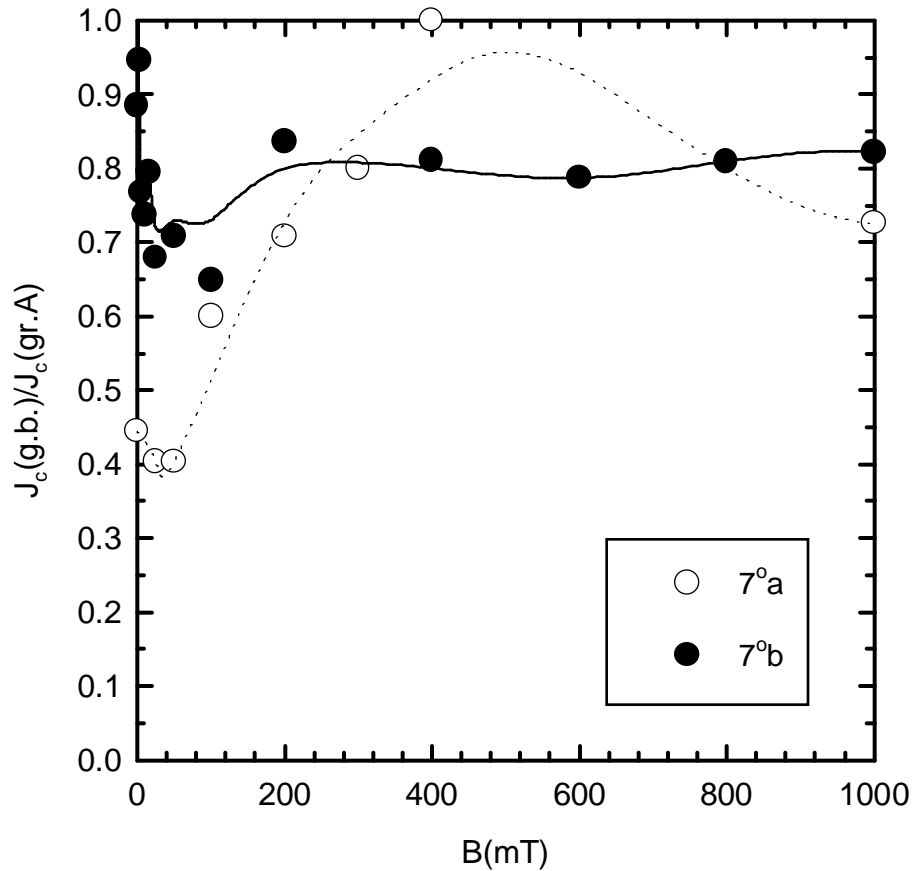


Figure 4-19 A plot of the ratio of the intergranular $J_c(B)$ vs. the lower intragranular $J_c(B)$ for samples 7°a and 7°b at 77K.

The 11° bicrystal, which had a smoothly curved GB, was subdivided into 3 sub-samples: 11°a, 11°b, and 11°c. Bicrystals 11°a and 11°b had similar GB planes, which were inclined at $\sim 45^\circ$ to the direction of current flow (**Figure 4-20a**, **Figure 4-20b**), while the boundary plane in 11°c was nearly normal to the direction of current flow (**Figure 4-**

20c). The GB plane in these 3 sub-samples was essentially parallel to the surface normal. $J_{c(g.b.)}(B)$ of all three sub-samples were very similar, $J_{c(g.b.)}$ exhibiting a decline of ~70-85% in fields of ~20mT (**Figure 4-21**). Starting from a zero field value of $\sim 10^4$ A/cm², all sub-samples exhibited a similar residual supercurrent of $1-2 \times 10^3$ A/cm², which was independent of field in the measured range of 20 to 400mT.

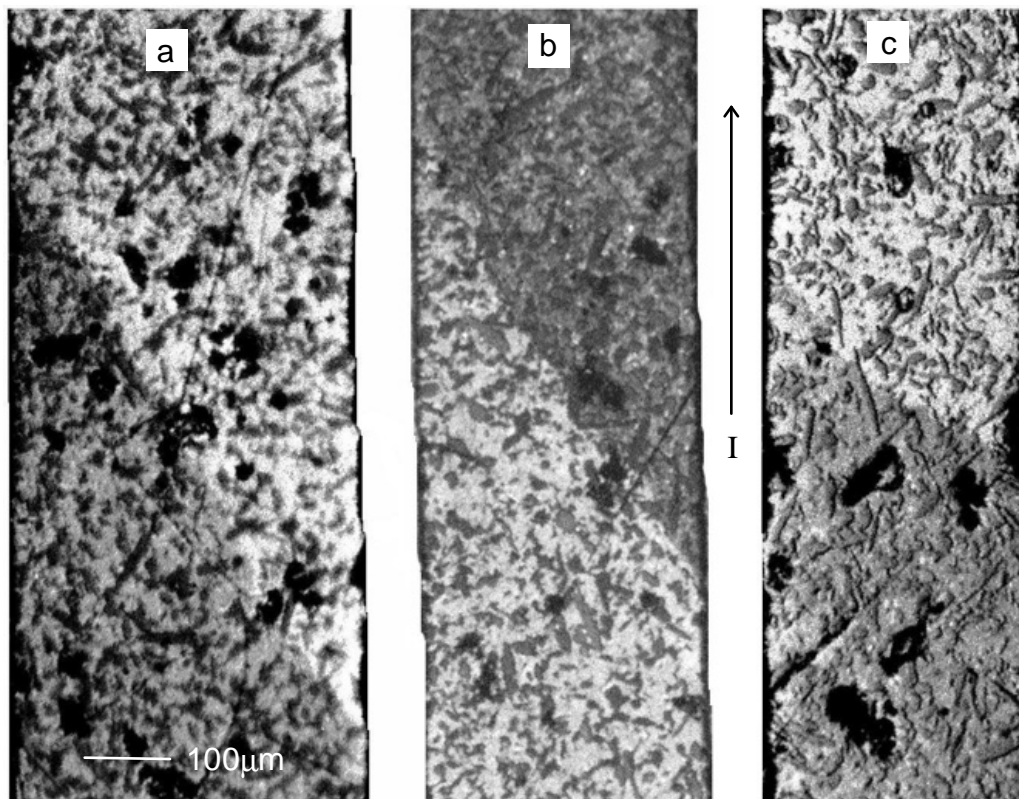


Figure 4-20) Polarized light micrographs of samples 11°a, b, and c. The boundary planes in 11°a and 11°b have similar inclinations to the samples' long axis, while 11°c is nearly normal to the long axis. Applied current direction is along the long sample dimension as indicated.

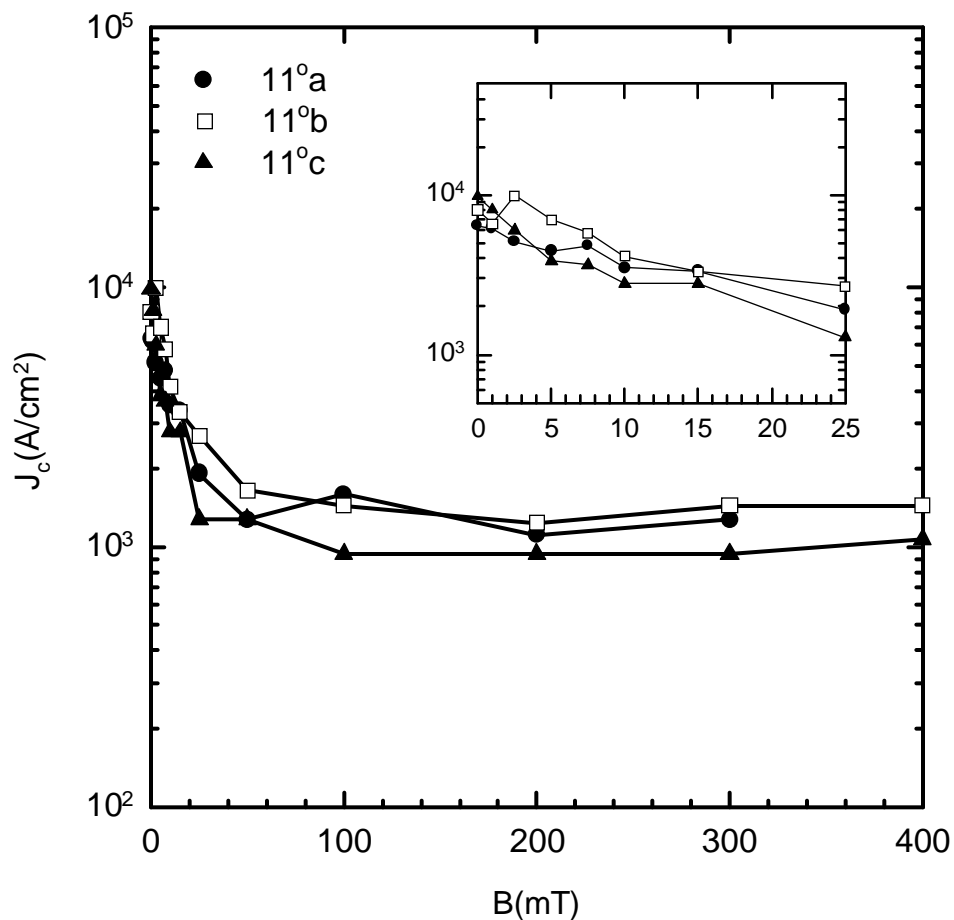


Figure 4-21) Plot of the $J_c(B, 77K)$ characteristic for samples 11°a, b, c.

The 38° bicrystal was sectioned into 5 sub-samples, 38°a through e. Samples 38°a-d were polished to $\sim 85\mu\text{m}$ thickness and laser cut as were the previous samples. Sample 38°e was kept as a massive sample which was as wide as the sum of 38°a-d ($\sim 1.5\text{mm}$) and was 0.5mm thick. The much larger 38°e sample had a sufficiently large enough $I_c(H)$ that it was possible to measure extended V-J curves at high fields. Sample

38°b cracked and was not measured; the other sub-samples had the boundary inclinations indicated in **Figure 4-22**. Four sub-samples were measured (38°a, c, d and e). Their $J_{c(g.b.)}(77K, 0mT)$ values were strongly depressed to $\sim 60-150A/cm^2$, as compared to the $5,000-10,000A/cm^2$ of the smaller misorientation bicrystals. Weak fields of even 1mT depressed the $J_{g.b.}$ of all sub-samples to below $0.1A/cm^2$.

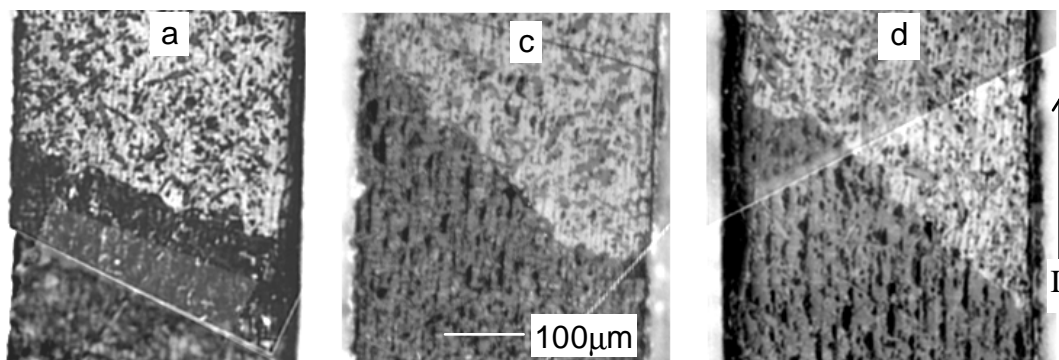


Figure 4-22) Polarized light micrographs of samples 38°a, c, d showing the different grain boundary plane inclinations. Current direction is along the long sample dimension.

In summary, we found that macroscopic boundary plane effects were small for 7°, 11° and 38° bicrystals and, where present, not obviously distinguishable from small effects introduced by the different self-fields of different samples. It is also noted that the effect of the macroscopic grain boundary plane is dwarfed by the effect of the general misorientation angle. This is not in contradiction to the magneto-optic results, which do show inhomogeneity of the GB plane, but at the $10\mu m$ size scale or below. The

macroscopic grain boundary plane experiment could not probe variations at this fine of a size scale.

Discussion

Taken as a whole, the data presented shows that the transition from strongly-coupled to weakly-coupled for bulk scale, melt-textured YBCO bicrystals of general misorientation is neither abrupt nor complete as one progresses from a low (5°) to high angle (38°) grain boundary. The characteristics taken into account in judging the electromagnetic character of the GB are the magnitude of the zero field critical current density, the field-dependence of the critical current density, and whether or not the extended V-J characteristics show a low-voltage, vortex-glass-like transition comparable to that seen within the grains. By these criteria it is clear that the 5° bicrystal is fully coupled. There is a distinct and progressive increase in the field dependent J_c (77 K) as θ increases, culminating in the extreme field dependence of the very high angle bicrystal (38°), but even this GB showed evidence of the irreversibility field transition at the same magnetic field as the intragranular regions. Thus it appears that a small, but nevertheless finite, strongly coupled section of GB remains, even at very high angles.

Systematic information about the misorientation dependence of the properties of GBs has come mainly from thin films grown on bicrystal substrates. In the original thin film GB misorientation studies [14,139,140], [001] tilt boundaries in YBCO showed a rapid fall in the ratio $J_{c(\text{g.b.})}/J_{c(\text{grain})}$ as θ increased beyond 5° . Indeed, even a 5° [001] tilt boundary exhibited asymmetric I-V curves and extreme field sensitivity, indicating that it was weakly

coupled. In the limit of low θ , [001] tilt GBs can be described as heterogeneous interfaces containing lattice dislocations which run from top to bottom of the film and lie parallel to each other in the GB. The dislocations are separated by channels of comparatively undisturbed lattice. Thus it is natural to explain the transition from strong to weak coupling of [001] tilt GBs in terms of the narrowing of the undistorted channel with increasing θ , either because the dislocation cores[14] or their strain fields overlap[15]. Implicit in this model is the idea that the dislocation core is not superconducting and that supercurrent is confined to the channels between the cores, or to proximity coupled regions adjacent to the dislocation cores. In the limit of $\theta < 3\text{-}5^\circ$, this model is quite plausible because it associates the strongly coupled electromagnetic properties to the comparatively undisturbed channels that lie between the dislocation cores.

To explain the electromagnetic properties at higher angles, this basic model can be generalized, as is schematically illustrated in **Figure 4-23**. The simple dislocation-core model is shown in **Figure 4-23a** for both open (left) and closed (right) configurations [14]. When the dislocations or their strain fields overlap, the boundary becomes weakly coupled since the cores are normal or insulating. The ohmic nature of the higher voltage portions of the V-J curves in **Figure 4-10** and **Figure 4-12** argue that the cores are normal. The second scheme is a modification of the first in that the coupling strength of the weakly coupled GB lying beyond the overlap misorientation is itself spatially modulated. Sarnelli et al. [141] proposed that the residual supercurrents observed at high fields in higher angle thin film GBs were characteristic of transport through a set of parallel Dayem bridges (Josephson-coupled regions separated by normal barriers) (**Figure 4-23b**). A third, more

general possibility is that high angle GBs of general misorientation still contain a few strongly coupled paths[142, 143, 128, 37, 144] (**Figure 4-23c**), even though the majority of the GB is weak-linked. Potential sources of the strongly coupled paths might be infrequent structural units that are strongly coupled regions of matched lattice between widely spaced dislocations, or symmetric facets with no hole depletion across them[145]. This model can rationalize the rapid fall off of J_c in low fields as being due to field-induced destruction of the majority, proximity-coupled part of the GB, while the higher field, residual supercurrent occurs by transport through the (minority) strongly coupled regions. At what misorientation angle, and for what type of bicrystal, any of these models are accurate is subject to debate. The Dimos et al. data are consistent with a transition near 5° [13] to 10° [14], while the more recent and complete data set of Heinig et al. [146] suggests that the channels [14,15] close between 10 and 15° . Differences between the two studies may be at least partially ascribed to differences in the growth conditions of the films and the influence that this has on the effective dislocation core size. Consistent with the higher angle transition of Heinig et al.[146], Babcock et al.[4] found strong coupled behavior in a 14° [001] tilt, bulk YBCO bicrystal and Cai et al.[147] found that $H^*(GB) \sim H^*(grain)$ up to at least 18° [001] tilt, also finding the large GB resistance at higher voltages similar to that seen in **Figure 4-12** for the 38° bicrystal. Suhara et al.[148] found the transition from strong to weak coupling to be between 10° and 15° for Tl-1223 and Tl-2212 thin films. Thus it seems clear that the channel model seems to be a good basis for understanding the

crossover from strong to weak coupling, at least for [001] tilt bicrystals, but also that the exact position of the crossover is sample- and perhaps material-dependent.

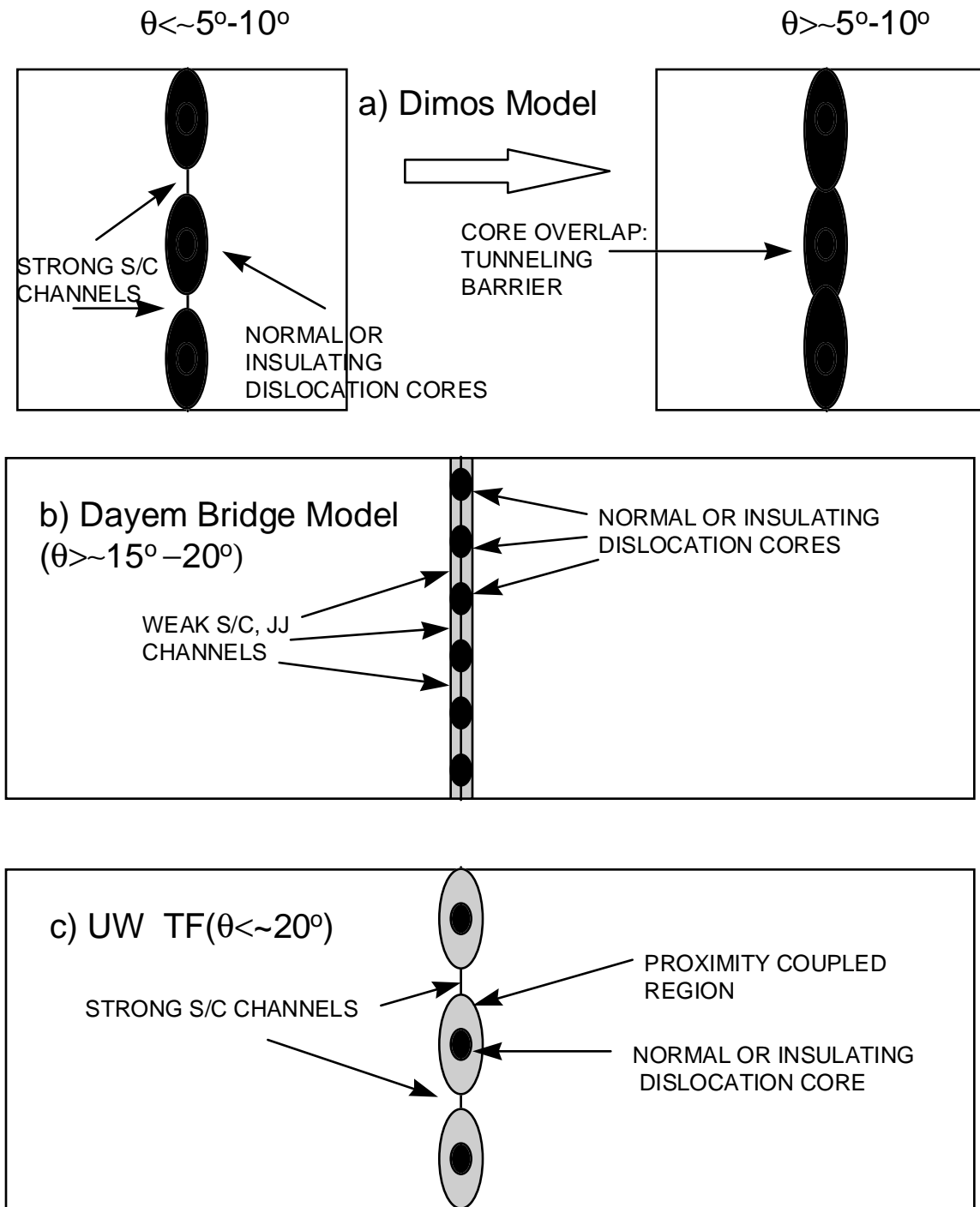


Figure 4-23) Schematic drawings of three models for explaining the GB J_c in thin film [001] tilt YBCO as a function of GB structure: a) The dislocation core model [14,15], before and after core overlap, b) The Dayem bridge model[141], and c) Two channel model[42,146].

One source of the strongly coupled regions within the GBs is suggested by the recent analysis of dislocation structure of [001] tilt flux grown bicrystals by Tsu et al.[149], which shows that dislocations are neither uniformly spaced, nor of one type and that macroscopically straight grain boundaries facet on the scale of tens of nanometers. Such boundaries have variable width channels, thus naturally leading to residual, high field supercurrents being present at higher angles than would occur for equally spaced dislocations. In the melt-textured, general (or “mixed”) misorientation bicrystals, we have an even more complicated situation. Whereas [001] tilt boundaries in principle have only one set of dislocations, a mixed misorientation GB has at least three intersecting sets of dislocations. This changes the shape of the strongly coupled channels in the GB plane from extended rectilinear objects sandwiched between parallel dislocation sets (**Figure 4-24a**) to point-like contacts in mixed misorientation grain boundaries[150] (**Figure 4-24b**). The mixed misorientation sketch is based on recent electron microscopy studies of low angle MOMT GBs by Miranova et al.[150] (the dislocation cores are black, the associated strain field is gray, and undisturbed lattice is white). The provocative result of the present work is that such mixed misorientation boundaries still show evidence of strongly coupled paths, in spite of the much smaller areas of “strong” channel that are expected from the model. The evidence for this conclusion lies both in the electromagnetic results and from the magneto-optic imaging on the 5° , 11° and 14° boundaries, which provided visual evidence of strongly coupled channels across the GB. Perhaps the combination of macroscopic and microscopic faceting allows for a large number of possible dislocation spacings, of which some may allow small, strongly-coupled gaps.

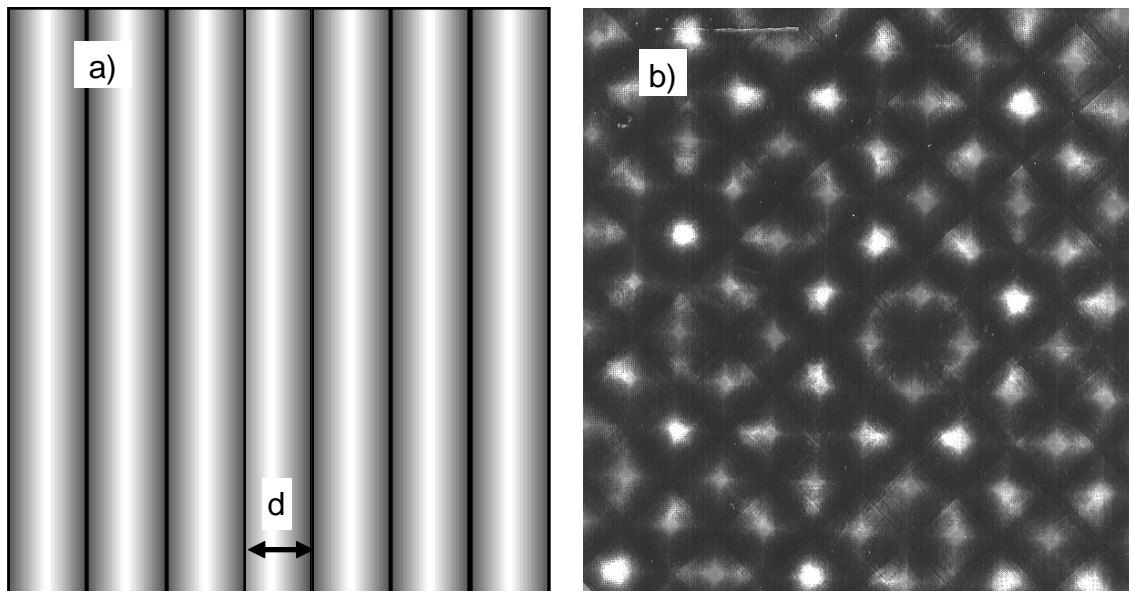


Figure 4-24) Schematic representations of the possible microstructure viewed in the GB plane (GB normal is out of the paper) of a) the prison bar model of a simple [001] tilt boundary. The black regions are the dislocation cores, the gray are the areas near the cores that are degraded due to strain, while the white areas represent undisturbed lattice. Note the large 2-D rectangular regions of this undisturbed lattice. b) General misorientation GB, composed of a grid of 4 sets of dislocations, results in a geometrical network of essentially point, rather than line contacts (adapted from Miranova et al.[150]).

Figure 4-25 is a plot of the $J_{c(g,b.)}(\theta, B=0)$ values for the mixed misorientation, melt-textured, samples described in my work[22,33,151], as well as values for flux-grown[20,152], seeded melt-textured[93], and thin film YBCO bicrystals[146,153] found in the literature. It is clear that the intragranular regions of thin film bicrystals have far higher $J_{c(g,b.)}(\theta, B=0)$ values than bulk melt-textured or flux-grown bicrystals, but that the drop off of $J_{c(g,b.)}(\theta, B=0)$ is significantly sharper for the thin films. So different are the angular dependence of the two classes that the absolute $J_{c(g,b.)}$ values crossover at $\sim 35^\circ$. In

contrast, the bulk $J_{c(g.b.)}(\theta, B=0)$ values are rather flat out to $\sim 10^\circ$ and a very gradual drop-off of $J_{c(g.b.)}(\theta, B=0)$ despite the far more complicated misorientations (and hence dislocation structure) of many of the bulk scale bicrystals!

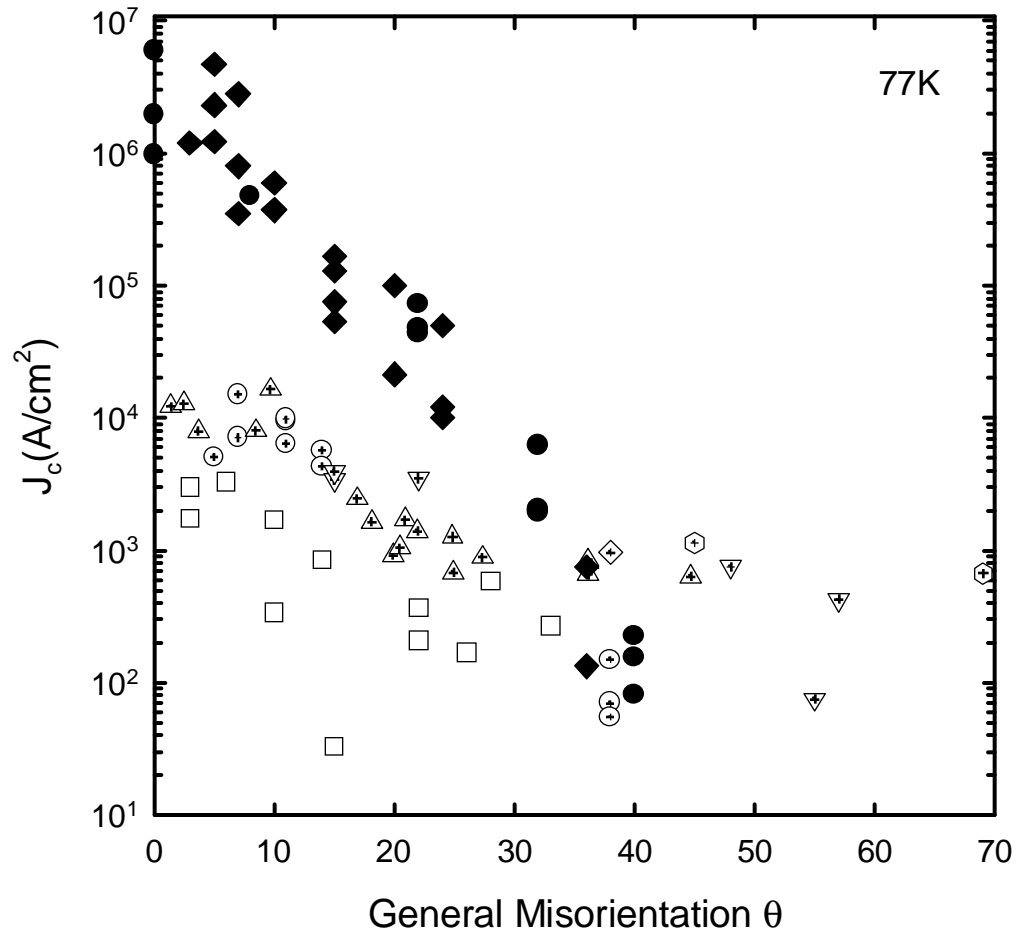


Figure 4-25) Plot of the $J_{c(g.b.)}(B=0, 77K)$ values for flux-grown (\square [20,152]), melt-textured (UW/AT&T MT - \oplus [22], MOMT - \odot [33], UW MT - ∇ [22], Boeing seeded - \diamond [151], Argonne seeded - \triangle [93]) and thin film (Ivanov et al. - \bullet [153], Heinig et al. - \blacklozenge [146]) bicrystals, as a function of general misorientation angle.

I have plotted in **Figure 4-26** the ratio of the intergranular (from **Figure 4-25**) to intragranular $J_c(B=0)$ of the previous bulk and thin film bicrystals in the manner of Dimos et al.[14]. For many samples, both the inter- and intragranular J_c values were measured (the solid white and black symbols). In other samples, the intragranular regions were too small to measure by transport and had to be estimated based on well established intragranular values of similar samples (the symbols with white crosshairs). For melt-textured samples, the estimated intragranular $J_c(0T, 77K)$ was $2.5 \times 10^4 A/cm^2$ (this is generally accurate to within a factor of 2). For [001] tilt flux-grown bicrystals[152], the intragranular $J_c(0T, 77K)$ was estimated at $4000 A/cm^2$ [4]. Plotting the data as a ratio re-emphasizes the disparity of zero field boundary behavior as a function of misorientation between the bulk scale and thin film samples. For example, at 30° , the J_c ratio of bulk bicrystal boundaries has fallen by $\sim 1-2$ orders of magnitude, but for thin film boundaries it has fallen by 3 orders of magnitude. However, one must use caution in interpreting zero field GB critical current densities since they may be sensitive to self-field effects and to extrinsic factors, such as cracks, which are common in bulk samples.

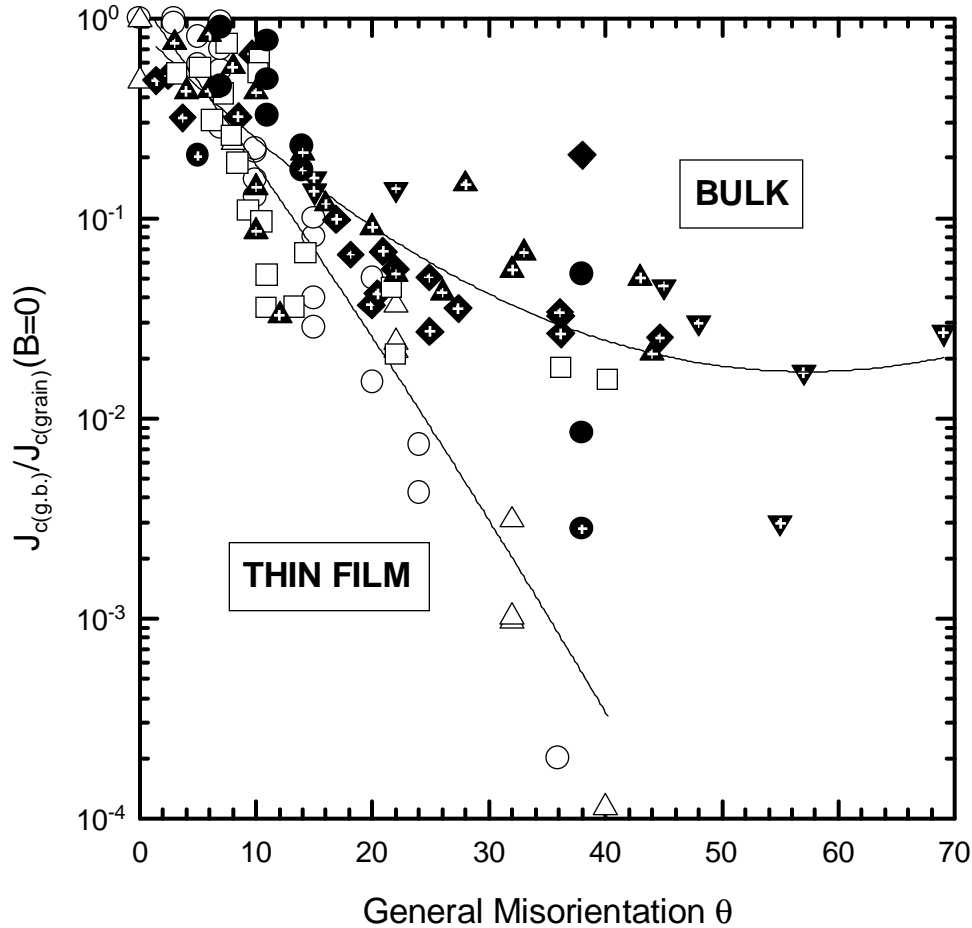


Figure 4-26) Plot of the ratio of the intergranular to intragranular critical currents ($0T, 77K$) for melt-out samples (\bullet, \odot), in comparison to other general misorientation, UW melt-textured samples previously measured at $77K$ (∇)[22], (\blacklozenge)[151], Argonne seeded melt-textured bicrystals (\blacklozenge)[93], UW/NIST $[001]$ tilt bulk flux-grown bicrystals at $77K$ (\blacktriangle)[20,152], thin film samples of mixed misorientation at $5K$ (\square) by Dimos et al.[14], $[001]$ tilt thin film samples at $77K$ (\circ) by Heinig et al.[146], and $[001]$ tilt thin film samples at $77K$ (\triangle) by Ivanov et al.[153]. Symbols with white crosses indicate that the intragranular J_c was estimated, while all other samples had measured intragranular J_c values. Second order regression fits to all the bulk scale and thin film data illustrate that bulk scale grain boundaries tend to have a weaker decline of $J_{c(g.b.)}$ with increasing misorientation angle than the thin film boundaries.

An important issue not always considered in studies of the misorientation dependence of the J_c is the field-dependence of the properties. An example of the fact that the zero field and in-field properties are not the same is illustrated in the four plots of **Figure 4-27**. Transport data for bicrystal 7°a were taken inside both grains, as well as across the boundary for the conditions where B was both $\sim\parallel c$ and $\sim\perp c$. Considering the whole $J_{c(g.b.)}(B)$ characteristic gives a more complete picture of the electromagnetic role of the GB. When data is plotted as $J_{c(g.b.)}(B)/J_{c(\text{grain})}(B)$ in **Figure 4-27b** and **d**, a line with zero slope indicates strong coupling, a steep negative slope indicates weak coupling, and a positive slope indicates that the intragranular J_c is declining more rapidly than the intergranular J_c . The vertical axes in **Figure 4-27b** and **d** define the effectiveness of the boundary in passing supercurrent. About 40% of the weaker grain's supercurrent is transported across the boundary in zero field, but this fraction increases sharply to ~ 1 for fields $\sim\perp c$ up to 1T, before settling at ~ 0.7 from 2T to 8T (**Figure 4-27b**). Thus there does appear to be a proximity-coupled component to the supercurrent transport at low fields, indicating some weak link behavior to the GB. However, the boundary does not act as a weak link at 1T, and is only a minor impediment at higher fields. For $H\sim\parallel c$, there is also a strong weak link effect in low field ($<20\text{mT}$), $I_{c(g.b.)}/I_{c(\text{grain})}$ decreasing from about 0.7 to 0.3 before rebounding to ~ 0.8 and then decreasing to zero at H^* (**Figure 4-27d**). Plotting the data in this manner shows that, despite some low magnetic field sensitivity, this 7° boundary is not a severe impediment to the high field critical current. This result may help to explain the recent good transport J_c values ($\sim 2.5 \times 10^3 \text{ A/cm}^2$, 77K) in high magnetic fields (0-3T) found in magnetically aligned YBCO thick films[29], whose grains are believed to

be generally misorientated by $\sim 10^\circ$ [31]. The result is also consistent with the recent study of Wang et al. on a BSCCO-2212 8° [001] tilt bicrystal[154]. When tested at fields up to H^* , they both showed that the GB could transmit large fractions ($\sim 75\%$) of the intragranular current. Therefore it seems desirable to consider the magnetic field-dependent properties of grain boundaries and not just the self field properties in considering the full character of grain boundaries and their influence on the transport current

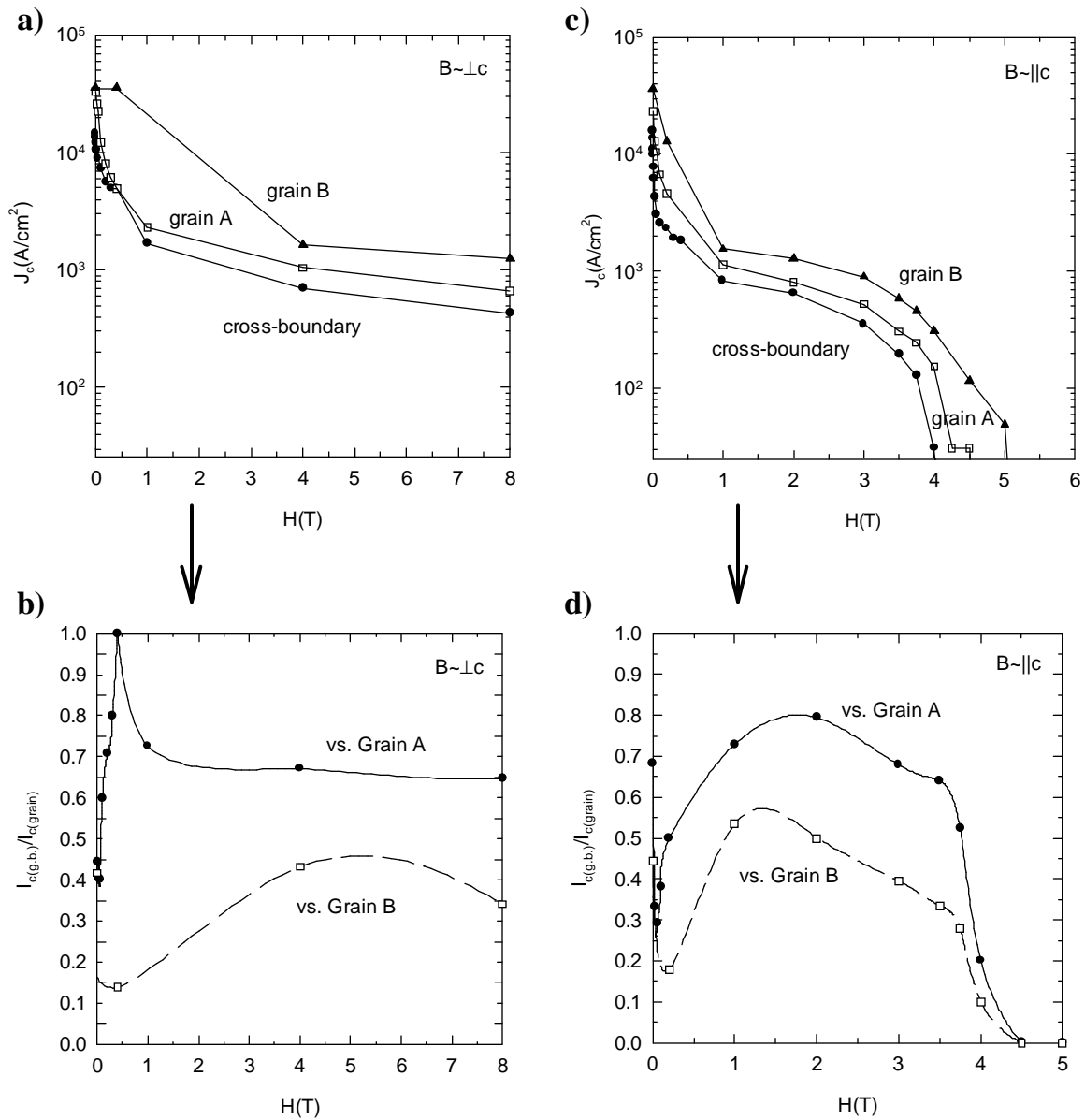


Figure 4-27) Plots of the ratios of the intergranular to intragranular critical currents as a function of applied magnetic field at 77K: a) $J_c(B)$ for the inter and intragranular regions of sample 7°a with $B \sim \perp c$, b) The ratio of intergranular I_c to intragranular I_c with $B \sim \perp c$, c) $J_c(B)$ for the inter and intragranular regions of sample 7°a with $B \sim \parallel c$, d) The ratio of intergranular I_c to intragranular I_c with $B \sim \parallel c$.

Chapter 5 : Summary and Conclusions

The fundamental conclusion of this thesis is that the transition from strong to weak coupling in bulk scale, melt-processed YBCO is neither abrupt nor complete as a function of increasing general misorientation. My original, conventional voltage level data on high angle boundaries (15° - 69°) already suggested that there was a smooth transition from strong to weak coupling and that strongly-coupled paths (at least at 4K), existed for all high angle boundaries. My more recent high sensitivity transport data show more clearly that both transition angle ($\theta=7^{\circ}$ - 11°) and high angle ($\theta=38^{\circ}$) grain boundaries have minority, strongly coupled paths, even at 77K. The residual critical current seen at high magnetic fields appears to have a flux-pinning nature, as evidenced by the observation that the irreversibility line measured across the grain boundary is about the same as in the grains. This observation is bolstered by magneto-optic imaging, which was used to directly observe inhomogeneous coupling on a scale of $\sim 10\mu\text{m}$ in the 11° and 14° GBs.

The effect of the *macroscopic* grain boundary plane on the overall electromagnetic character of a melt-out melt-textured grain boundary was found to be minimal, supporting my initial assumption that the crystal misorientation angle is the key parameter of the full grain boundary misorientation description for determining superconducting properties. The results of the magneto-optic imaging and the subsection of the grain boundary plane experiments are not necessarily contradictory, as these two experiments investigate

different size scales. The macroscopic grain boundary plane experiment probed the grain boundary plane on the scale of several hundred microns, more than an order of magnitude greater than the features seen in the magneto-optic images. It is also worth noting that the stronger coupled regions in the magneto-optic image do not require that the material is homogeneously strongly-coupled (this would be incompatible with any dislocation model of the grain boundary), but rather that it has a higher density of strongly-coupled elements than the other regions of the grain boundary.

The angular dependence of the ratio of inter- to intra-granular critical current for melt-textured bicrystals was found to be similar to that in bulk scale flux-grown bicrystals but less severe than in thin film bicrystals. However, this ratio depends on the applied field, becoming larger in higher fields ($\sim > 1\text{T}$), thus showing that the GB weakens less than the grain under increasing field.

Finally, it is interesting to ascertain whether the bulk or TF bicrystals serve as a better model for the grain boundaries in the extremely promising Ion-Beam Aided Deposition (IBAD) tapes. It is unclear whether the IBAD grain boundaries should be considered thin film or bulk in nature, as the tapes are deposited via a thin film technique but have thicknesses more usually associated with the bulk (some IBAD tapes are as thick as $9\mu\text{m}$). Although IBAD tapes cannot be tested as bicrystals, we can correlate their J_c properties with bicrystal data by correlating J_c to the FWHM of the (103) pole figure. This pole figure has components of both c and ab pole misorientation, and so is analogous to a general misorientation angle. Using a summary of IBAD data from Freyhardt et al.[155], and estimating the intragranular J_c to be $2 \times 10^6 \text{A/cm}^2$ (a reasonable value obtained from

intragranular regions of TF YBCO[152]), a collection of intergranular vs. intragranular J_c ratios can be obtained. This data can be compared to experiments on TF bicrystals (**Figure 5-1**) and bulk scale bicrystals (**Figure 5-2**). Although it is clear from very recent experiments of my colleague A. Pashitiski[156] that the current path in IBAD tapes is controlled by percolation, still, it is interesting to note that the IBAD data follows well the data for bulk scale bicrystals for essentially the entire angular range. Therefore, future studies of bulk scale bicrystals (MT or FG) may have special relevance to the attempts to refine and improve IBAD tapes.

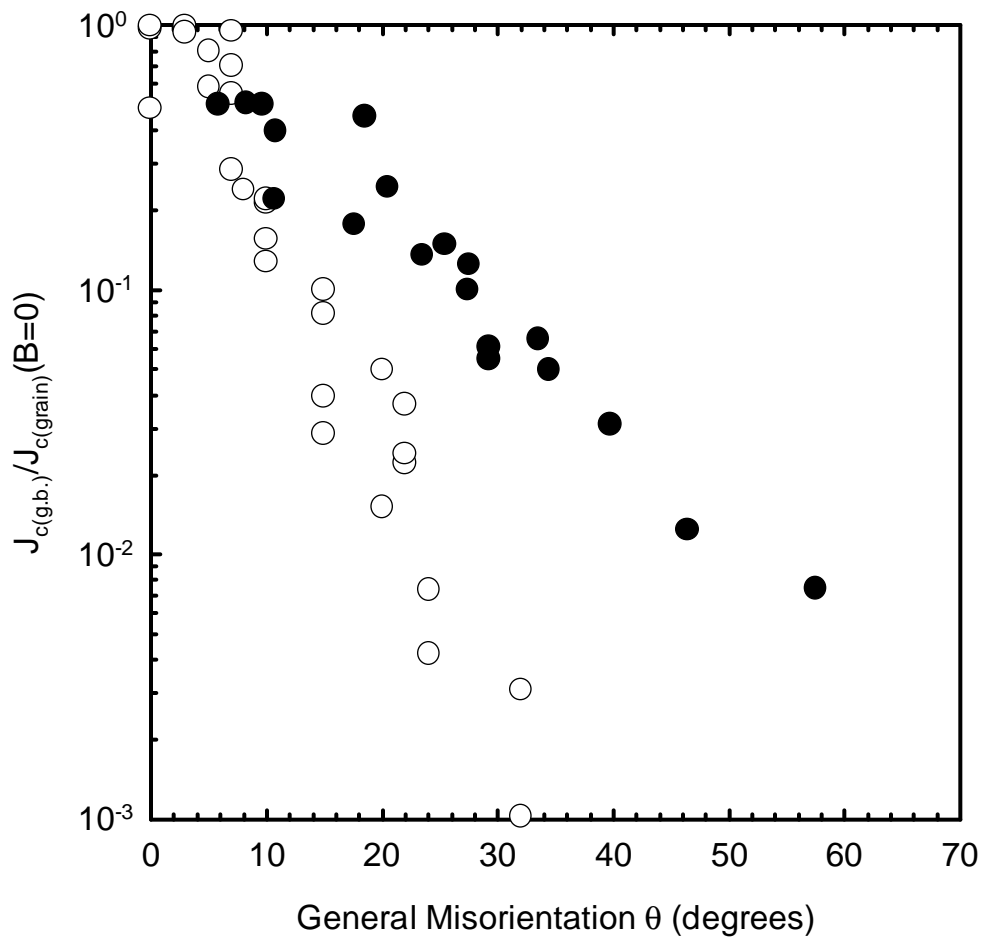


Figure 5-1) Plot of the estimated $J_{c(g.b.)}/J_{c(grain)}(77K)$ ratios at zero field for IBAD tapes (●)[155] vs. thin film (TF) bicrystals (○)[146,153]. The intragranular J_c value for IBAD tapes is estimated at $2 \times 10^6 \text{ A/cm}^2$, a standard YBCO TF value[152]. The IBAD ratios are consistently higher than the TF ratios above 10° .

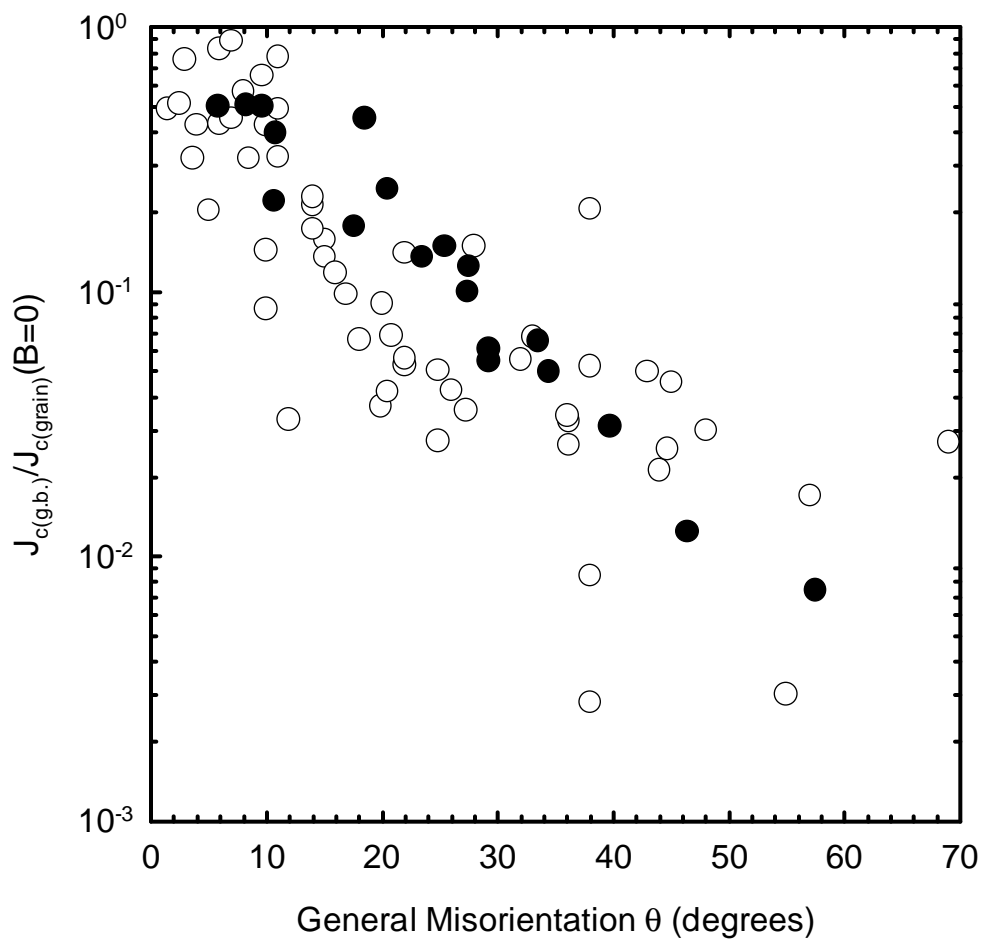


Figure 5-2) Plot of the estimated $J_{c(g.b.)}/J_{c(grain)}(77K)$ ratios at zero field for IBAD tapes (\bullet) vs. bulk bicrystals (\circ , flux grown[20,152] and melt-textured[22,151,93]). The IBAD ratios lie among the bulk bicrystal ratios.

In summary:

- Melt-textured bulk scale bicrystals have been successfully isolated and characterized in detail.
- The change from strong to weak coupling as a function of misorientation angle is neither abrupt nor complete. There exists a transition region, $\sim 7^\circ$ - 20° , that contains significant fractions of both weak and strong coupling.
- Evidence has been provided to support the concept that the high field residual current is due to minority, strongly coupled components of the grain boundary.
- Melt-textured bulk scale bicrystals have shown to be possible models for the misorientation dependence of IBAD tapes.

Appendix A: The Mixed Misorientation Description

The Mixed Misorientation Description - General Grain Boundary Geometry

There are five macroscopic degrees of freedom associated with a complete description of the misorientation of the two grains and the boundary that form a general bicrystal.[131] There are two basic schemes for describing these five degrees of freedom; the interface-plane scheme, which describe the misorientation in terms of the lattice planes at the grain boundary, and the misorientation scheme, which describes it on the basis of the two crystallographic lattice orientations. The basis of this appendix is the latter, more common scheme. Of the five degrees of freedom needed to describe the grain boundary, two degrees describe the boundary plane normal \mathbf{n} (two independent direction cosines), two describe the rotation axis \mathbf{u} (two independent direction cosines) and one is needed to describe the rotation angle that sets both crystals coincident (**Figure A-1**).

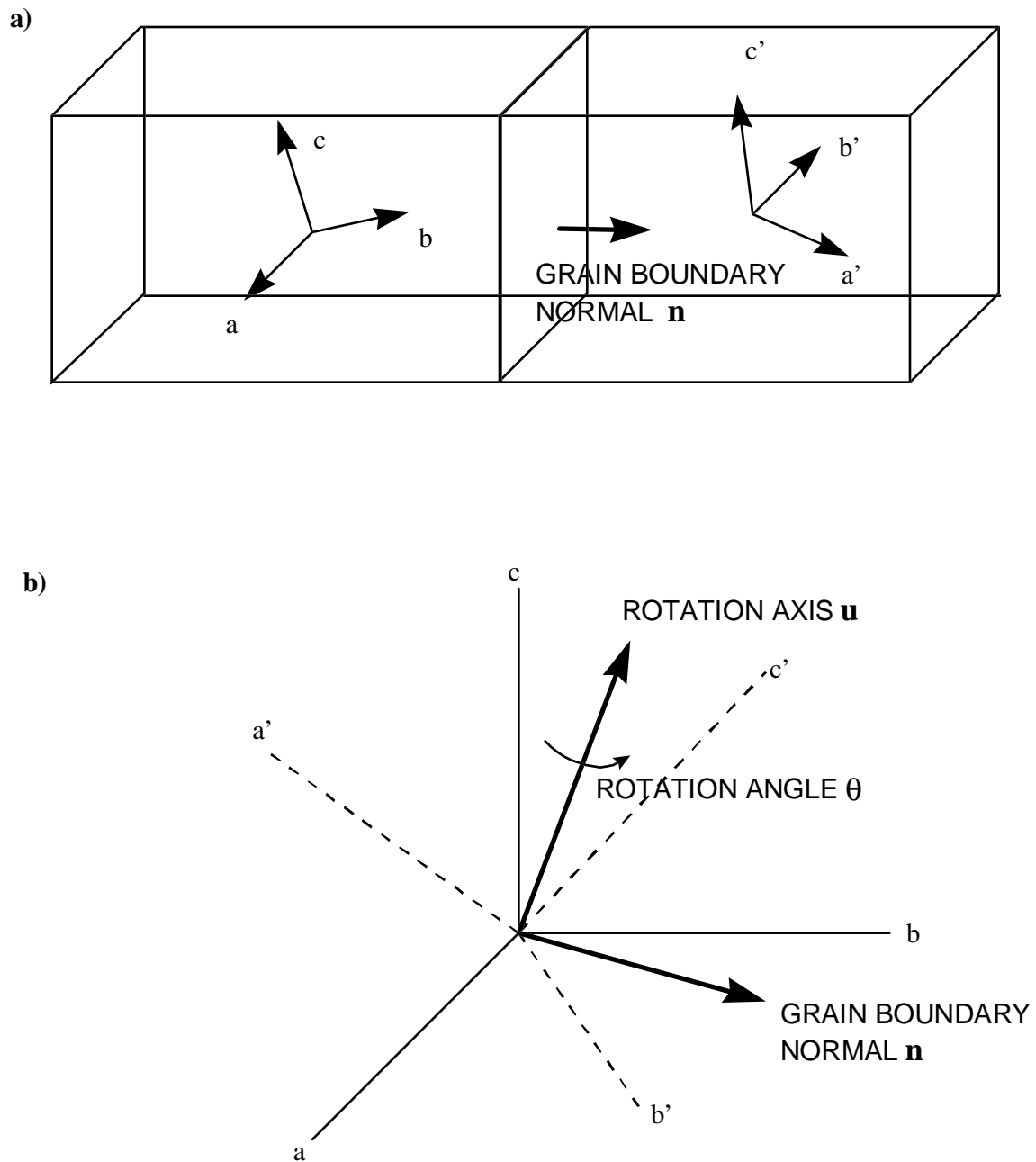


Figure A-1) a) Schematic drawing of a general misorientation grain boundary with a flat grain boundary plane. b) The misorientation between crystal abc and $a'b'c'$ in a) can be described by a rotation angle θ about a rotation axis \underline{u} that sets both crystal coincident. The grain boundary normal \underline{n} is independent of θ and \underline{u} .

There are two popular ways of describing the crystallographic misorientation - by a one angle/axis pair method, or by three Euler angles. The one angle/axis pair description of grain boundary misorientation was originally promoted by Lange[131], and it is presently the preferred description in the crystallography and microscopy communities. The complete description is the rotation angle θ about the rotation axis $[UVW]$ with the grain boundary normal \mathbf{n} . The values for the rotation angle and axis are derived from the misorientation matrix, \mathbf{M} , which is obtained from experimentally determined data of the misorientation between low index poles of the two crystals. The elements of the misorientation matrix are direction cosines between the low index poles of one crystal with the low index poles of the other crystal, i.e. a 3 x 3 matrix of direction cosines:

$$\mathbf{M} = \begin{bmatrix} \cos \theta_{aa'} & \cos \theta_{ab'} & \cos \theta_{ac'} \\ \cos \theta_{ba'} & \cos \theta_{bb'} & \cos \theta_{bc'} \\ \cos \theta_{ca'} & \cos \theta_{cb'} & \cos \theta_{cc'} \end{bmatrix}$$

where the axes of crystal 1 are a, b, c and crystal 2 a', b', c'

The axis of misorientation (UVW) and the angle of misorientation (θ) about this axis can be extracted from the matrix by the following formulae:

$$\cos \theta = (\cos \theta_{aa'} + \cos \theta_{bb'} + \cos \theta_{cc'} - 1) / 2$$

$$U:V:W = \cos \theta_{cb'} - \cos \theta_{bc'} : \cos \theta_{ac'} - \cos \theta_{ca'} : \cos \theta_{ba'} - \cos \theta_{ab'}$$

$$(\text{if } \theta=180^\circ, U:V:W = (a_{11} + 1)^{\frac{1}{2}}:(a_{22} + 1)^{\frac{1}{2}}:(a_{33} + 1)^{\frac{1}{2}})$$

For misorientations about low index poles, twist and tilt terms can be used to further describe the boundary (**Figure A-2**). A twist boundary is one in which the grain boundary plane normal is parallel to the rotation axis. A tilt boundary is one in which the grain boundary plane is orthogonal to the rotation axis. If we describe the rotation angle as θ , the angle between the rotation axis \mathbf{u} and the grain boundary normal \mathbf{n} as α , then the twist angle (ϕ) and tilt angle (ω) can be described as such:

$$\sin \frac{\phi}{2} = \frac{\sin \frac{\theta}{2}}{\sqrt{(1 + \tan^2 \alpha \cos^2 \frac{\theta}{2})}}$$

$$\sin \frac{\omega}{2} = \sin \alpha \sin \frac{\theta}{2}$$

It should be stressed that this decomposition into twist and tilt angle components cannot be done if \mathbf{n} is not precisely defined and constant for the boundary area under analysis.

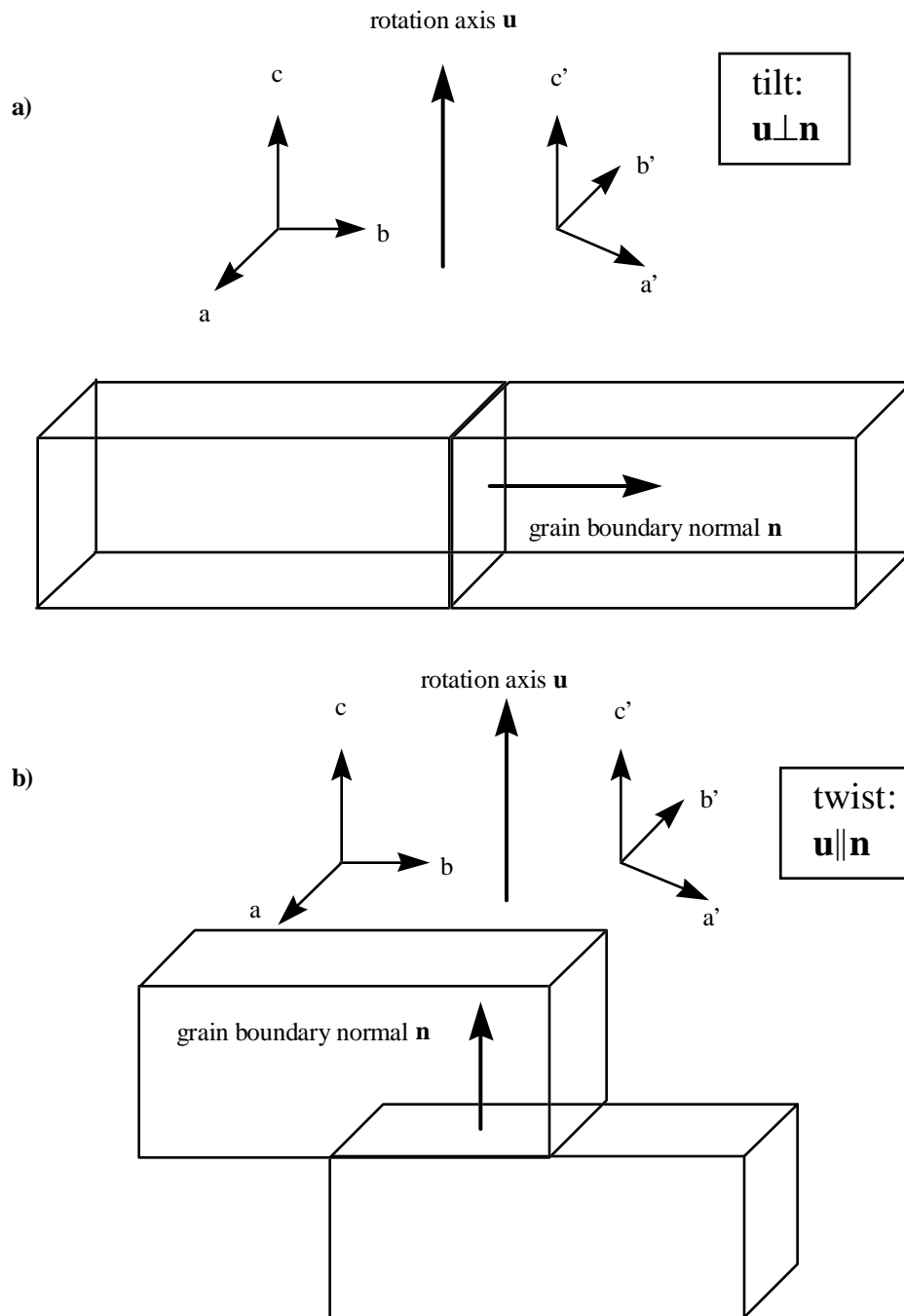


Figure A-2) a) Drawing of a tilt grain boundary: the rotation axis is perpendicular to the grain boundary plane normal ($\mathbf{u} \perp \mathbf{n}$). b) Drawing of a twist grain boundary: the rotation axis is parallel to the grain boundary plane normal ($\mathbf{u} \parallel \mathbf{n}$).

The Euler angles description is preferred in the physics community.[157] Any misorientation may be described by three consecutive rotations about three orthogonal axes. There are many different choices of rotations allowed, but a popular convention used in mechanics and solid state physics is illustrated in **Figure A-3**. The first rotation is Ψ about z , the second Θ about x'' , and the last is Φ about z' . This results in the following relation to the measured misorientation matrix M :

$$\mathbf{M} = \begin{bmatrix} \cos \theta_{aa'} & \cos \theta_{ab'} & \cos \theta_{ac'} \\ \cos \theta_{ba'} & \cos \theta_{bb'} & \cos \theta_{bc'} \\ \cos \theta_{ca'} & \cos \theta_{cb'} & \cos \theta_{cc'} \end{bmatrix} =$$

$$\begin{bmatrix} \cos \Psi \cos \Phi - \sin \Phi \sin \Psi \cos \Theta & \cos \Psi \sin \Phi + \cos \Theta \cos \Phi \sin \Psi & \sin \Psi \sin \Theta \\ -\cos \Phi \sin \Psi - \cos \Theta \sin \Phi \cos \Psi & -\sin \Psi \sin \Phi + \cos \Theta \cos \Phi \cos \Psi & \cos \Psi \sin \Theta \\ \sin \Theta \sin \Phi & -\sin \Theta \cos \Phi & \cos \Theta \end{bmatrix}$$

Using the above relation, one can solve for the Euler angles Φ , Θ , and Ψ .

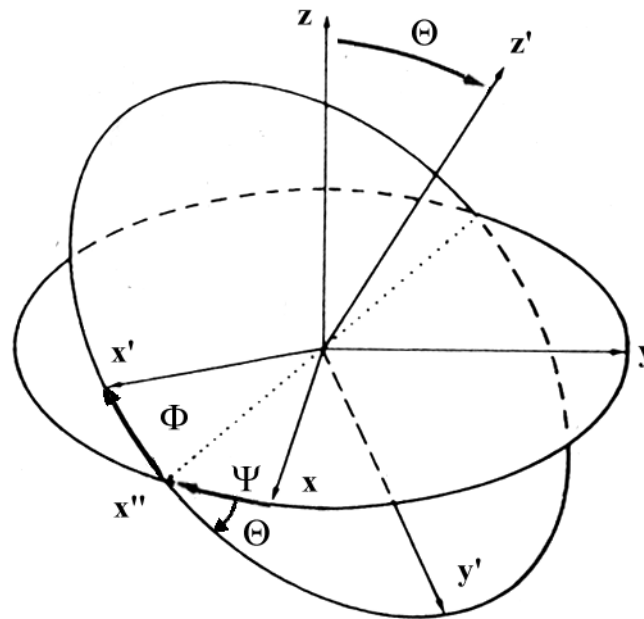


Figure A-3) Graphical definition of the Euler angles (Θ , Φ , and Ψ). The misorientation between two crystals of axes xyz and $x'y'z'$ can be described by a rotation about z , followed by a rotation about x' , and then a rotation of about z' . Figure adapted from Randle[118].

No matter what misorientation description is used, there are a number of crystallographically equivalent rotation matrices \mathbf{M}' , the number of such matrices depending on the symmetry of the crystallographic system. These matrices will result in several equivalent angle/axis combinations.

$$\mathbf{M}' = \mathbf{T}_i \mathbf{M}$$

where \mathbf{T}_i are the symmetry operation matrices and $i=1$ to n ($n=1+n_2+2n_3+3n_4+5n_6$), where n_2 is the number of two fold symmetry axes, n_3 is the number of threefold symmetry axes, etc.

Since $\text{YBa}_2\text{Cu}_3\text{O}_{6+x}$ is approximated as tetragonal ($a \sim b$ and the samples are twinned), there are four two-fold symmetry axes (about $[010]$, $[100]$, $[1\bar{1}0]$, and $[110]$) and one four-fold symmetry axis (about $[001]$), resulting in eight symmetrically equivalent rotation matrices \mathbf{M}' . The individual \mathbf{T}_i rotation matrices are:

$$\begin{bmatrix} 1 & 0 & 0 \\ 0 & 1 & 0 \\ 0 & 0 & 1 \end{bmatrix}, \begin{bmatrix} \bar{1} & 0 & 0 \\ 0 & \bar{1} & 0 \\ 0 & 0 & 1 \end{bmatrix}, \begin{bmatrix} 1 & 0 & 0 \\ 0 & \bar{1} & 0 \\ 0 & 0 & \bar{1} \end{bmatrix}, \begin{bmatrix} \bar{1} & 0 & 0 \\ 0 & 1 & 0 \\ 0 & 0 & \bar{1} \end{bmatrix}, \begin{bmatrix} 0 & \bar{1} & 0 \\ 1 & 0 & 0 \\ 0 & 0 & 1 \end{bmatrix}, \begin{bmatrix} 0 & 1 & 0 \\ \bar{1} & 0 & 0 \\ 0 & 0 & 1 \end{bmatrix}, \begin{bmatrix} 0 & \bar{1} & 0 \\ \bar{1} & 0 & 0 \\ 0 & 0 & \bar{1} \end{bmatrix}, \begin{bmatrix} 0 & 1 & 0 \\ 1 & 0 & 0 \\ 0 & 0 & \bar{1} \end{bmatrix}$$

By convention the angle/axis pair with the smallest angle is sometimes called the disorientation angle and this angle/axis pair is used to describe the bicrystal misorientation.

The Mixed Misorientation Description - Example

Here is an example showing how raw x-ray pole figure data are converted into a axis/angle pair description of the misorientation. The x-ray data for sample MB4C1 was taken as described in **Chapter 3. Figure A-4** shows this data plotted on a stereographic projection with the aid of a Wulff net (**Figure A-5**), a device used in solving stereographic projection problems.[158] The Wulff nets used in my work, with a diameter of 18cm, are accurate to $\sim 1^\circ$.

Pole Figure Data for Sample MB4C.1

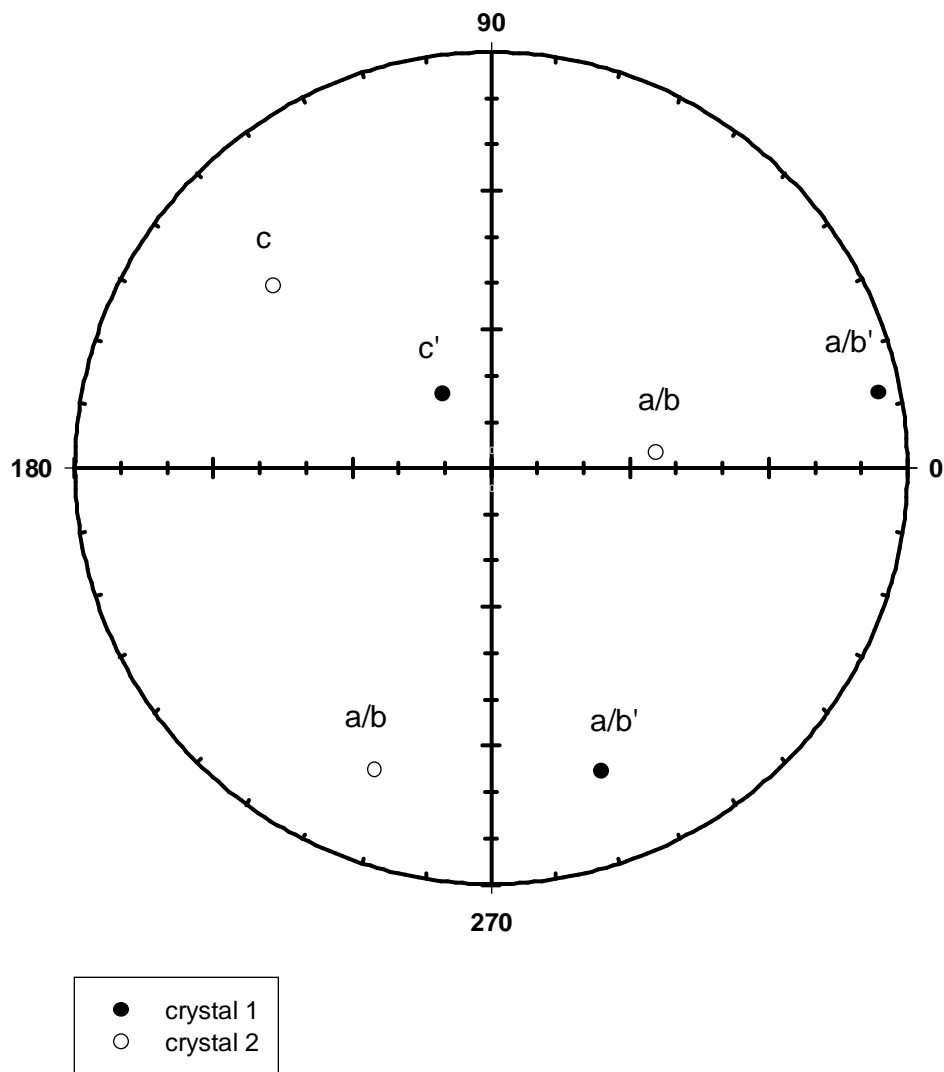


Figure A-4) Pole figure data plotted on a stereographic projection, with each point a centroid of the labeled pole. The orthorhombic structure of YBCO constrains which pole belongs to which crystal.

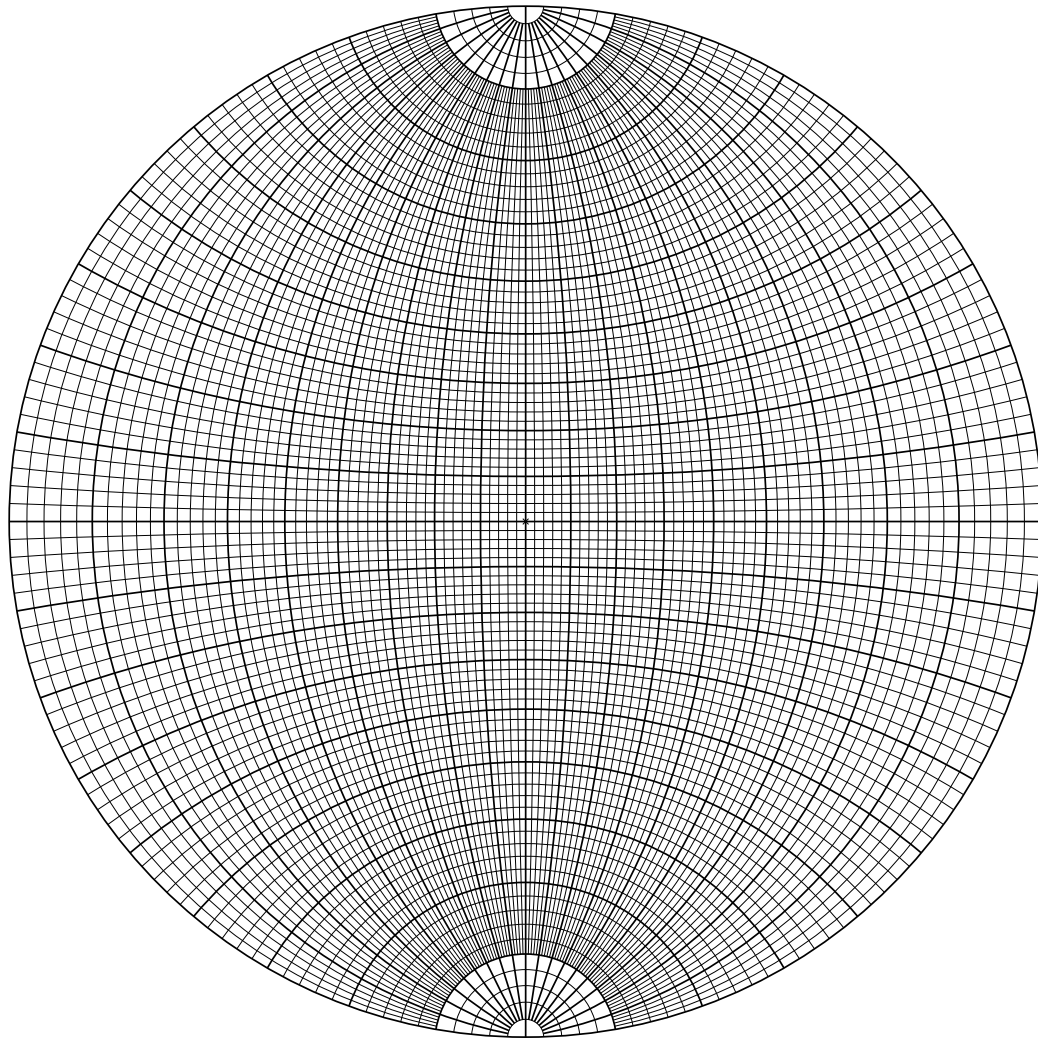


Figure A-5) A Wulff net, used to measure angles from a stereographic projection. The longitudinal lines are known as the “great circles.”

Measurements of each element of the matrix are accomplished by rotating two poles of interest on the stereographic projection so that the two poles are coincident on the same “great circle”, like the c-axis poles for each crystal in **Figure A-6**. The cosine of the angle

between these poles on the same great circle form a matrix element. Finding the angular relationship between all poles allows us to build the misorientation matrix:

$$\mathbf{M} = \begin{bmatrix} \cos 51^\circ & \cos 67^\circ & \cos 47^\circ \\ \cos 128^\circ & \cos 38^\circ & \cos 82^\circ \\ \cos 113^\circ & \cos 124^\circ & \cos 44^\circ \end{bmatrix}$$

$$\cos\theta = (0.6293 + 0.7880 + 0.7193 - 1)/2$$

$$\therefore \theta = 55^\circ$$

$$U:V:W = -0.6984:1.073:-1.0064$$

This UVW ratio would be the ratio of the Miller indices only in the cubic case. In order to get the axis ratio in terms of Miller indices, we need to multiply the U and V values by 3 for YBCO ($c \sim 3a, b$).

$$U:V:W \sim \bar{15}:23:\bar{7} \sim \bar{2}:3:\bar{1}$$

Performing the symmetry operations resulted in a series of matrices that all happened to have a smaller trace than the original matrix, which means the original matrix had the smallest θ . Therefore the disorientation angle/axis pair for the MB4C1 bicrystal is described as $55^\circ[\bar{2} \ 3 \ \bar{1}]$.

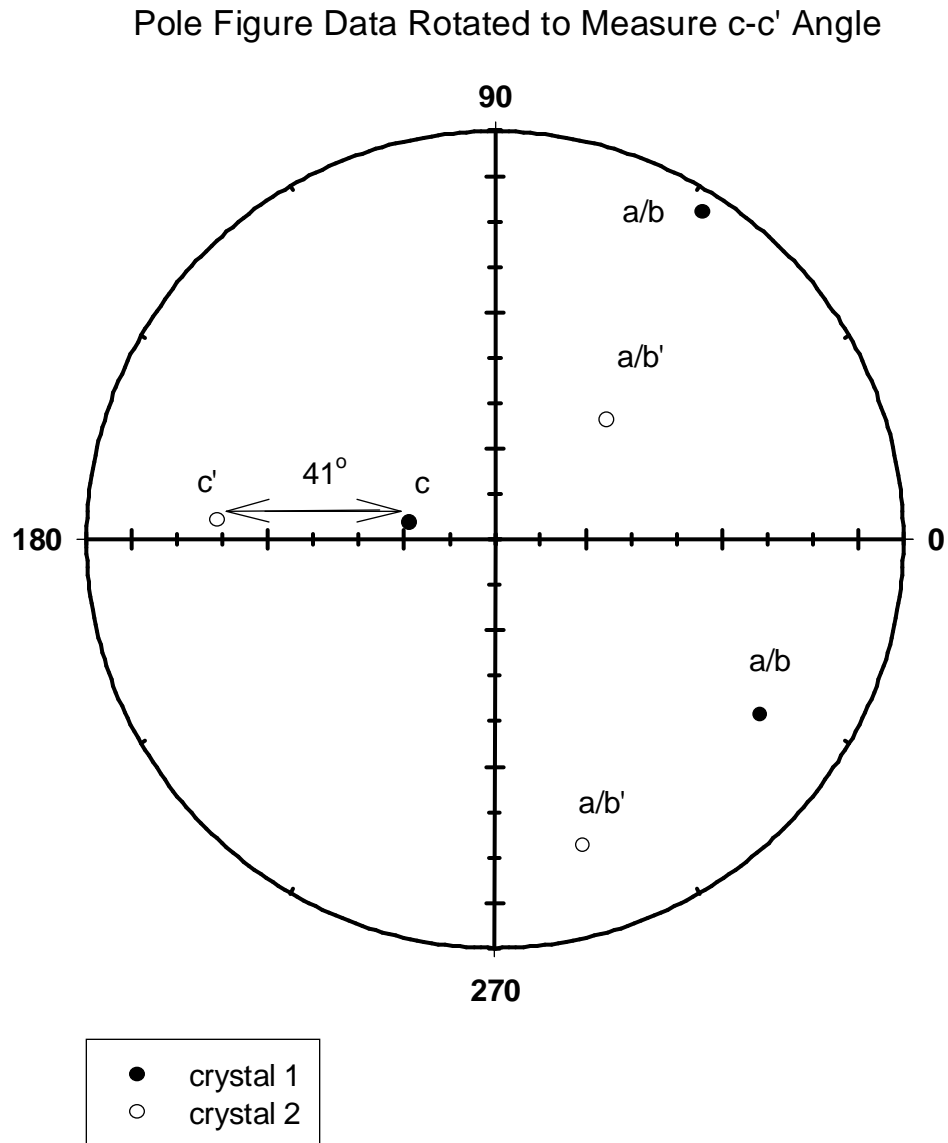


Figure A-6) The poles marked on Figure A-4 are rotated so that the c' and c poles lie on the same great circle. Then the misorientation angle between c and c' can be determined by noting the angular distance on the great circle ($\theta_{cc'}=41^\circ$).

Appendix B: Laser Cutting of $\text{YBa}_2\text{Cu}_3\text{O}_{6+x}$

The fracture technique for bicrystal isolation resulted in only low yields of measurable bicrystals from a given batch of starting material. Many of these were of such small size that it was difficult to perform x-ray pole figures and to apply contacts for electrical experiments. Melt textured samples often have large grains, on the order of millimeter size. If mm-scale bicrystals could be isolated, x-ray pole figure data collection would be greatly simplified, and contacting would be eased to the extent that it would now be practical to apply intragranular as well as intergranular, contacts to the samples. Cutting samples with a finely focused laser beam seemed to be a promising solution; Schindler et al.[36] had showed that individual grain boundaries in sintered Dy-123 could be isolated with the aid of a laser cutter.

Lasers with different wavelengths have different material interactions. Excimer lasers, used in the laser deposition of high T_c films, have a short wavelength and remove material by the process of ablation. Ablation is the name of the process whereby ultraviolet photons break the chemical bonds on the target, decomposing the compound into its constituent molecular components. This procedure results in little heating to the adjoining regions. By contrast, solid-state lasers, like Nd:YAG (Nd^{+3} doped $\text{Y}_3\text{Al}_5\text{O}_{12}$), or frequency doubled or tripled Nd:YAG, have a long wavelength (in the visible or infrared region) and remove material by the process of thermoevaporation. Thermoevaporation involves the local heating of the material through the solid-liquid-gas transitions until the

material is ejected (**Figure B-1**)[159] from the incident beam region. With a thermoevaporative process, it is required that the material have low thermal diffusivity in order to keep the beam energy localized so as to facilitate cutting and to prevent heat damage to the adjoining regions. This is a large part of the reason why infrared lasers are more effective at cutting ceramics than metals. Another is that metals easily reflect the incident laser beam.

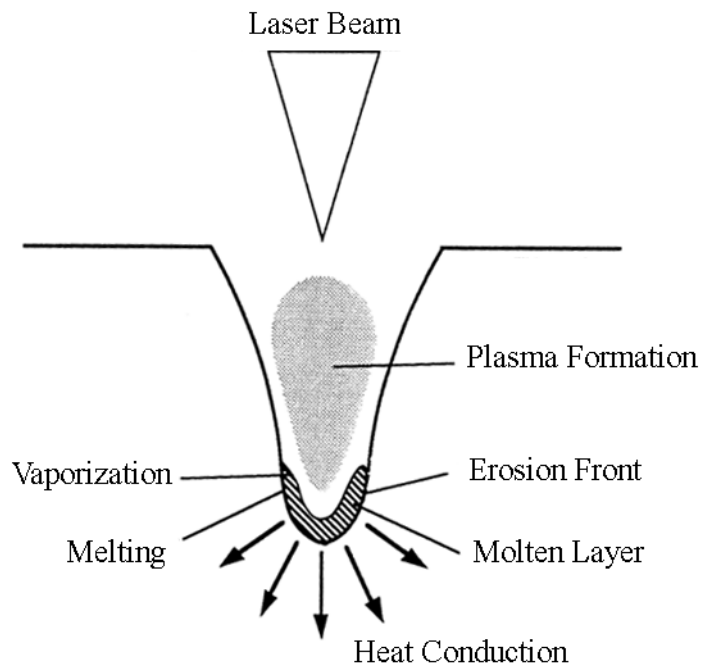


Figure B-1) Schematic drawing of the thermoevaporation process from ref.[159]. Laser beam first melts the material and then heats the liquid until the vapor phase is formed and ejected from the cut.

The amount of laser energy absorbed by YBCO as a function of wavelength has been investigated with respect to Bouguer's Law of absorption (Equation B-1)[160]. The

variable q is the radiation at depth z into the sample, q_0 the initial radiation, R is the reflectivity and α is the absorption coefficient:

Equation B-1

$$q(z) = q_0(1 - R)e^{-\alpha z}$$

Table B-1: Bouguer's constants for different laser wavelengths[160].

Laser	Wavelength(μm)	$\alpha(10^5 \text{ cm}^{-1})$	R
CO ₂	~10	0.5	0.75
Nd:YAG	1.064	1.2	0.18
Nd:YAG(freq. doubled)	0.533	1.5	0.14
Nd:YAG(freq. tripled)	0.355	1.7	0.12
XeCl(excimer)	0.308	1.9	0.12
KrF(excimer)	0.248	2.3	0.13
ArF(excimer)	0.193	2.4	0.15

From **Table B-1** we see that except for the CO₂ laser, the reflectivities (R) are similar, so the absorption coefficient (α) is the key parameter. Clearly, the longer wavelength is better, although the CO₂ wavelength is so large that it is on the same order of magnitude of the dimensions of the desired cut features. Some experimental evidence with respect to YBCO film deposition has quantitatively shown that the infrared wavelength couples better to YBCO than do the shorter wavelengths of excimer lasers (**Figure B-2**)[161], thus allowing for more efficient removal of material.

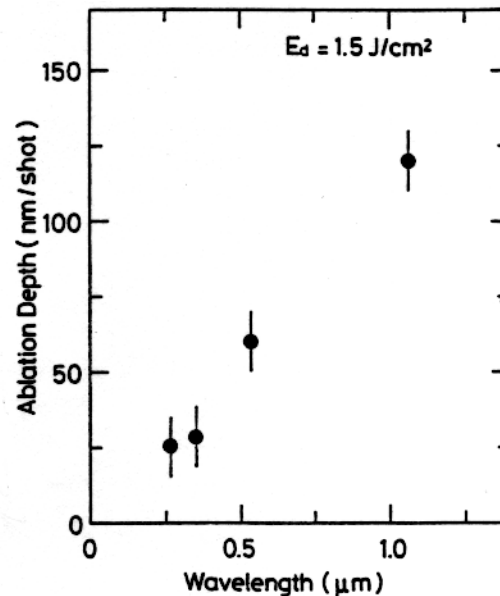


Figure B-2) Plot of ablation depth per laser shot as a function of laser wavelength, from ref.[161].

Our requirements for a laser cutter, the ability to cut ceramic material 50-100 μm thick with a minimal cut width and damage region, but at a reasonable cost, led to a series of lasers made for the semiconductor failure analysis industry. The lasers are mounted on microscopes and are designed to remove passivation layers. Several lasers were tested for their effectiveness in cutting sample YBCO material, including frequency doubled Nd:YAG ($\lambda=532\text{nm}$) green lasers, as well as a Xenon ($\lambda=480\text{-}520\text{nm}$) and an infrared Nd:YAG ($\lambda=1064\text{nm}$). Results varied, with some units cutting narrower, deeper and faster than others. One laser, the infrared Nd:YAG, performed above the rest, as its high shot frequency and infrared wavelength helped it cut faster. The final purchased laser was manufactured by the Florod Co. It consisted of an Amoco solid state Nd:YAG pulsed laser, two mirrors, a telescoping lens and an iris shutter that directed the beam vertically

through the microscope (**Figure B-3**). The laser operated at 1064nm with a pulse width of 15ns. The maximum power is 35mJ (max. energy density $\sim 40\text{J}/\text{cm}^2$) out of the objective with a variable pulse rate of 1 - 15000 Hz and a spot size of 2-20mm. This spot size was adjustable by changing the telescoping ratio and by varying the shutter diameter. The laser was fired through a long working distance Mitutoyo microscope which was mounted on a Micromanipulator probe station. The X-Y stage of the probe station can be moved with micron scale precision. The laser was selected for its ability to cut deep but narrow lines in YBCO (it can achieve a steep-sided cut $80\mu\text{m}$ deep and $30\mu\text{m}$ wide).

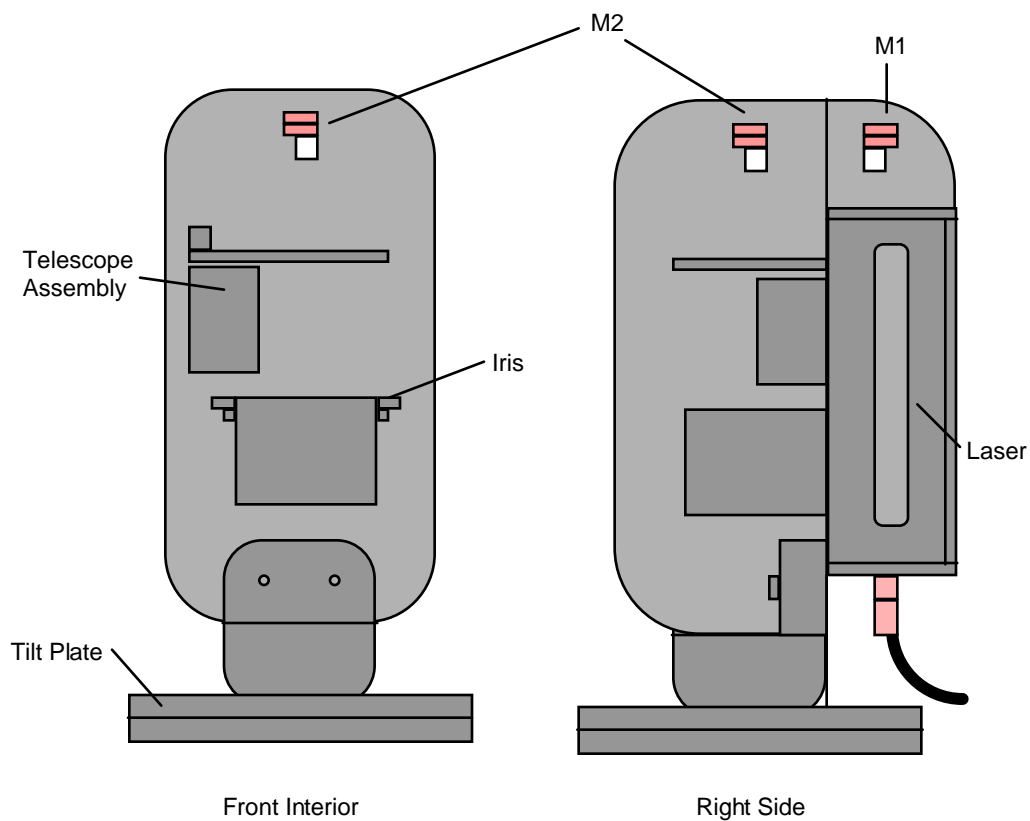


Figure B-3) Drawing of the Florod Nd:YAG laser, from the Florod LMS Manual[162]. This assembly is mounted with the tilt plate attached to the top part of a long working distance Mitutoyo microscope.

The possibility of laser damage to the bulk of the cut material was investigated. The appearance of the material directly after cutting was discolored, (**Figure B-4a**). This discoloration was not damage however. It was material ejected from the cut that had settled on the surface. It could be removed by washing with methanol, which left behind an extremely clean cut (**Figure B-4b**). Twins, which are very sensitive to local oxygen concentration, could be seen in laser-cut samples right up to the cut edge. Thus the damaged region may be estimated as no wider than the resolution of the microscope ($\sim 1\mu\text{m}$). Recent results in YBCO thick films cut with a Nd:YAG laser with two orders of magnitude higher energy density had cut walls with a heat affected zone of $3\mu\text{m}$ [163]. Since the dimensions of our bulk samples are orders of magnitude larger than the largest estimated size of the damage zone, we believe laser cutting to be an extraction technique that does not effect the properties of our material.

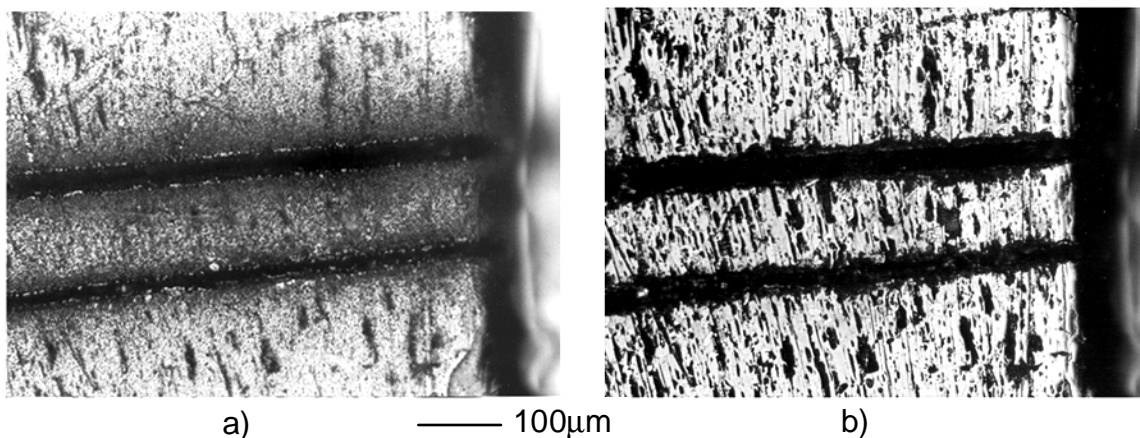


Figure B-4) An unpolarized light micrograph of a melt texture sample cut with a Nd-YAG laser a) before and b) after cleaning with methanol. The discoloration surround the cut in the first image is due to re-deposit material from the cut, and is not sample damage.

As well as cutting melt-textured YBCO, the laser has proven effective in slicing unsheathed BSCCO tape [164], as well as trimming flux-grown YBCO[147] and BSCCO bicrystals.[154] Other groups outside the UW are currently using lasers to assist in the electromagnetic investigation of bulk ceramic superconductors[38,165].

References

- [1] M. K. Wu, J. R. Ashburn, C. J. Torng, P. H. Hor, R. L. Meng, L. Gao, Z. J. Huang, Q. Wang, and C. W. Chu, *Phys. Rev. Lett.* **58**, 908 (1987).
- [2] M. Suenaga, D.O. Welch, and R. Budhani, *Supercond. Sci. Technol.* **5**, S1 (1992).
- [3] M. Okada, A. Okayama, T. Morimoto, T. Matsumoto, R. Aihara, and S. Matsuda, *Jpn. J. Appl. Phys.* **27**, 185-187 (1988).
- [4] S. E. Babcock, X. Y. Cai, D. L. Kaiser and D. C. Larbalestier, *Nature* **347**, 167 (1990).
- [5] K. Salama, V. Selvamanickam, L. Gao, and K. Sun, *Appl. Phys. Lett.* **54(23)**, 2352 (1989).
- [6] D. Shi, H. Krishnan, J.M. Hong, D. Miller, P.J. McGinn, W.H. Chen, M. Xu, J.G. Chen, M.M. Fang, U. Welp, M.T. Lanagan, K.C. Goretta, J.T. Duser, J.J. Picciolo, and U. Balachandran, *J. Appl. Phys.* **68(1)**, 228 (1990).
- [7] T. Venkatesan, X.D. Wu, B. Dutta, A. Inam, M.S. Hedge, D.M. Hwang, D.M. Chang, L. Nazar, and B. Wilkens, *Appl. Phys. Lett.* **54**, 581 (1989).
- [8] G. Deutscher and K. A. Müller, *Phys. Rev. Lett.* **59**, 1745 (1987).
- [9] B. Oh, K. Char, A. P. Kent, M. Naito, M. R. Beasley, T. H. Geballe, R. H. Hammond, A. Kapitulnik, and J. M. Graybeal, *Phys. Rev.* **B 37**, 7861 (1988).
- [10] A.K. Ghosh, M. Suenaga, T. Asano, A. R. Moodenbaugh, R. L. Sabatini, *Adv. Cryogenic Mater.* **34**, 607 (1987).
- [11] “Concise Encyclopedia of Magnetic and Superconducting Materials” ed. J. Evetts, Pergamon Press, 415 (1992).
- [12] T. Hikata et al., *Jap J. Appl. Phys* **28**, L82 (1989).
- [13] D. Dimos, J. Mannhart, P. Chaudhari, and F. K. LeGoues, *Phys. Rev. Lett.* **61**, 219 (1988).
- [14] D. Dimos, J. Mannhart and P. Chaudhari, *Phys. Rev.* **B 41**, 4038 (1990).
- [15] M.F. Chisholm, and S.J. Pennycook, *Nature* **351**, 47 (1991).

-
- [16] A.H. Cardona, H.Suzuki, T. Yamashita, K.H. Young, L.C. Bourne, Appl. Phys. Lett. **62(4)**, 411 (1993).
- [17] M. Kawasaki, E. Sarnelli, P. Chaudhari, A. Gupta, A. Kussmaul, J. Lacey, and W. Lee, Appl. Phys. Lett. **62(4)**, 417 (1993).
- [18] C. B. Eom, A. F. Marshall, Y. Suzuki, B. Boyer, R. F. W. Pease, and T. H. Geballe, Nature **353**, 544 (1991).
- [19] D.J. Lew, Y. Suzuki, A.F. Marshall, T.H. Geballe, and M.R. Beasley, Appl. Phys. Lett. **65(12)**, 1584 (1994).
- [20] D. C. Larbalestier, S. E. Babcock, X. Y. Cai, M. B. Field, Y. Gao, N. F. Heinig, D. L. Kaiser, K. Merkle, L. K. Williams, N. Zhang, Physica C **185-189**, 315 (1991).
- [21] N Heinig, unpublished.
- [22] M.B. Field, X.Y. Cai, S.E. Babcock, and D.C. Larbalestier, IEEE Trans. on Superconductivity, Vol.**3(1)**,1479, (1993).
- [23] I.K. Yanson, Soviet Physics JETP **31(5)**, 800 (1970).
- [24] L.N. Bulaevskii, J.R. Clem, L.I. Glazman, and A.P. Malozemoff, Phys. Rev. B **45**, 2545 (1992); L.N. Bulaevskii, L.L. Daemen, M.P. Maley, and J.Y. Coulter, Phys. Rev. B **48**, 13798 (1993).
- [25] S. E. Babcock, X. Y. Cai, D. C. Larbalestier, D.H. Shin, N. Zhang, et al., Physica C **227**, 183 (1994).
- [26] Y. Iijima, N. Tanabe, O. Kohno, and Y. Ikeno, Appl. Phys. Lett **74**, 1905 (1993).
- [27] X.D. Wu, S.R. Foltyn, P. Arendt, J. Townsend, C. Adams, I.H. Campbell, P. Tiwari, Y. Coulter, and D.E. Peterson, Appl. Phys. Lett. **65(15)**, 1961 (1994).
- [28] A. Goyal, D.P. Norton, J.D. Budai, M. Paranthaman, E.D. Specht, D.M. Kroeger, D.K. Christen, Q. He, B. Saffian, F.A. List, D.F. Lee, P.M. Martin, C.E. Klabunde, E. Hatfield, and V.K. Sikka, preprint, (1996).
- [29] J.A. Lewis, and M. Wegmann, Appl. Phys. Lett. **67(20)**, 3028 (1995).
- [30] S.R. Foltyn, P. Arendt, X.D. Wu, W.R. Blumenthal, J.D. Cotton, J.Y. Coulter, W.L. Hutts, H.F. Safar, J.L. Smith, and D.E. Peterson, Extended Abstracts, MRS/ISTEC International Workshop on Superconductivity, Maui, HI, 1995.

-
- [31] J.A. Lewis, ASC 96 Pittsburgh Poster Presentation (1996).
- [32] A. Parikh, B. Meyer, and K. Salama, *Supercond. Sci. Technol.* **7**, 455 (1994).
- [33] M.B. Field, D.C. Larbalestier, A.S. Parikh, and K. Salama, Submitted to *Physica C*, (1996).
- [34] Z. Yi, S. Ashworth, C. Beduz, and R.G. Scurlock, *IEEE Trans. on Magnetics* **27**, 1506 (1991).
- [35] G. Schindler, B. Seebacher, and K. Andres, *Journal of Less-Common Metals*, **164&165**, 1346 (1990).
- [36] G. Schindler, B. Seebacher, R. Kleiner, P. Müller and K. Andres, *Physica C* **196**, 1 (1992).
- [37] C. Sarma, G. Schindler, D.G. Haase, C.C. Koch, A.M. Saleh, and A.I. Kingon, *Appl. Phys. Lett.* **64(1)**, 109 (1994).
- [38] G. Schindler, C. Sarma, D.G. Haase, C.C. Koch, and A.I. Kingon, *Cryogenics* **34(4)**, 287 (1994).
- [39] C. Sarma, G. Schindler, D.G. Haase, C.C. Koch, A.I. Kingon and A. Goyal, *Physica C* **244**, 287 (1995).
- [40] D.W.A. Willén and K. Salama, *Physica C* **201**, 311 (1992).
- [41] M. Nilsson-Mellbin, A. Parikh, K. Salama, *Physica C* **223**, 19 (1994).
- [42] M.B. Field, A. Pashitski, A. Polyanskii, and D.C. Larbalestier, A.S. Parikh, and K. Salama, *IEEE Trans. of Applied Superconductivity*, Vol. **3(2)**, 1631, (1995)
- [43] M.B. Field, A. Pashitski, A. Polyanskii, and D.C. Larbalestier, A.S. Parikh, and K. Salama, to appear in the Proceedings to the 10th Anniversary High Temperature Superconductor Workshop, (1996).
- [44] S. Jin, T.H. Tiefel, R.C. Sherwood, M.E. Davis, R.B. van Dover, G.W. Kammlott, R.A. Fastnacht, and H.D. Keith, *Appl. Phys. Lett.*, **52(24)**, 2074 (1988).
- [45] J.D. Verhoeven, *Metallography* **22**, 245 (1989).
- [46] M.K. Wu, J.R. Ashburn, C.J. Torng, P.H. Hor, R.L. Meng, L. Gao, Z.J. Huang, Y.Q. Wang, and C.W. Chu, *Phys. Rev. Lett.* **58(9)**, 908 (1987).

-
- [47] J.G. Bednorz and K.A. Müller, *Z. Phys. B-Condensed Matter* **64**, 189 (1986).
- [48] J.D. Doss “Engineer’s Guide to High-Temperature Superconductivity”, J. Wiley & Sons, pp. 105, 381 (1989).
- [49] R.Cava, *Phys. Rev. Lett.* (1987).
- [50] A. Santoro, S. Miraglia, F. Beech, S.A. Sunshine, and D.W. Murphy, *Mat. Res. Bull.*, **22**, 1007 (1987).
- [51] J.D. Verhoeven and E.D. Gibson, *Appl. Phys. Lett.* **52**(14), 1190 (1988).
- [52] L. Forro, C. Ayache, J.Y. Henry and J. Rossat-Mignod, *Physica Scripta* **41**, 365 (1990).
- [53] T.R. Dinger, T.K. Worthington, W.J. Gallagher, and R.L. Sandstrom, *Phys. Rev. Lett.* **58**, 2687 (1987).
- [54] H.F. Poulsen, N.H. Andersen, J.V. Andersen, H. Bohr, and O.G. Mouritsen, *Nature* **349**, 594 (1991).
- [55] R. Hauff, V. Breit, H. Claus, D. Herrmann, A. Knierim, P. Schweiss, H. Wühl, A. Erb, and G. Müller-Vogt, Submitted to Proceedings of M²S-HTSC IV, Grenoble, (1994).
- [56] J-L. Wang, Univ. of Wisconsin Ph.D. Thesis, (1996).
- [57] S.J. Rothman, J.L. Routbort, U. Welp, and J.E. Baker, *Phys. Rev. B* **44**(5), 2326 (1991).
- [58] R.J. Cava et al. *Physica C* **156**, 523 (1988).
- [59] R.J. Cava et al. *Physica C* **165**, 419 (1990).
- [60] Z. Fisk, J.D. Thompson, E. Zirngiebl, J.L. Smith, and S-W Cheong, *Solid State Commun.*, **62**(11), 743 (1987).
- [61] M. Murakami, S-I. Yoo, T. Higuchi, N. Sakai, J. Weltz, N. Koshizuka, and S. Tanaka, *Jpn. J. Appl. Phys.* Vol. **33**, L714 (1994).
- [62] R.Beyers and B.T. Ahn, *Annual Rev. of Mat. Sci.* Vol **21**, (1991).
- [63] I-K. Jeong, D-Y. Kim, Z.G. Khim, and S.J. Kwon, *Mater. Lett.* **8**(3,4), 91 (1989).

-
- [64] R.W. McCallum, J.D. Verhoven, M.A. Noack, E.D. Gibson, F.C. Laabs, and D.K. Finnemore, *Advan. Ceram. Mater.* **2**(3B), 388 (1987).
- [65] M. Maeda, M. Kadoi, and T. Ikeda, *Jap. Journ. Of App. Physics* **28**(8), 1417 (1989).
- [66] D.L. Kaiser, F. Holtzberg, B.A. Scott, and T.R. McGuire, *Appl. Phys. Lett.* **51**(13), 1040 (1987).
- [67] M. Murakami, *Supercond. Sci. Technol.* **5**, 185 (1992).
- [68] J. Mannhart and C.C. Tsuei, *Z. Phys. B* **77**, 53 (1989).
- [69] K.B. Alexander, A. Goyal, D.M. Kroeger, V. Selvamanickam, and K. Salama, *Phys. Rev. B*, **45**(10), 5622 (1992).
- [70] M. Daümeling, private communication (1994).
- [71] G-W. Hong, K-B. Kim, I-H. Kuk, C-J. Kim, Y-S. Lee and H-S. Park, Submitted to *IEEE Trans. on Appl. Super.*, Pittsburgh (1996).
- [72] M. Murakami, S. Gotoh, H. Fujimoto, K. Yamaguchi, N. Koshizuka, and S. Tanaka, *Supercond. Sci. Technol.* **4**, S43 (1991).
- [73] K. Yamaguchi, M. Murakami, H. Fujimoto, S. Gotoh, T. Oyama, Y. Shiohara, N. Koshizuka, and S. Tanaka, *J Mater. Res.*, **6**(7), 1404 (1991).
- [74] P. McGinn, N. Zhu, W. Chen, S. Sengupta, and T Li, *Physica C* **176**, 203 (1991).
- [75] S. Jin, G. W. Kammlott, T. H. Tiefel, T. T. Kostas, T. L. Ward and D. M. Kroeger, *Physica C* **181**, 57 (1991).
- [76] S. Jin, T. H. Tiefel, and G. W. Kammlott, *Appl. Phys. Lett.*, **59**(5), 540 (1991).
- [77] M. Murakami, K. Yamaguchi, H. Fujimoto, N. Nakamura, T. Tagauchi, N. Koshizuka, and S. Tanaka, *Cryogenics* **32**(11), 930 (1992).
- [78] M. Chopra, Private Comm. (1996).
- [79] W.K. Kwok, U. Welp, G.W. Crabtree, K.G. Vandervoort, R. Hulscher, and J.Z. Liu, *Phys. Rev. Lett.* **64**, 966 (1990).
- [80] D. Shi, S. Sengupta, J.S. Luo, C. Varanasi, and P.J. McGinn, *Physica C* **213**, 179 (1993).

-
- [81] M. Ullrich, D. Miller, K. Heinemann, L. Neil and H.C. Freyhardt, *Physica C* **198**, 181 (1992).
- [82] R.L. Meng, C. Kinalidis, Y.Y. Sun, L.Gao, Y.K. Tao, P.H. Hor and C.W. Chu, *Nature* Vol. **345**, 326 (1990).
- [83] R. Weinstein, J. Liu, Y. Ren, R.-P. Sawh, D. Parks, C. Foster, and V. Obot, Submitted to the Proceedings for the 10th Anniv. HTS Workshop, Houston (1996).
- [84] M. Murakami, M. Morita, K. Doi, and K. Miyamoto, *Jpn. J. Appl. Phys.* Vol. **28**(7), 1189 (1989).
- [85] M. Morita, M. Tanaka, S. Takebayashi, K. Kimura, K. Miyamoto and K. Sawano, *Jpn. J. of Appl. Phys.* Vol. **30**(5A), L813 (1991).
- [86] N. Ogawa, I. Hirabayashi, and S. Tanaka, *Physica C* **177**, 101 (1991).
- [87] J-I. Shimoyama, J-I. Kase, S. Kondoh, E. Yanagisawa, T. Matsubara, M. Suzuki, and T. Morimoto, *Jpn. J. of Appl. Phys.* **29**(11), L1999 (1990).
- [88] V. Chakrapani, D. Balkin, and P. McGinn, *Appl. Supercond.* Vol. 1 No. 1/2, 71 (1993).
- [89] C.J. Kim, K.B. Kim, K.W. Lee, C.T. Lee, G.W. Hong, I.S. Chang and D.Y. Won, *Materials Letters* Vol. **11**, No. 8/9, 241 (1991).
- [90] M. Murakami, S-I. Yoo, T. Higuchi, N. Sakai, M. Watabiki, N. Koshizuka, and S. Tanaka, *Physica C* **235-240**, 2781 (1994).
- [91] M. Morita, S. Takebayashi, M. Tanaka, K. Kimura, K. Miyamoto, and K. Sawano, *Proceedings of ISS'90*.
- [92] R.L. Meng, L. Gao, P. Gautier-Picard, D. Ramirez, Y.Y. Sun, C.W. Chu, *Physica C* **232**, 337 (1994).
- [93] V.R. Todt, X.F. Zhang, and D.J. Miller, Fall MRS Poster Presentation (1995).
- [94] M.B. Field, unpublished.
- [95] D.W.A. Willen and K. Salama, *Physica C* **201**, 311 (1992).
- [96] Y. Masuda, R. Ogawa, and Y. Kawate, *J. Mater. Res.* **8**, 693 (1993).

-
- [97] J. Wang, I. Monot, M. Hervieu, J. Provost and G. Desgardin, *Supercond. Sci. Technol.* **9**, 69 (1996).
- [98] L.T. Romano, P.R. Wilshaw, N.J. Long, and C.R.M. Grovenor, *Supercond. Sci. Technol.* **1**, 285 (1989).
- [99] T.Y. Hsiang and D.K. Finnemore, *Phys. Rev. B* **22**, 154 (1980).
- [100] D.P. Hampshire and S-W. Chan, *J. Appl. Phys.* **72**(9), 4220 (1992).
- [101] S.E. Russek, D.K. Lathrop, B.H. Moeckly, R.A. Buhrman, D.H. Shin, and J. Silcox, *Appl. Phys. Lett.* **57**(11), 1155 (1990).
- [102] C.S. Owen and D.J. Scalapino, *Phys. Rev. Vol.* **164**, No. 2, 538 (1967).
- [103] K. Schwidtal, *Phys. Rev. B* **2**(7), 2526 (1970)
- [104] I-F Tsu, S.E. Babcock, D.L. Kaiser, *J. Mater. Res.* **11**(6), 1383 (1996).
- [105] W.T. Read, Jr., "Dislocations in Crystals", McGraw-Hill Book Co., Inc, 157 (1953).
- [106] M.L. Kronberg and F.H. Wilson, *Trans. Am. Inst. Miner. Engr.* **215**, 820 (1959).
- [107] D.A. Smith, M.F. Chisolm, and J. Clabes, *Appl. Phys. Lett.* **53**(23), 2334 (1988).
- [108] R. Bonnet, E. Cousineau and D.H. Warrington, *Acta Cryst.* **A37**, 184 (1981).
- [109] S.E. Babcock and D.C. Larbalestier, *J. Mater. Res.* **5**, 919 (1990).
- [110] A. Singh, N. Chandrasekhar, and A.H. King, *Acta Cryst. B* **46**, 117 (1990).
- [111] Y. Zhu, H. Zhang, H. Wang, and M. Suenaga, *J. Mater. Res.* **6**(12), 2507 (1991).
- [112] K.L. Merkle, *J. Phys. Chem. Solids*, **55**(10), 991 (1994).
- [113] S-W. Chan, *J. Phys. Chem. Solids* **55**(12), 1415 (1994).
- [114] J. Orehotsky, H. Wiesmann, A. R. Moodenbaugh, M. Suenaga, H. G. Wang, and H. Herman, *IEEE Trans. on Magnetics*, vol. **27**, 914 (1991).
- [115] J. Wang, I. Monot, M. Hervieu, J. Provost, and G. Desgardin, *Supercond. Sci. Technol.* **9**, 69 (1996).

-
- [116] C-J. Kim, K-B. Kim, and G-W. Hong, *Supercond. Sci. Technol.* **7**, 812 (1994).
- [117] T. Wolf, W. Goldacker, B. Obst, G. Roth, R. Flukiger, *Journal of Crystal Growth* **96**, 1010 (1989).
- [118] V. Randle, "The Measurement of Grain Boundary Geometry," Institute of Physics Publishing, Bristol UK, (1993).
- [119] Beraha, E. and Shpigler, B., "Color Metallography", American Society for Metals, (1977).
- [120] P. Diko, N. Pelerin, and P. Odier, *Physica C* **247**, 169 (1995).
- [121] Cullity, B. D., "Elements of X-Ray Diffraction", Addison-Wesely Publishing Co. Inc., (1978).
- [122] D. Chateigner, P. Germi, M. Ingold, M. Pernet, *Physica C* **185-189**, 2411 (1991).
- [123] M. Kimura, M. Tanaka, H. Horiuchi, M. Morita, M. Tanaka, M. Matsuo, H. Morikawa, and K. Sawano, *Physica C* **174**, 263 (1991).
- [124] D.J. Dingley and K. Baba-Kishi, *Scanning Electron Microscopy*, vol ii, 383 (1986).
- [125] Y. Matsumoto, T. Degener, and C. Heiden, *Jap. J. of App. Phys.*, **27**(11), 2065 (1988).
- [126] D.P. Hampshire, X. Cai, J. Seuntjens, and D.C. Larbalestier, *Supercond. Sci. Technol.*, Vol. **1**, 12 (1988).
- [127] J.W. Ekin, H.R. Hart, Jr., and A.R. Gaddipati, *J. Appl. Phys.*, **68**(5), 2285 (1990).
- [128] D. Shi, *J of Electronic Materials*, vol. **22**(10), 1211 (1993)
- [129] M. Daümling, E. Sarnelli, P. Chaudhari, A. Gupta and J. Lacey, *Appl. Phys. Lett.* **61**, 1355 (1992).
- [130] P. Morgan, Rockwell, Private Comm.
- [131] F.F. Lange, *Acta Metallurgica* **15**, 311 (1967).

-
- [132] R.H. Koch, V. Foglietti, W.J. Gallagher, G. Koren, A. Gupta, and M.P.A. Fisher, *Phys. Rev. Lett.*, **63**(14), 1511 (1989).
- [133] K.Y. Blohowiak, D.F. Garrigus, T.S. Luhman, K.E. McCrary, M. Strasik, I.A. Aksay, F. Dogan, W.B. Hicks, J. Liu, and M. Sarikaya, *IEEE Trans. on Appl. Supercond.*, **3**(1), 1049, (1993).
- [134] M. Murakami, T. Oyama, H. Fujimoto, T. Taguchi, S. Gotoh, Y. Shiohara, N. Koshizuka, and S. Tanaka, *Jap. J. Appl. Phys.*, **29**, L1991 (1994).
- [135] M. Morita, S. Takebayashi, M. Tanaka, K. Kimura, K. Miyamoto, and K. Sawano, *Proceedings of ISS'90*, 733 (1990).
- [136] H. Edelman, U. of Wisconsin-Madison PhD. Thesis in Physics (1995).
- [137] M.R. Koblischka and R.J. Wijngaarden, *Supercond. Sci. Technol.* **8**, 199 (1995).
- [138] R. Hedderich, T. Schuster, H. Kuhn, J. Geerk, G. Linker, and M. Murakami, *Appl. Phys. Lett.* **66**(23), 3215 (1995).
- [139] R. Gross and B. Mayer, *Physica C* **180**, 235 (1991).
- [140] Z.G. Ivanov, P. Å Nilsson, D. Winkler, J.A. Alarco, T. Claeson, E.A. Stepantsov and A. Ya. Tzalenchuk, *Appl. Phys. Lett.* **59**(23), 3030 (1991).
- [141] E. Sarnelli, P. Chaudhari and J. Lacy, *Appl. Phys. Lett.*, vol 62(7), (1993) 777.
- [142] J.W. Ekin, H.R. Hart, Jr. and A.R. Gaddipati, *J. Appl. Phys.*, Vol **68**(5), 2285 (1990).
- [143] M.B. Field, University of Wisconsin-Madison Preliminary Examination, (1994).
- [144] B.H. Moeckly, D.K. Lathrop, and R. A. Buhrman, *Phys. Rev B*, **47**(1) 400 (1993).
- [145] N. Browning, M.F. Chisholm, S.J. Pennycook, D.P. Norton and D.H. Lowndes, *Physica C* **212**, 185 (1993).
- [146] N.F. Heinig, R.D. Redwing, I-F. Tsu, A. Gurevich, J.E. Nordman, S.E. Babcock, and D.C. Larbalestier, *Appl. Phys. Lett.* **69**(4), 577 (1996).
- [147] X.Y. Cai, I-F. Tsu, A. Gurevich, S.E. Babcock, and D.C. Larbestier, in preparation.

-
- [148] H. Suhara, T. Nabatame, O.-B. Hyun, S. Koike, and I. Hirabayashi, *Supercond. Sci. Technol.* **8**, 443 (1995).
- [149] I-F. Tsu, S.E. Babcock and D.L. Kaiser, *J. Mater Res.*, **11**(6), 1383 (1996).
- [150] M.K. Mironova, G. Du, I.A. Rusakova, and K. Salama, Submitted to *Physica C*, (1996).
- [151] M.B. Field, unpublished.
- [152] N.F. Heinig, Univ of Wisconsin-Madison Ph.D. Thesis, (1996).
- [153] Z.G. Ivanov, P.Å. Nilsson, D. Winkler, J.A. Alarco, T. Claeson, E.A. Stepanotsov and A.Y. Tzalenchuk, *Appl. Phys. Lett.* **59**(23), 3030 (1991).
- [154] J-L. Wang, I-F. Tsu, X.Y. Cai, R.J. Kelly, M.D. Vaudin, S.E. Babcock, D.C. Larbalestier, *J of Mat. Res.* **11**(4), 868 (1996).
- [155] H.C. Freyhardt, J. Hoffmann, J. Wiesmann, J. Dzick, K. Heinemann, A. Isaev, F. Garcia-Moreno, S. Sievers, A. Usoskin, Submitted to the Proceedings of 1996 ASC, Pittsburgh (1996).
- [156] A. Pashitski and A. Polyanskii, unpublished.
- [157] H. Goldstein, "Classical Mechanics" Second Edition, Addison-Wesley Publishing Co., 1980, Reading, Mass.
- [158] B.D. Cullity, "Elements of X-Ray Diffraction" Second Edition, Addison-Wesley Publishing Co., 1978, Reading, Mass.
- [159] G. Chryssolouris, "Laser Machining, Theory and Practice", Springer-Verlag New York Inc., 1991.
- [160] Reference lost.
- [161] O. Eryu, K. Murakami, K. Masuda, K. Shihoyama, and T. Mochizuki, *Jpn. J. Appl. Phy.*, **31**, L86 (1992).
- [162] Florod LMS User Guide, 3 (1992).
- [163] U. Varshney, B.D. Eichelberger III, J.M. Glass, R.J. Churchill and A.I. Kingon, *J. Mater. Res.*, **8**(10), 2429 (1993).

[164] D.C. Larbalestier, X.Y. Cai, Y. Feng, H. Edelman, A. Umezawa, G.N. Riley Jr., and W.C. Carter, *Physica C* **221**, 299 (1994).

[165] Th. Schuster, H. Kuhn, A. Raiber, T. Abeln, F. Dausinger, H. Hügel, M. Kläser, and G. Müller-Vogt, *Appl. Phys. Lett.* **68**(18), 2568 (1996).